Tréhu, A.M., Bohrmann, G., Rack, F.R., Torres, M.E., et al., 2003
Proceedings of the Ocean Drilling Program, Initial Reports Volume 204

6. Site 1247[1]

Shipboard Scientific Party[2]

INTRODUCTION

Site 1247 (proposed Site HR4c) is located in ~835 m of water on the western flank of Hydrate Ridge ~800 m northwest of the southern summit (see Fig. **F1C,** p. 51, in the "Leg 204 Summary" chapter). The three-dimensional (3-D) seismic data indicate that the seismic stratigraphic setting is similar to that of Site 1245 (see Fig. **F5,** p. 55, in the "Leg 204 Summary" chapter). The bottom-simulating reflector (BSR) is at a depth of ~121–124 meters below seafloor (mbsf) at this site. Horizon A is brighter and shallower (~160 mbsf) at Site 1247 than at Site 1245; Horizon Y is also shallower (~60 mbsf) at this site.

The primary objective at Site 1247 was to sample sediments and fluids from Horizon A, which lies at a location approximately halfway between Site 1245 and the summit (Site 1249), in order to determine updip variations in the physical and chemical characteristics of this horizon and, thus, understand the role it plays in fluid migration and formation of hydrate on the seafloor at the summit. A second objective was to sample Horizon A where the amplitude of this reflector changes dramatically over a short distance.

Two holes were drilled at Site 1247 (Fig. **F1**). Although they are only 87 m apart, the two holes sample parts of Horizon A with distinctly different seismic characteristics (Fig. **F2**). Hole 1247A was drilled without coring to a depth of 270 mbsf to obtain logging-while-drilling (LWD) data for this site. We returned to core Hole 1247B, which was offset from Hole 1247A by ~87 m to the west. Hole 1247B was cored to 220 mbsf using the advanced piston corer (APC) and extended core barrel (XCB).

Samples suspected of containing hydrate, based on infrared (IR) temperature anomalies, were recovered from 93 and 113 mbsf and stored temporarily in liquid nitrogen. However, on later inspection, it was dis-

F1. Bathymetric map, p. 27.

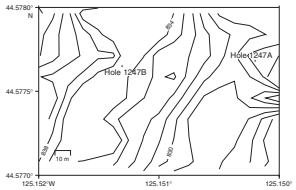

F2. Seismic characteristics of Horizon A, p. 28.

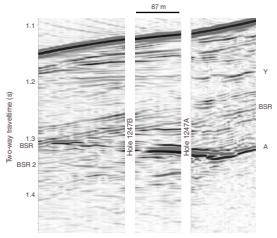

[1]Examples of how to reference the whole or part of this volume.
[2]Shipboard Scientific Party addresses.

Ms 204IR-106

covered that, although the samples showed textures indicative of hydrate dissociation, no hydrate was actually preserved.

OPERATIONS

Two holes were drilled at this site (Table T1) under good weather conditions. Wind speed was 4–19 kt, gusting to 23 kt; seas were 4–7 ft; swell was 6–7 ft; and the prevailing sea-surface current was from the north at ~0.5 kt.

T1. Coring summary, p. 70.

Hole 1247A was drilled without coring to obtain the initial LWD data for this site. We initiated continuous LWD/measurement-while-drilling (MWD) drilling and advanced at a rate of penetration (ROP) of 25–30 m/hr, to a total depth (TD) of 270.0 mbsf. LWD operations began at 2030 on 20 August, with tool initialization at the rig floor. LWD tools included the Resistivity at the Bit (RAB)-6 tool, with $9^1/_8$-in button sleeve, MWD, the Nuclear Magnetic Resonance (NMR-MRP) tool, and Vision Neutron Density (VND) tool. Heave conditions increased, and the real-time data record was changed to increase the time resolution of weight-on-bit and torque measurements for heave analysis (see "Downhole Logging," p. 19). LWD tools were pulled to ~60 m above the seafloor for the dynamic positioning move to Site 1248. Total bit run was ~21 hr.

We returned to this site on 22–24 August to core Hole 1247B. Hole 1247B was offset from Hole 1247A by ~87 m to the west. This hole was cored to 220 mbsf using the APC and XCB (Table T1). Six in situ temperature runs were made at this site using the APCT tool, including a dedicated mudline run; two DVTP runs were also made. No in situ pressure measurements were made at this site.

The PCS was deployed three times at Site 1247. Two of these deployments recovered core under pressure; however, the ball valve did not fully close during the other deployment.

Hole 1247B was logged using the triple combination (triple combo) and Formation MicroScanner (FMS)-sonic tool strings. After wireline logging, a vertical and an offset vertical seismic profile (VSP) covering the interval of 104–214 mbsf was acquired by alternately shooting from the *JOIDES Resolution* and the *Ewing,* which held station ~700 m away. Plans to conduct walkaway VSPs were abandoned when the Schlumberger Vertical Seismic Imager (VSI) would no longer clamp in the hole (see "Downhole Tools and Pressure Coring," p. 17).

LITHOSTRATIGRAPHY

Site 1247 is located between Sites 1245 and 1248 just east of the crest of southern Hydrate Ridge (see Figs. F1, p. 51, and F7, p. 57, both in the "Leg 204 Summary" chapter). Two holes were drilled at Site 1247. One hole was logged by LWD (Hole 1247A), and one was cored (Hole 1247B) to a depth of 220.0 mbsf. Seismic reflection profiles show that Horizon A, cored at Sites 1245, 1248, and 1250, is present at Site 1247 as well (see Fig. F6, p. 56, in the "Leg 204 Summary" chapter). Although the seismic amplitude and LWD response of Horizon A in Hole 1247A are similar to those exhibited at Sites 1245, 1248, and 1250, the lithologic manifestation of the horizon differs significantly in Hole 1247B from that observed at the other sites. Note that the seismic character of this horizon also differs significantly between the two holes drilled at this site (Fig. F2).

Three lithostratigraphic units were defined at Site 1247 (Figs. F3, F4) based on variations in sedimentologic criteria such as grain size and biogenic components, as well as on geochemical parameters, such as calcium carbonate content (expressed as $CaCO_3$ weight percent), total organic carbon (TOC), and mineralogy from X-ray diffraction (XRD). Lithostratigraphic Unit I is composed of a section of uninterrupted dark greenish gray diatom-bearing clay. Lithostratigraphic Units II and III are composed of dark greenish gray diatom-bearing clay with abundant silt and sand turbidites. Lithostratigraphic Unit III was further subdivided into two subunits (Subunits IIIA and IIIB) on the basis of biogenic content. We also compare and correlate our results with the 3-D seismic reflection data, downhole LWD data (density and resistivity), and physical property measurement (magnetic susceptibility [MS]) to better define the entire stratigraphic sequence (Fig. F4). Correlation of the lithostratigraphic units defined here with the other Leg 204 sites is summarized in Figure F10, p. 60, in the "Leg 204 Summary" chapter.

Lithostratigraphic Units

Lithostratigraphic Unit I

Interval: Core 204-1247B-1H through Section 204-1247B-5H-2
Depth: 0.00–27.00 mbsf
Age: middle Pleistocene–Holocene

Good core recovery suggests that a complete record of lithostratigraphic Unit I was recovered at Site 1247 and can be correlated to the uppermost lithostratigraphic units recovered at Sites 1245 and 1250 (see Fig. F10, p. 60, in the "Leg 204 Summary" chapter). Lithostratigraphic Unit I consists of dark greenish gray (5GY 4/1) hemipelagic clay and silty clay with a low total biogenic content (<10%) as determined by smear slide analysis, although diatoms are present throughout. Authigenic carbonate precipitates are common, primarily as light-colored cements in Sections 204-1247B-1H-1 and 2H-4 (Fig. F5); sulfide mineralization and bioturbation increase toward the base of lithostratigraphic Unit I. The lower boundary of lithostratigraphic Unit I is defined by the first occurrence of coarse grain-size sediments at ~27 mbsf in Core 204-1247B-5H (Fig. F3).

The clay content of lithostratigraphic Unit I varies between 70% and 80% in the major lithology. Silt-size components compose the remaining 20%–30% of the lithology, with sand-size particles present only in trace amounts (0%–3%) (Fig. F3). The predominant minerals identified from smear slides are quartz, feldspar, and opaque and clay minerals. Opaque grains, associated with zones of sulfide precipitates, are commonly irregular and framboidal forms. The onset of the first zone of major sulfide precipitates and bioturbation in lithostratigraphic Unit I occurs in Core 204-1247B-3H and corresponds to a peak in the MS data at ~21 mbsf (see "Magnetic Susceptibility," p. 16, in "Physical Properties").

The calcium carbonate content (see "Carbon Analyses, Elemental Analyses, and Rock-Eval Characterization," p. 14) of lithostratigraphic Unit I remains relatively constant despite the presence of authigenic carbonate found in both Cores 204-1247B-1H and 2H (Fig. F6); however, this may be an effect of sparse sampling. The carbonate-rich zones were initially identified by their light color in the cores (Fig. F5). Smear slides analyzed from these patches indicate these zones contain

F3. Lithostratigraphic summary, p. 29.

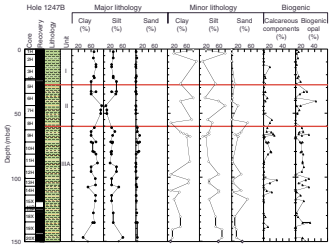

F4. Seismic reflection profile and LWD data, p. 31.

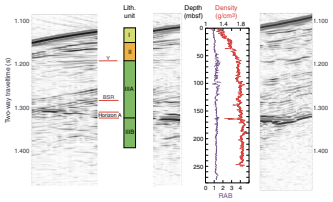

F5. Authigenic carbonate cement, p. 32.

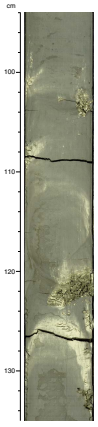

F6. $CaCO_3$ vs. depth, p. 33.

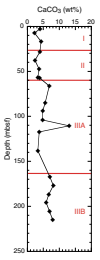

70%–90% authigenic carbonate in needlelike grains that are typically 1–5 µm long, and XRD analysis indicates that the carbonates are primarily calcitic, though both Samples 204-1247B-2H-1, 43–44 cm, and 2H-4, 55–56 cm, have two phases (Fig. F7). Of the XRD samples analyzed shipboard from Site 1247, only Sample 204-1247B-2H-4, 124–125 cm, contains carbonate of a dolomitic composition (Fig. F7).

The total biogenic component of lithostratigraphic Unit I, consisting of diatoms, siliceous microfossils, foraminifers, and calcareous nannofossils, does not exceed 10% of the total sediment (Fig. F3). Cores 204-1247B-1H, 3H, and 5H contain the highest percentage of biogenic components, with diatoms composing 5%–8% of the major lithology in Cores 204-1247B-1H and 5H. Carbonaceous nannofossils and foraminifers compose 10% of the major lithology in Core 204-1247B-3H.

F7. XRD record from carbonate samples, p. 34.

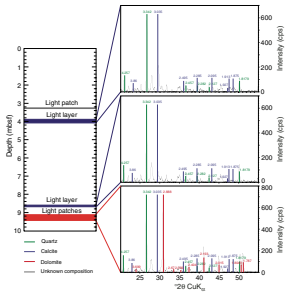

Lithostratigraphic Unit II

Interval: Sections 204-1247B-5H-2 through 8H-5
Depth: 27.00–60.00 mbsf
Age: middle Pleistocene

Lithostratigraphic Unit II is composed of dark greenish gray (5GY 4/1) diatom-bearing to diatom-rich silty clay with graded silt and sand turbidites. Authigenic carbonates in lithostratigraphic Unit II are few and are present only in Core 204-1247B-6H. Lithostratigraphic Unit II also contains more sulfide precipitates than lithostratigraphic Unit I. The top of lithostratigraphic Unit II is defined by the first occurrence of a fining-upward clayey silt layer in Section 204-1247B-5H-2 at 27 mbsf. The frequency of turbidites increases toward the base of the lithostratigraphic unit (~60 mbsf). This depth corresponds to the location of seismic Horizon Y, a regional unconformity best identified on the 3-D seismic reflection data (see Fig. F6, p. 56, in the "Leg 204 Summary" chapter).

The major lithology of lithostratigraphic Unit II is diatom-bearing to diatom-rich silty clay (contains 20%–40% silt-size grains) punctuated by fining-upward sequences of clayey silt to silt to silty sand (Fig. F3). The coarse-grained minor lithologies typically have erosional basal contacts. They are often <0.5 cm thick but can grade upward over 10 cm or more and are interpreted as turbidites (Cores 204-1247B-5H and 6H). Soft-sediment deformation features and mud clasts, representative of a debris flow deposit, were observed at ~29 mbsf, just below the onset of the silt and sand interlayers.

Both the major and minor lithologies of lithostratigraphic Unit II are composed of quartz, feldspar, and opaque and clay minerals. The grain size of the minor lithologies in lithostratigraphic Unit II ranges from clayey silt (containing 40% clay-size grains) to sandy silt (containing 40% sand-size grains). Trace quantities of glauconite (<5%) were observed in the minor lithology of Cores 204-1247B-5H, 6H, and 8H. This glauconite is associated with the coarse-grained material at the bases of turbidites and is likely detrital rather than authigenic.

The biogenic content of lithostratigraphic Unit II, composed of diatoms, siliceous microfossils, calcareous nannofossils, and foraminifers, ranges from 5% to 35% of the total sedimentary components and is consistently higher than that of lithostratigraphic Unit I (Fig. F3). Diatoms were observed in every smear slide from the major lithology of lithostratigraphic Unit II, although they were typically absent from the minor lithology (Fig. F3). Calcareous nannofossils, unlike diatoms, are limited to the minor lithology of lithostratigraphic Unit II. Macroscopic

foraminifers are also found predominantly in the minor lithology, although microscopic foraminifers compose 3% of the major lithology in Core 204-1247B-5H.

Sulfide precipitates are common in lithostratigraphic Unit II and correlate well with high values in MS (see **"Magnetic Susceptibility,"** p. 16, in "Physical Properties"). A 10-cm-long vein of pyrrhotite dipping at 45° on the core face was observed in Section 204-1247B-5H-6 at ~31 mbsf (Fig. **F8**) and was recorded in a high-resolution MS scan, performed every 1 cm (10-s count interval). The result of this study confirmed the influence of sulfide precipitates on full-core MS records. Below the pyrrhotite vein, the whole-core MS data show more frequent and higher-amplitude peaks than those above 33 mbsf. The change in magnitude and frequency of the magnetic highs probably is a result of the combined effect of frequent turbidite layers and increased sulfide precipitates, both of which characterize lithostratigraphic Unit II.

F8. Pyrrhotite vein, p. 35.

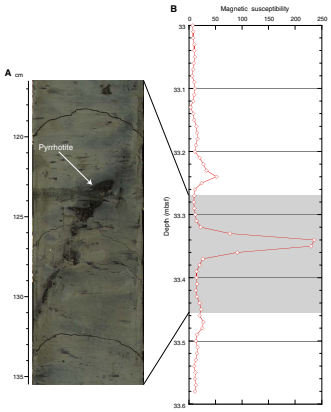

Lithostratigraphic Unit III

Intervals: Sections 204-1247B-8H-5, 90 cm, through 27X-CC
Depth: 60.00–220.62 mbsf
Age: early–middle Pleistocene

Lithostratigraphic Unit III is composed of dark greenish gray (5GY 4/1) diatom-bearing to diatom-rich clay and silty clay (Fig. **F3**). The core recovery of the unit was very good (96%). Although lithostratigraphic Unit III is dominantly composed of diatom-bearing to diatom-rich clay and silty clay, it also contains abundant layers of fining-upward parallel-bedded silt to sand, interpreted as turbidites, some sulfides, and rare to moderate bioturbation. The major components of the clay and silty clay, as determined by XRD analyses, are quartz, feldspar, muscovite, illite, other clay minerals, and probably biogenic calcite in varying amounts.

The upper boundary of lithostratigraphic Unit III is defined by an increase in the sand fraction of the major lithology of up to 10% (~60–80 mbsf) as well as an increase in biogenic calcareous and siliceous components of up to 20% (~60–70 mbsf) (Fig. **F3**). The boundary between lithostratigraphic Units II and III correlates with seismic Horizon Y. This reflector is seen in the 3-D seismic data and is interpreted to be an unconformity at this site.

Lithostratigraphic Unit III is divided into two subunits (Subunits IIIA and IIIB), based on the increase in calcareous biogenic components in Subunit IIIB and the correlation with 3-D seismic data. The boundary between the two subunits lies at 163.50 mbsf (in Section 204-1247B-22X-1) and corresponds to the first occurrence of nannofossil-rich clay.

Lithostratigraphic Subunit IIIA

The major lithology of lithostratigraphic Unit IIIA (60.00–163.50 mbsf) is diatom-bearing to diatom-rich clay and silty clay (Fig. **F3**). Cores 204-1247B-9H and 10H are also nannofossil bearing and foraminifer bearing to nannofossil rich. Smear slide analyses indicate that lithostratigraphic Subunit IIIA is composed of up to 97% clay, though more typically it contains ~20% silt and >10% sand. The major nonbiogenic components of lithostratigraphic Subunit IIIA are feldspar, quartz, and clay and opaque minerals.

The diatom-bearing to diatom-rich clay and silty clay is punctuated by 1- to 10-cm-thick turbidites composed of foraminifer-bearing to foraminifer-rich and diatom-bearing to diatom-rich silty-sandy clay and

clayey-sandy silt to sand. These turbidites are present as planar-laminated fining-upward sequences, with event spacing varying from 2 cm to 2 m.

The minor lithology in Sections 204-1247B-20X-2 through 20X-4 contains minor amounts of volcanic glass (<5%) in thin layers or lenses (1 mm). Wood fragments were found in interval 204-1247B-8H-6, 140–142 cm. Two hydrate samples were recovered in lithostratigraphic Subunit IIIA in Sections 204-1247B-12H-2 and 14H-5 and correspond to an observed increase in biogenic calcareous and siliceous components at 100–120 mbsf (Fig. F3). Macroscopic foraminifers were found in the coarse fraction (minor lithology) of Cores 204-1247B-23X and 26X. The moderate to rare abundance of sulfides in Core 204-1247B-18X responsible for the dark gray (N3) color of the sediments, seems to correlate with a high in the MS data (see **"Magnetic Susceptibility,"** p. 16, in "Physical Properties"). A series of clay clast–rich deposits we interpret as a debris flow deposit is present between 156 and 161 mbsf (Sections 204-1247B-21X-2, 72 cm, through 21X-5, 140 cm) at the base of Subunit IIIA (Fig. F9). This debris flow consists of five layers ranging from 0.1 to 2 m thick and is correlated with Horizon A, a bright regional seismic reflector. The clayish matrix of the debris flow contains clasts (1–5 cm) of a slightly lighter color and different composition (foraminifer- and diatom-bearing clay) that lack volcanic glass. The upper and lower contacts of the debris flow are sandy-silty turbidites that also lack volcanic glass. At Sites 1245, 1248, and 1250, however, Horizon A is present as a series of volcanic glass–rich and ash sequences and is a bright reflection on the 3-D seismic section. The difference in the lithologic manifestation of Horizon A between Site 1247 and all other sites at which it was drilled corresponds to a change in the character of the seismic horizon in Hole 1247B where the reflector is more washed out (Fig. F2).

F9. Debris flow deposit, p. 36.

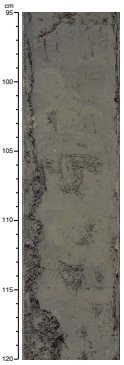

Lithostratigraphic Subunit IIIB

Lithostratigraphic Subunit IIIB is distinguished from Subunit IIIA by a distinct increase in biogenic calcareous components, which reach up to 50% in the minor lithology (Section 204-1247B-23X-4 [177.6 mbsf]) (Fig. F3). However, the major lithology of lithostratigraphic Subunit IIIB (163.50–220.62 mbsf) is nannofossil-bearing to nannofossil-rich clay and silty clay (Fig. F3). Cores 204-1247B-22X and 23X are foraminifer bearing to foraminifer rich, and Cores 24X through 26X are diatom bearing. Smear slide analyses indicate that lithostratigraphic Subunit IIIB is composed of up to 90% clay, though more typically it contains 20%–30% silt components and up to 10% sand. The major nonbiogenic components of lithostratigraphic Subunit IIIA are feldspar, quartz, and clay and opaque minerals.

The nannofossil-bearing to nannofossil-rich clay and silty clay is interbedded with 1- to 12-cm-thick layers of foraminifer-bearing to foraminifer-rich clay, nannofossil-bearing and diatom-bearing to diatom-rich silty clay, and clayey-sandy silt to silty sand. These coarser-grained layers are present as planar-laminated fining-upward sequences (turbidites) and contain macroscopic foraminifers (Fig. F10) in Sections 204-1247B-23X-1, 23X-4, 26X-2, 26X-4, and 26X-5. The erosional bases of turbidites are visible in Core 204-1247B-23X. The turbidites of lithostratigraphic Subunit IIIB are present at a lower frequency than those in lithostratigraphic Subunit IIIA. Single turbidite interlayers have event spacing between 0.20 and 6 m. Cores 204-1247B-23X and 24X (180–186 mbsf) show abundant bioturbation and sulfides. The high sulfide

F10. Sandy turbidite, p. 37.

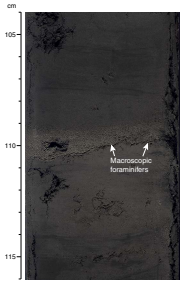

content generally correlates with highs in the MS (see "Magnetic Susceptibility," p. 16, in "Physical Properties").

Sedimentary Evidence of Gas Hydrate

There was little evidence for the presence of gas hydrate at this site. No mousselike or soupy textures were observed, although hydrate samples suspected to contain hydrate were taken on the catwalk from Cores 204-1247B-12H and 14H in lithostratigraphic Subunit IIIA, just above depth of the BSR.

Environment of Deposition

Consistent with the lithostratigraphic unit boundaries at Sites 1245, 1248, and 1250, Unit III at Site 1247 is placed below the unconformity and Units II and I above the unconformity at Horizon Y (Figs. F3, F4). Lithostratigraphic Unit III was subdivided at Horizon A into Subunits IIIA and IIIB (Figs. F3, F4). The stratigraphy present at this site is similar to that at the other sites cored near the southern summit of Hydrate Ridge, with variations in grain size and biogenic content suggestive of an active slope basin or abyssal plain environment of deposition.

Although Horizon A has a strong seismic amplitude in Hole 1247A and was also detected as a density low on the LWD density log (see "Downhole Logging," p. 19), the location of Hole 1247B was west of Hole 1247A, in a region where the amplitude of Horizon A decreases abruptly (Fig. F2). The depth of Horizon A in Hole 1247B is ~158 mbsf. Interestingly, the volcanic glass–rich horizons, which are present at Horizon A at Sites 1245, 1248, and 1250, were not observed here. Instead, a debris flow, bound by turbidites free of volcanic glass, was identified at 156–161 mbsf; a debris flow lacking volcanic glass is most likely the cause of the apparent decrease in seismic amplitude of Horizon A in Hole 1247B. A lateral variation of sedimentary facies resulting from local factors (e.g., original topography and/or turbidite-channel sedimentary pathways) may explain why a debris flow was deposited at Site 1247, whereas an ash-rich sequence was deposited at Sites 1245, 1248, and 1250.

A good correlation between MS and turbidite sequences, sulfide precipitates, or both is also observed at Site 1247. Because most, if not all, of the high MS peaks at Site 1247 are coincident with either sands and silts bearing magnetic minerals transported via turbidity currents and/or clays rich in magnetic iron sulfide precipitates formed in situ (pyrrhotite); therefore, changes in their magnitude and recurrence interval must be interpreted carefully. The turbidites above and below the debris flow at Horizon A, for example, are seen as high-amplitude spikes in the MS data, whereas the clay-rich low-sulfide debris flow shows low MS (see "Magnetic Susceptibility," p. 16, in "Physical Properties"). The high susceptibility from 210 mbsf to the end of the core is also caused by turbidites. In contrast, the high susceptibility seen from 180 to 190 mbsf is caused by the presence of abundant sulfide.

At Site 1245, Horizon Y represents an angular unconformity or a thrust fault (see "Environment of Deposition," p. 10, in "Lithostratigraphy" in the "Site 1245" chapter); however, at Site 1247, lithostratigraphic Units II and III are disconformable at Horizon Y (60 mbsf) thereby making it more difficult to detect within the stratigraphic record. A slightly higher frequency of turbidites is observed above Horizon Y than below. This change is associated with a decrease in sulfide

abundance across the boundary and the onset of foraminifers within the turbidites at 54 mbsf. These observations may indicate that there is a higher sedimentation rate above Horizon Y and that the sediments are more susceptible to sulfide mineralization. The onset of foraminifers within the turbidites at 54 mbsf at Site 1247 may indicate a change in the source area or in the productivity of this microfossil group, either of which can vary in space and time and thus are not diagnostic evidence for the presence of an unconformity. The best evidence for an unconformity or thrust fault origin for Horizon Y comes from the seismic profiles that cross Site 1245, which depict the angular bedding relationships (see Fig. F5, p. 55, in the "Leg 204 Summary" chapter).

BIOSTRATIGRAPHY

Site 1247 is located on the eastern flank of the summit of southern Hydrate Ridge. Two holes were drilled at Site 1247, and one hole (Hole 1247B) was cored from the seafloor to 220 mbsf. The biostratigraphy determined for Site 1247 was based on examination of diatoms and calcareous nannofossils from all core catcher samples from Holes 1247B. Calcareous nannofossils were also examined in smear slide samples collected by the sedimentologists.

Diatoms

Hole 1247B yields few to common and poorly to moderately preserved diatoms, except in the intervals from Samples 204-1247B-22H-CC to 24H-CC, where diatoms are rare. Diatom assemblages in Hole 1247B are dominated by species such as *Stephanopyxis dimorpha, Stephanopyxis* spp., *Neodenticula seminae,* and *Thalassionema nitzschioides*. Warm-water species, such as *Fragilariopsis doliolus* and *Thalassiosira oestrupii,* are frequently present throughout the sediment sequence recovered.

The interval from the seafloor to 35.02 mbsf contains *N. seminae* but does not contain *Proboscia curvirostris*. This interval was assigned to North Pacific Diatom Zone (NPD) 12 (*N. seminae* Zone). *P. curvirostris* is present almost continuously from Samples 204-1247B-6H-CC to 27X-CC (44.37–220.57 mbsf). The last occurrence (LO) of *P. curvirostris* was placed between Samples 204-1247B-5H-CC (35.02 mbsf) and 6H-CC (44.47 mbsf). Rare *Actinocyclus oculatus* is present from Samples 204-1247B-10H-CC (81.90 mbsf) and 13H-CC (106.72 mbsf); thus, the LO of *A. oculatus* was placed between Samples 9H-CC (72.26 mbsf) and 10H-CC (81.90 mbsf). The interval below the LO of *A. oculatus,* from 81.90 mbsf to the bottom of Hole 1247B, was assigned to NPD 10 (*A. oculatus* Zone) based on the presence of *A. oculatus* and the absence of *Neodenticula koizumii* in this interval. The presence of *P. curvirostris* in the interval from 44.37 mbsf to the bottom of Hole 1247B means that the sediment sequence at Site 1247 is younger than 1.6 Ma.

Calcareous Nannofossils

The calcareous nannofossil biostratigraphy for Site 1247 was based on an investigation of all core catcher samples from Hole 1247B. In addition, the smear slides taken for sedimentologic descriptions, which were distributed throughout the cores, were also examined. Generally, the intervals are barren or have trace abundances of calcareous nanno-

fossils from the seafloor down to 44.37 mbsf, whereas the intervals are rarely to commonly present from 47.35 to 220.57 mbsf, except in a few short intervals (e.g., 90.49–100.40 mbsf) that contain trace calcareous nannofossils.

The core catcher samples taken from the interval of 3.55–22.93 mbsf (Samples 204-1247B-1H-CC to 3H-CC) contain no or trace calcareous nannofossils. *Emiliania huxleyi* was found in a few smear slides produced for the sedimentological study from the same interval. The LO of *E. huxleyi* was placed in Sample 204-1247B-5H-CC (35.02 mbsf); consequently, the interval from the seafloor to 35.02 mbsf was assigned to Zone NN21. The underlying interval between Samples 204-1247B-6H-5, 36 cm, and 7H-3, 80 cm (40.46–47.35 mbsf), does not contain *Pseudoemiliania lacunosa*. A few *P. lacunosa* specimens are infrequently present from 47.35 to 53.08 mbsf; reworked early Pleistocene species, such as *Calcidiscus macintyrei, Helicosphaera sellii,* and large-sized *Gephyrocapsa lumina,* are also present in rare abundance. Therefore, the trace and infrequent presence of *P. lacunosa* in this interval could also be the result of reworking. The reworking of this interval is supported by the sedimentologic data, which suggests that the frequency of turbidites increased toward Horizon Y at 60 mbsf (see **"Lithostratigraphy,"** p. 2). On the other hand, *P. lacunosa* is present in rare abundance from 63.08 mbsf down to the bottom of Hole 1247B, allowing us to place the LO of *P. lacunosa* at 63.08 mbsf. Consequently, the zonal boundary between NN20 and NN19 was placed at 63.08 mbsf. Abundant, various, small *Gephyrocapsa* species are present in the interval from 107.59 to 151.36 mbsf (Samples 204-1247B-14H-1, 89 cm, to 20X-6, 57 cm), assigning this interval to the mid-Pleistocene small *Gephyrocapsa* spp. Acme Zone (1.0–1.2 Ma). In consequence, the depths of 107.59 and 151.36 mbsf were determined as the upper level (1.0 Ma) and the lower level (1.2 Ma) of the small *Gephyrocapsa* spp. Acme Zone, respectively. The LO of *C. macintyrei* (1.59 Ma) was recognized in Sample 204-1247B-22X-CC (171.97 mbsf). Rare to common *G. lumina* is present in Sample 204-1247B-27X-CC (220.57 mbsf), assigning the bottom of Hole 1247B to the lower part of Pleistocene Zone NN19, with an age younger than 1.67 Ma.

Summary

Based on analysis of diatoms and calcareous nannofossils from Hole 1247B, seven microfossil events (two diatom and five nannofossil events) were recognized (Table **T2;** Fig. **F11**). The age of the bottom sediments (220.57 mbsf) in Hole 1247B was estimated to be younger than 1.6 Ma, based on diatom assemblage, or to be younger than 1.67 Ma, based on nannofossil assemblage. This means that the 220-m-thick sequence at Site 1247 is early Pleistocene–Holocene in age.

We estimated the linear sedimentation rates using these events. The sedimentation rates are 13 cm/k.y. for the interval from the top of 1247B to 60 mbsf, 9 cm/k.y. for the interval from 60 to 110 mbsf, 22 cm/k.y. for the interval from 110 to 150 mbsf, and 4 cm/k.y. for the interval from 150 to 170 mbsf.

INTERSTITIAL WATER GEOCHEMISTRY

Site 1247 was cored to a TD of 220 mbsf (Hole 1247B). The interstitial water (IW) program at this site was aimed at providing geochemical

T2. Bioevents, p. 71.

F11. Age-depth plot, p. 38.

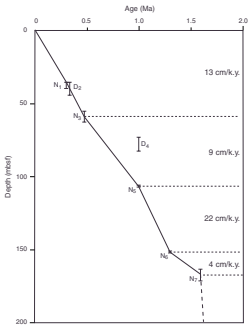

proxies for the presence and abundance of gas hydrate and to establish constraints on the updip fluid flow along a sedimentary sequence imaged by the seismic reflector known as Horizon A. This horizon is present at 160 mbsf at this site (see "Introduction," p. 1) and was previously sampled from 176 to 183 mbsf at Site 1245 (see "Lithostratigraphy," p. 3, in the "Site 1245" chapter). We recovered 48 IW samples at a frequency of approximately two whole-round samples per core in the upper 140 mbsf, followed by a sampling resolution of one whole-round sample per core below this depth. The IW geochemistry data are tabulated in Table T3 and are illustrated in Figure F12.

Chloride Concentration and the Presence of Gas Hydrate

The presence of excursions with low-chloride values above the BSR can be used to infer the presence and amount of gas hydrate in the sediments (see "Interstitial Water Geochemistry," p. 13, in the "Explanatory Notes" chapter and "Interstitial Water Geochemistry," p. 13, in the "Site 1244" chapter). At Site 1247, freshening chloride anomalies predict the presence of gas hydrate between ~51 and 116 mbsf. Thermal image data obtained with the IR camera suggest that hydrate is present in two major zones: the intervals between 40 and 50 mbsf and between 90 and 120 mbsf. The anomalies in the chloride content of the pore fluids (Fig. F13), however, only show the large effects of gas hydrate dissociation in the interval ranging from 110 to 120 mbsf. This discrepancy reflects the resolution limitations of the chloride anomaly technique in identifying zones of gas hydrate when it is present as distinct thin layers within the core. Any chloride anomaly associated with layered gas hydrates can only be detected if the pore water sample is collected within ~10 cm of the hydrate layer, as illustrated with a high-resolution experiment at Site 1245 (see "Interstitial Water Geochemistry," p. 13, in the "Site 1245" chapter). Thus, a sampling resolution of two samples per core (i.e., a sample approximately every 4.5 m) can easily fail to identify discrete hydrate horizons.

The chloride anomalies measured in two samples recovered from near the base of the gas hydrate stability zone (GHSZ) indicate that gas hydrate occupies ~10% of the pore space, as illustrated in Figure F13. More commonly, the chloride data suggest that gas hydrates occupy between 0% and 2% of the pore space within the GHSZ.

Sulfate, Methane, and the Sulfate/Methane Interface

High-resolution sampling in Hole 1247B allows firm characterization of sulfate and methane profiles as well as identification of the sulfate/methane interface (SMI) (Fig. F14). Sulfate generally decreases downcore within the sulfate-reduction zone as sulfate is removed from the sediments by sulfate reducers. The sulfate profile is linear between 6 and 9 mbsf, with strong curvature above 6 mbsf and below 9 mbsf. Minimal sulfate values combined with a rapid increase in methane headspace concentrations (see "Organic Geochemistry," p. 12) locate the SMI at ~11 mbsf.

Although the sulfate profile shows curvature, the distinct linear portion of the curve may be caused by anaerobic methane oxidation (AMO) at the SMI. Following the method outlined at Site 1244 (see "Interstitial Water Geochemistry," p. 13, in the "Site 1244" chapter)

T3. Dissolved species in pore waters, p. 72.

F12. Dissolved species in pore waters, p. 39.

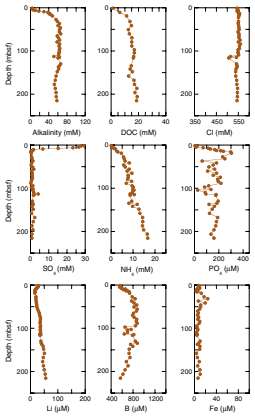

F13. Chloride concentration profile, p. 41.

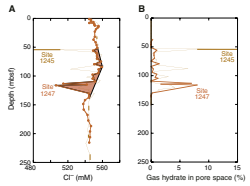

F14. Sulfate and methane concentration profiles, p. 42.

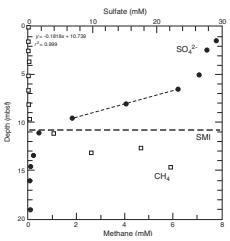

(Borowski et al., 1996), we can estimate methane flux of 2.5×10^{-3} mM/cm^2/yr, based on a sulfate gradient of 5.5 mM/m (Fig. F14), a sulfate diffusion coefficient of 5.8×10^{-6} cm^2/s at 5°C, and average porosity of 63% (see "Physical Properties," p. 14). This estimated a methane flux is approximately the same as that calculated for Site 1244, ~30% less than that at Site 1251 and ~1.4 times greater than that estimated at the Blake Ridge.

These estimates assume methane delivery through diffusion only and that the linear portion of the sulfate profile represents sulfate demand at the SMI. If significant water or methane advection occurs or if sulfate depletion through AMO is of minor importance, then this estimate is invalid. The role of AMO in sulfate depletion can be assessed with knowledge of the isotopic composition of the methane gas and that of the dissolved inorganic carbon, sulfate, and sulfide, which will be carried out postcruise.

Major and Minor Element Distributions

Diagenetic effects associated with carbonate geochemistry are apparent in the distributions of dissolved strontium and magnesium. These elements show a marked decrease in their concentrations in pore waters from ~8 to 15 mbsf, probably associated with the formation of authigenic carbonates such as those recovered at 19 mbsf (see "Lithostratigraphy," p. 2). Another zone marked by low strontium and magnesium concentrations is apparent below 160 mbsf, a zone that also shows a decrease in pore fluid alkalinity (Fig. F12). This zone corresponds to lithostratigraphic Unit III and is characterized by an increase in the nannofossil content of the sediments (see "Lithostratigraphic Unit III," p. 5, in "Lithostratigraphic Units" in "Lithostratigraphy"). It is possible that this biogenic component provides nucleation sites for authigenic carbonate formation, as previously discussed for Site 1245.

Dissolved iron and manganese have similar profiles, showing a coincident increase in their concentrations from the seafloor to ~30 mbsf (Fig. F12). This distribution is likely to reflect remobilization from iron-manganese minerals, which precipitate as sulfides below the SMI. Similar distributions have been observed at Sites 1244–1246 (see "Interstitial Water Geochemistry," p. 13, in the "Site 1244" chapter; "Interstitial Water Geochemistry," p. 13, in the "Site 1245" chapter; and "Interstitial Water Geochemistry," p. 7, in the "Site 1246" chapter). Postcruise analyses of the distribution and isotopic characterization of dissolved sulfide and of solid phases will provide constraints on the nature on the Fe-Mn biogeochemical cycling at sites drilled during Leg 204.

In the near-surface sediments, barium has very low concentrations (Fig. F12), as expected in pore waters where dissolved sulfate is present (see "Interstitial Water Geochemistry," p. 13, in the "Site 1244" chapter). As sulfate is depleted, barium shows a marked increase to values >100 µM at depths below 25 mbsf. Of particular interest is the increase in dissolved barium observed between 130 and 140 mbsf, where it reaches 200 µM. A similar increase just below the base of the GHSZ was observed at Site 1245, with dissolved barium concentrations as high as 250 µM. This increase might reflect migration of barium-enriched fluids from deep sequences to the depth of the BSR, where gas hydrates serve as a barrier to upward fluid flow.

Dissolved lithium generally increases in concentration with increasing depth. Superimposed on this trend, lithium shows an enrichment

in the pore fluids recovered from the depth of the seismic reflector known as Horizon A (160 mbsf) (see **"Introduction,"** p. 1). A similar increase associated with Horizon A was observed at Site 1245 (Fig. **F15**). This increase suggests migration of lithium-enriched fluids from depths >1 km, where burial temperature exceeds the 80°C threshold needed for lithium release from alumnosilicates (e.g., Edmond et al., 1979; Seyfried et al., 1984). Gases collected from the sediments between the BSR (129 mbsf) and Horizon A (160 mbsf) also show enrichment of heavy hydrocarbons (see **"Hydrocarbon Gases,"** p. 12, in "Organic Geochemistry"), which is consistent with migration of fluids from a deep-seated source. These patterns correspond to observations previously recorded at Site 1245 (see **"Interstitial Water Geochemistry,"** p. 13, in the "Site 1245" chapter).

F15. Lithium concentration profile, p. 43.

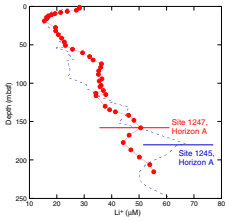

T4. C_1, C_2, and C_3, p. 73.

F16. C_1, C_2, C_3, and $C_{2=}$ vs. depth, p. 44.

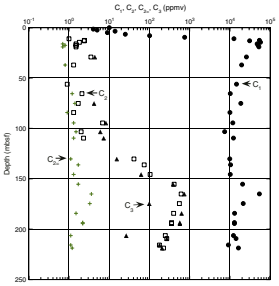

F17. Residual methane and sulfate in pore water, p. 45.

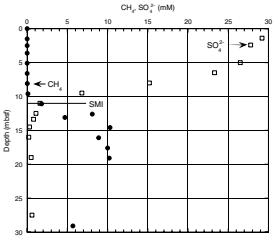

T5. Light hydrocarbon and nonhydrocarbon gases, p. 74.

F18. Light hydrocarbons vs. depth, p. 46.

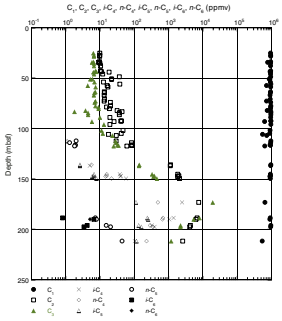

ORGANIC GEOCHEMISTRY

Site 1247 is located northwest of the southern summit of Hydrate Ridge. The shipboard organic geochemistry program at Site 1247 included analyses of hydrocarbon gases, carbonate and organic carbon, and total sulfur and total nitrogen contents. Descriptions of the methods used for these analyses are summarized in **"Organic Geochemistry,"** p. 16, in the "Explanatory Notes" chapter.

Hydrocarbon Gases

Concentrations of methane (C_1), ethane (C_2), ethylene ($C_{2=}$), and propane (C_3) were measured for every core available using the headspace technique. The results are reported in parts per million by volume (ppmv) in Table **T4** and illustrated as ppmv vs. depth in Figure **F16.** Methane content in Hole 1247B varies from 4 to 25 ppmv in the uppermost 6.6 mbsf. It increases to 749 ppmv at 9.6 mbsf and to 12,599 ppmv at 11.1 mbsf. It remains in the range of 10,000–60,000 ppmv to the base of the cored section. In addition to the relative concentration of methane in the headspace vial, the C_1 values are expressed in millimoles per liter (mM) of pore water in Table **T4.** Based on the methane concentration profile, the onset of methanogenesis occurs at a depth of ~11 mbsf in Hole 1247B (Fig. **F17**). Dissolved sulfate in pore water is also essentially consumed by 11 mbsf (see **"Sulfate, Methane, and the Sulfate/Methane Interface,"** p. 10, in "Interstitial Water Geochemistry"). No ethane is detected within the upper 10 mbsf. The concentration of ethane is very low in the samples from 10 to 110 mbsf (0–6.8 ppmv). It increases rapidly to 41.0 ppmv at 130.3 mbsf and to a maximum value of 615.7 ppmv at 165.0 mbsf. Propane is also abundant in this interval (130.3–165.0 mbsf), ranging from 62.3 to 735.7 ppmv. Enrichment of heavy hydrocarbon gases in this interval suggests migration of wet hydrocarbon gases (Fig. **F16**). Ethylene is sporadically present throughout the cored section (0.7–3.6 ppmv) (Table **T4**). The relative richness of ethylene between 165.0 and 174.6 mbsf suggests that the ethylene in this interval may also be related to the migration of wet gases.

High-resolution sampling and analysis of gas voids in cores was carried out to define the gas hydrate occurrence zone (GHOZ) based on gas composition, which is listed in Table **T5** and plotted in Figure **F18.** The contents of methane in the voids from Hole 1247B are generally >900,000 ppmv (>90% by volume) (Fig. **F18**), except for the samples

contaminated with air. The ethane concentration is uniform in the upper 40 mbsf. The first shift in the C_1/C_2 ratio, indicating ethane enrichment perhaps resulting from dissociated gas hydrate, is detected at 44 mbsf. An increase of ethane concentration in void gases is also apparent at depths of ~50 and 80 mbsf. Another slight anomaly is present at ~115 mbsf. Hydrocarbon gases from these depths are characterized not only by an enrichment of ethane but also by a depletion of propane (Table **T5**). Relative enrichment of ethane and depletion of propane may be explained by significant contribution of gas from dissociated Structure I gas hydrate during core recovery. These changes in gas composition show good correlation with IR temperature data (see **"Infrared Scanner,"** p. 14, in "Physical Properties"). We can define the top of the GHOZ at 44 mbsf, based on the composition of void gas data. The base of the GHSZ/GHOZ is usually marked by an order-of-magnitude increase in ethane (e.g., Site 1251) perhaps as a result of its release from dissociated gas hydrates. However, at Site 1247, it is very difficult to define the base of the GHSZ/GHOZ because the depth interval between 120 and 220 mbsf is characterized by an anomalous increase in the amount of thermogenic wet gas hydrocarbon gases (Fig. **F18**). The increase in ethane and propane concentrations in this interval is also apparent in the headspace gas analysis. The thickness of the anomalous zone for heavy hydrocarbon gases is greater at Site 1247 than at Site 1245, and C_{4+} hydrocarbons are also more abundant. Based on this abundance of C_{4+} hydrocarbon gases, Site 1247 appears to be closer to the source of migrating hydrocarbons than Site 1245. Horizon A or another permeable layer below Horizon A may act as a migration conduit to facilitate the transport of thermogenic hydrocarbons from greater depths.

Gas composition as expressed by the C_1/C_2 ratio of headspace and void gases is plotted vs. depth in Figure **F19.** The C_1/C_2 ratio for void gas samples shows a shift to lower values that indicates the effect of gas from decomposed gas hydrate. A decrease of the C_1/C_2 ratio presumably from migrated thermogenic ethane is also distinctive at depths ranging from 130 to 220 mbsf.

The C_1/C_2 ratio is plotted vs. estimated sediment temperature in Figure **F20.** The C_1/C_2 vs. temperature plot shows evidence for migrated hydrocarbons in the depth interval from ~130 to 220 mbsf, as indicated by ratios that are too low for the prevailing sediment temperature.

Gas Hydrate and Pressure Cores

Gas hydrate pieces and gas hydrate–bearing sediments were recovered at Site 1247 in cores sampled on the catwalk. Two samples were analyzed to determine the gas composition associated with the dissociation of a gas hydrate (piece recovered from Section 204-1247B-12H-4) (Table **T6**). The gas from this gas hydrate sample shows enrichment of ethane and depletion of propane relative to what is believed to be the composition of dissolved gas in the core. The composition of the gas derived from the dissociated gas hydrate is consistent with a Structure I methane hydrate. On the C_1/C_2 plot (Fig. **F19**), the hydrate-bound gas falls on the trend of void gas samples also believed to be derived from gas hydrates and is enriched in ethane compared to "baseline" C_1/C_2 ratios of dissolved gas.

Two deployments of the PCS successfully retrieved full (1 m long) cores from depths of 23.1 and 123.8 mbsf. The composition of gas sam-

F19. C_1/C_2 ratio vs. depth, p. 47.

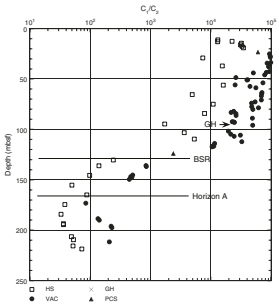

F20. C_1/C_2 ratio vs. temperature, p. 48.

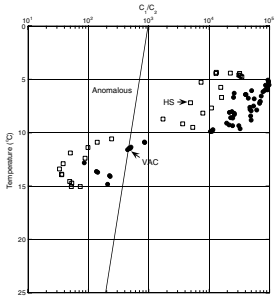

T6. Gas from decomposed gas hydrate, p. 75.

ples obtained during controlled PCS degassing experiments is listed in Table T7. Core 204-1247B-16P (123.8 mbsf) shows sufficient gas content to confirm the subsurface presence of methane hydrate (see "Downhole Tools and Pressure Coring," p. 17). Based on the volume-averaged composition, the C_1/C_2 ratio of this sample is similar to the C_1/C_2 ratio in void gases from adjacent depths (Fig. F19).

T7. Composition of PCS gas samples, p. 76.

Carbon Analyses, Elemental Analyses, and Rock-Eval Characterization

A total of 21 sediment samples were analyzed for carbonate carbon (IC), total carbon, organic carbon (OC), total nitrogen, and total sulfur. The results are listed in Table T8 and plotted in Figure F21. IC varies from 0.27 to 1.57 wt%, with the maximum value at 110.46 mbsf. When calculated as $CaCO_3$, the IC content of the sediment varies from 2.24 to 13.07 wt% (Fig. F21).

T8. IC, TC, OC, TN, and TS, and C/N ratios, p. 77.

F21. IC, OC, TN, TS, and C/N ratios, p. 49.

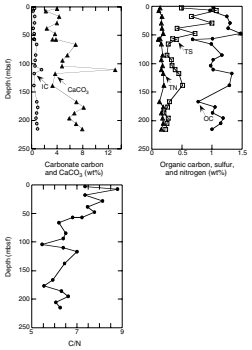

OC content varies from 0.68 to 1.48 wt% and averages 1.09 wt% (Table T8; Fig. F21). The C/N ratio is <10, suggesting that marine organic matter is dominant. Nitrogen in the sediments ranges from 0.10 to 0.20 wt% (Table T8; Fig. F21). The nitrogen data show no apparent trends vs. either depth or OC content. The total sulfur contents vary from 0.20 to 1.07 wt% (Table T8).

The results of Rock-Eval pyrolysis of selected samples are given in Table T9. This analysis was performed in part to evaluate the possible presence of migrated liquid hydrocarbons. Although the production index values seem moderately elevated (i.e., >0.1), they are fairly typical for continental margin sediments cored by the Ocean Drilling Program (ODP). There is no correlation between increased C_{2+} gas components and higher production index values and no definitive evidence for oil staining.

T9. Rock-Eval pyrolysis of samples, p. 78.

PHYSICAL PROPERTIES

Only one hole was cored at Site 1247 in addition to the first hole drilled for the LWD program. Hole 1247B generally had good core recovery, but one core was not fully recovered around the BSR (at 124 mbsf). Standard procedures were used to measure the physical properties on recovered cores (see "Physical Properties," p. 22, in the "Explanatory Notes" chapter). Hole 1247A, where the LWD data were acquired, is offset from Hole 1247B by 87 m. A complete set of IR images was acquired with the track-mounted camera prior to and after sectioning the core liner on the catwalk. In addition, the hand-held IR camera was used for quick identification of cold anomalies associated with the presence of hydrate. At this site, only two hydrate samples were recovered.

Infrared Scanner

IR imaging provided rapid identification of hydrate on the catwalk. The track-mounted IR camera was used twice, both prior to and after sectioning the core liner. The second scan could then be directly correlated to the visual core descriptions and especially to the presence of the mousselike texture that is indicative of the presence of hydrate.

Data from the first IR scan were used to generate a downhole temperature profile at Hole 1247B (Fig. F22). The temperatures in the upper 20 mbsf are ~2°–3°C colder than those in the deeper part of the hole, but no discrete temperature anomalies were detected over this depth (Fig. F23). There was no indication of mousselike texture within the first three cores (see "Lithostratigraphy," p. 2), and the LWD resistivity data, converted to pore water saturation (S_w) using Archie's Relation, did not predict the presence of any hydrate in the upper 20 mbsf either (see "Downhole Logging," p. 19). The low temperatures observed may, therefore, be the result of a shorter core-handling time on the rig floor before the IR scan and/or seawater contact.

Significant ΔT anomalies start to occur at a depth of 45 mbsf (Fig. F23). The anomalies cluster in two intervals, from 45 to 65 mbsf and from 80 to 120 mbsf. The BSR depth at Site 1247 is between 121 and 124 mbsf, which matches well with the last thermal anomaly at 118 mbsf (Table T10). There is an apparent mismatch between the S_w data and the specific depths of ΔT anomalies, suggesting lateral heterogeneitiy in the presence of hydrate at this site. Note that the distance between Hole 1247A, where LWD data were obtained, and Hole 1247B, where cores were collected, is 87 m. Overall, $1 - S_w$ is relatively small with values below 0.2, indicating only small concentrations of hydrate present in the sediments, which is consistent with relatively small ΔTs from the IR imaging.

Hydrate samples were taken at 93 and 113 mbsf at Site 1247 after their identification by IR imaging. The temperature anomaly associated with interval 204-1247B-14H-5, 39–62 cm, was –2.8°C. However, close inspection of the sample after it had been preserved in liquid nitrogen did not show any visible hydrate crystals. Instead, the sediment texture suggested that disseminated gas hydrate had been present in this sample but was largely dissociated prior to storage in liquid nitrogen. Alternatively, the thermal anomaly could result from gas expansion or gas exsolution. Pore water chlorinities (Fig. F23) (see "Interstitial Water Geochemistry," p. 9) are consistent with the presence of a few volume percent of hydrate at this depth, favoring the hypothesis that hydrate was present at 93–113 mbsf in Hole 1247B.

Sediment Density from Multisensor Track and Moisture and Density

Sediment density increases with depth from values of ~1.6 g/cm³ at the seafloor to 1.8 g/cm³ at 220 mbsf (the bottom of Hole 1247B) (Fig. F24; Table T11). Generally, bulk density remains almost constant in the lower 50–60 m of Holes 1247A and 1247B at ~1.8 g/cm³.

There are several events in the density profile that can be correlated to lithostratigraphic units and seismic horizons (Figs. F24, F25). The bottom of lithostratigraphic Unit II at 60 mbsf is correlated with seismic Horizon Y. The results from moisture and density (MAD) samples indicate a zone of high variability within ~25 m above this unconformity. Individual bulk density values are higher by ~0.2 g/cm³ within this interval from 40 to 65 mbsf. The porosity of those samples is <50% compared to a background average of 55%–60%, and grain density is relatively higher. The scattering of bulk density values is the result of discrete sampling of individual sandy layers and the background clay-rich sediments. High sediment densities are not measured in the

F22. Downhole temperature profile, p. 50.

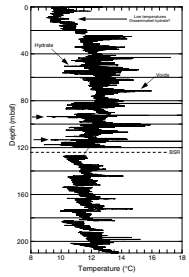

F23. Comparison of temperature anomalies in the IR profile and S_w, p. 51.

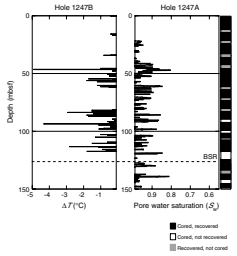

T10. IR anomalies, p. 79.

F24. Physical properties, p. 52.

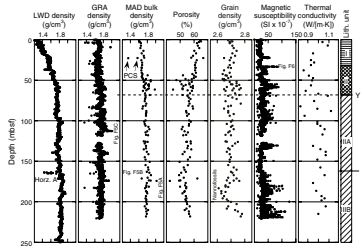

T11. MAD data, p. 80.

F25. Comparison of physical properties and IR temperature anomalies with 3-D seismic data, p. 53.

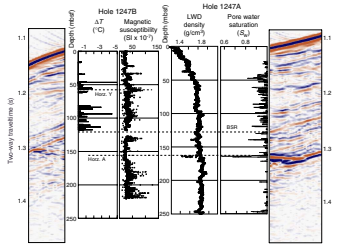

gamma ray attenuation (GRA) density data, probably as a result of the averaging effect of the GRA measurement.

A similar observation can be made at a depth of 181 mbsf (Sample 204-1247B-23X-1, 108–110 cm) (Fig. F26A). The sample was taken in the sand layers, resulting in a high density of 2.019 g/cm³ and a low porosity of 43%. It is interesting to note that the GRA density over this interval is also increased. A sample taken a few meters above (Sample 204-1247B-22X-6, 27–29 cm [171 mbsf]) was taken from a highly disturbed interval with apparent high porosity and low bulk density of 1.67 g/cm³ (Fig F26B). These samples are not representative of the general background trend and should be used with caution.

The GRA density data at a depth of 112 mbsf show elevated values that are not evident in the MAD or LWD density data. This interval corresponds to Section 204-1247B-14H-5 (Fig. F26C). Sample 204-1247B-14H-5, 30–32 cm, has a lower bulk density (1.81 g/cm³) than the two samples taken above. This core section shows higher sulfide content and a structure that probably reflects bioturbation.

Horizon A was cored at Site 1247 at a depth of 163 mbsf. There is a prominent decrease in the LWD density data, but this decrease is not so evident in the GRA and bulk density data. At Site 1247, Horizon A is not glass rich and does not contain ash layers, in contrast to its nature at other Leg 204 sites.

Below Horizon A, at a depth of 164 mbsf, the grain density shows a decrease to values of ~2.6 g/cm³. This decrease is consistent with the onset of lithostratigraphic Subunit IIIB, which is characterized by a high percentage of calcareous nannofossils (see "Lithostratigraphic Subunit IIIB," p. 6, in "Lithostratigraphic Unit III" in "Lithostratigraphic Units" in "Lithostratigraphy").

F26. Relation of bulk density to sedimentologic structure of sediment, p. 54.

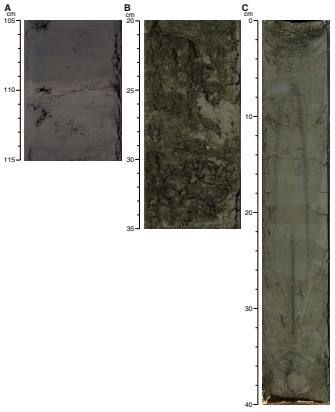

Magnetic Susceptibility

The MS record is characterized by a series of individual spikes that can be correlated to the presence of sulfides and turbidites (Fig. F24). However, it is difficult to relate individual features in the MS data to the exact location of the turbidites in the subdecimeter range of the core description. The uncertainties that remain are related to relative shifts of sediments and voids in the core liner during the core-splitting procedure and at section boundaries where whole-round samples were taken on the catwalk.

The boundary between lithostratigraphic Unit II and Subunit IIIA is marked by a MS peak at a depth of 60 mbsf. MS is generally increased in the last 2 m of Core 204-1247B-8H and shows detailed variations that are related to turbidite sequences.

Another remarkable feature of the MS record is the presence of a sulfide vein at 55 mbsf that contained abundant concretions (Fig. F27). The concretions are rich in pyrrhotite as inferred from XRD analyses.

F27. Sulfide vein and MS profile, p. 55.

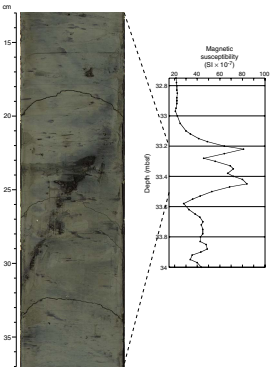

Compressional Wave Velocity from the Multisensor Track and Hamilton-Frame

At this site, no compressional (*P*)-wave velocities (V_P) could be measured with the MST as a result of intensive gas expansion cracks. An equipment failure on the Hamilton Frame, also precluded V_P measurements on the split cores.

Thermal Conductivity

Thermal conductivity was measured following standard procedures (see "Physical Properties," p. 22, in the "Explanatory Notes" chapter). Values are scattered and vary between a minimum of 0.83 W/(m·K) and a maximum of 1.112 W/(m·K) (Table T12). The average thermal conductivity is 0.99 W/(m·K). There is no obvious correlation between thermal conductivity and other physical properties, especially bulk density.

T12. Thermal conductivity, p. 81.

Shear Strength

As a result of pervasive gas-expansion cracks, no shear strength measurements were carried out at this site.

Summary and Discussion

Physical properties measured in Hole 1247B match well with the defined lithostratigraphic units. The boundaries are associated with peaks in MS (e.g., the boundary between Units II and III) or correlate to changes in sediment and grain density. Horizon A was cored at this site at a depth of 163 mbsf but did not contain high amounts of ash and does not show any significant change in bulk density. This is in contrast to the LWD data, which show a prominent drop in LWD density across this horizon in Hole 1247B.

IR thermal imaging provided the on-catwalk identification of gas hydrates, and at this site, two hydrate samples were taken based on negative temperature anomalies.

DOWNHOLE TOOLS AND PRESSURE CORING

Downhole Temperature Measurements

Six in situ temperature runs were made at this site using the APCT tool, including a dedicated mudline run; two DVTP runs were also made (Table T13; Fig. F28). APCT data were modeled using the software TFIT (as described in "Downhole Tools and Pressure Coring," p. 34, in the "Explanatory Notes" chapter) using measured thermal conductivities (see "Physical Properties," p. 14). Uncertainty in the extrapolated value of in situ temperature resulting from a subjective analyst picking of t_p, t_i, and t_f is <0.02°C for these high-quality records. Uncertainty resulting from possible errors in measured values of thermal conductivity is estimated to also be ~0.02°C.

T13. Temperature measurements, p. 82.

F28. Raw data for estimating in situ temperatures, p. 56.

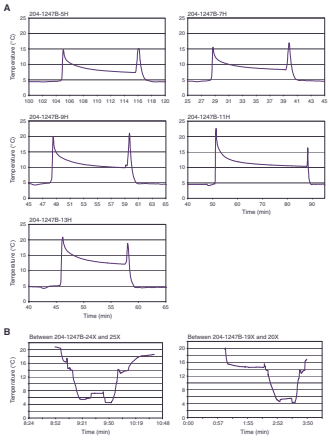

Both of the DVTP runs yielded apparent temperatures that are not consistent with the APCT data, and the time series suggest that the probe did not penetrate the sediment properly. These data were not used for the determination of the in situ thermal gradient.

The resulting temperature estimates are shown in Figure F29. The six APCT measurements define a straight line very well, and there is no significant difference in the slope and seafloor intercept if the mudline measurement is excluded. The temperature gradient of ~0.053°C/m results in a predicted depth to the base of the GHSZ of 151–152 mbsf, considerably deeper than the BSR depth of 129–134 mbsf determined from acoustic logging data and VSP measurements. If we add 0.513°C to each measurement, as suggested by the calibration for APCT 11 in an ice-water bath (see "Downhole Tools and Pressure Coring," p. 14, in

F29. Subsurface temperatures plotted vs. depth, p. 57.

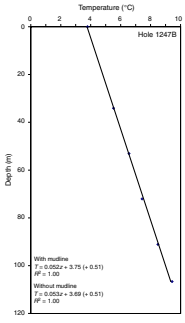

the "Site 1246" chapter), the predicted depth to the base of the methane stability zone is 142 mbsf, accounting for half of the apparent mismatch. This is equivalent to the temperature at the BSR being ~0.6°–1.2°C colder than predicted by the methane/seawater stability curve.

In Situ Pressure Measurements

No in situ pressure measurements were made at this site.

Pressure Core Sampler

The ODP PCS was deployed three times at Site 1247. Two of these deployments were successful (i.e., a core under pressure was recovered). The ball valve did not fully close during the other deployment. The main objectives of the deployments were (1) to construct a detailed profile of concentration and composition of natural gases in the upper part of the section (0–125 mbsf) and (2) to identify the presence/absence and concentration of gas hydrate within the GHSZ.

Specific depth intervals were targeted for deployment of the PCS. One core (Core 204-1247B-4P [22.6–23.6 mbsf]) was recovered in shallow sediments, and one core (Core 16P [123.3–124.3 mbsf]) was recovered from above the BSR at ~129 mbsf.

The PCS chambers were degassed for times from 547 to 3454 min after recovery on board (Table **T14**). Pressure was recorded during degassing experiments (Fig. **F30**). Gas was collected in a series of sample increments (splits), and most were analyzed for molecular composition (see **"Organic Geochemistry,"** p. 12). In addition, gas splits were subsampled for onshore analyses. After degassing, the PCS chambers were disassembled. The lengths of the cores were measured (Table **T14**), and samples were taken for analysis of physical properties (see **"Physical Properties,"** p. 14).

Gas was collected in 15- to 550-mL increments. The measured incremental and cumulative volumes are plotted vs. time (Fig. **F30**). The cumulative volume of released gas varies from 195 (Core 204-1247-4P) to 6025 mL (Core 16P) (Table **T14**). No gas was released during the last openings in both degassing experiments, suggesting that all gas present in the cores was collected.

Gases released from the PCS are mixtures of air (N_2 and O_2), CH_4, CO_2, and C_{2+} hydrocarbon gases (see **"Gas Hydrate and Pressure Cores,"** p. 13, in "Organic Geochemistry"). The abundance of air components in the PCS gas samples (5.6%–52.9% of gas mixtures) suggests that air was not properly displaced from the PCS by seawater during deployments. Methane is the dominant natural gas present in collected gas splits. The molecular composition of gases from the PCS is similar to the composition of gas voids at adjacent depths (Fig. **F19**).

Sediments in cores recovered with the PCS have lithologies that are similar to sediments recovered with the APC at adjacent depths (see **"Physical Properties,"** p. 14). Porosity values measured on samples from APC cores taken near the PCS were used to estimate the methane concentration in situ (Table **T14**).

The concentration of methane in situ was estimated based on data from the degassing experiment (i.e., total volume of methane) and core examination (i.e., length of recovered core and the porosity of sediments). The calculation yields equivalent concentrations varying from 4.3 to 292.4 mM of methane in pore water. These concentrations have been compared with the theoretical methane-solubility curve extrapo-

T14. Results from degassing experiments, p. 83.

F30. Volume-pressure-time plots for PCS, p. 58.

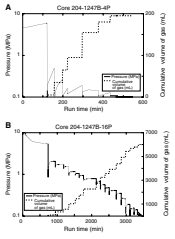

lated from values calculated for higher pressures (depths) (Handa, 1990; Duan et al., 1992) and are illustrated in Figure F31.

Preliminary analysis of gas concentrations suggests that gas hydrate may have been present in small concentrations (perhaps <3% of pore volume) in Core 204-1247B-16P, although no evidence of the presence of gas hydrate was found in the pressure record of core degassing (Fig. F30). Methane concentration measured in shallow Core 204-1247B-4P is consistent with the trend of concentrations that can be extrapolated based on the headspace measurements. This confirms that the PCS can be successfully used to study methane generation and flux in shallow sediments. Additional comparison of measured methane concentrations with theoretical methane solubility above and below the BSR will be performed on shore to better estimate if methane was present in situ in solution, in free phase, or as gas hydrate.

F31. Methane concentrations, p. 59.

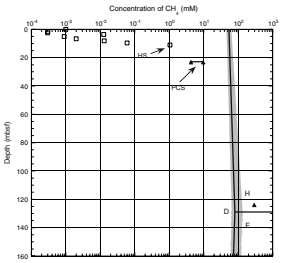

HYACINTH Pressure Cores

No HYACINTH pressure cores were taken at this site.

DOWNHOLE LOGGING

Logging While Drilling

Operations

LWD operations at Site 1247 began at 0430 hr Universal Time Coordinated (UTC) on 20 July 2002, with tool initialization at the rig floor. LWD tools included the Geo Vision Resistivity (GVR) RAB with $9^1/_8$-in button sleeve, MWD, the NMR-MRP tool, and the VND. Batteries had sufficient remaining life and were not changed. Hole 1247A was spudded at 0715 hr at 845.00 meters below rig floor (mbrf) water depth (drillers depth) on the northwestern crest of Southern Hydrate Ridge. Drilling proceeded at ~25 m/hr to TD at 270 mbsf at 2130 hr on 20 July. Heave conditions had increased since the LWD operations at Site 1246, and the real-time data record was changed to increase the time resolution of weight-on-bit and torque measurements for heave analysis. LWD tools were pulled to ~60 m clear of the seafloor at 2315 hr on 20 July for the dynamic positioning move to Site 1248. Total bit run was ~18 hr.

F32. LWD logs, p. 60

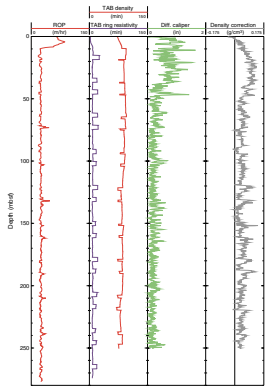

Logging Quality

Figure F32 shows the quality control logs for Hole 1247A. The target ROP of 25 m/hr (±5 m/hr) in the interval from the seafloor to TD was generally achieved. This was sufficient to record one sample per 4-cm interval (~25 samples per meter), which was obtained over 96% of the total section of the hole. The quality of RAB images is thus quite high, and no significant resolution loss is observed with variation in ROP in Hole 1247A. However, the quality of the RAB images in the upper 15 mbsf of Hole 1247A (Fig. F33) is degraded by an apparent problem associated with low rates of bit rotation. The NRM-MRP porosity data were enhanced by using a slow drilling rate, with a data sampling resolution of approximately one sample per 15-cm interval.

The differential caliper log (DCAL), which gives the distance between the tool sensor and the wall of the borehole, as recorded by the LWD

F33. LWD data, p. 61.

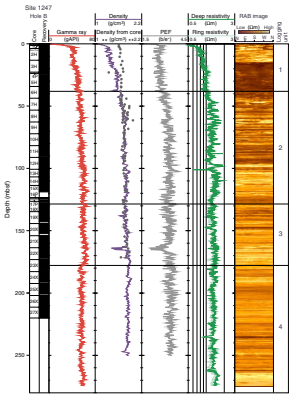

density tool, is the best indicator of borehole conditions. The DCAL values are <1 in over 96% of the total sections in Hole 1247A. Only the uppermost 47 mbsf of the hole contains washouts >1 in. The density correction, calculated from the difference between the short- and long-spaced density measurements, varies from 0 to 0.13 g/cm³ (Fig. F32), which generally suggests good-quality density measurements. A standoff of <1 in between the tool and the borehole wall also indicates high-quality density measurements, with an accuracy of ±0.015 g/cm³.

Time-after-bit (TAB) measurements are 12 ± 2 min for ring resistivity and gamma ray logs and 87 ± 5 min for density and neutron porosity logs (Fig. F32). TAB values remain relatively constant over the interval, coinciding with the steady ROP while drilling over most of the hole.

The depths relative to seafloor for all of the LWD logs were fixed by identifying the gamma ray signal associated with the seafloor and shifting the log data to the appropriate depth, as determined by the drillers pipe tallies. For Hole 1247A, it was determined that the gamma ray log pick for the seafloor was at a depth of 847 mbrf. The rig floor logging datum was located 10.9 m above sea level for this hole.

Wireline Logging

Operations

Hole 1247B was APC and XCB cored to a depth of 220 mbsf (drillers depth). Rig-up for conventional wireline logging (CWL) operations began at 0035 hr on 24 August, and final rig-down was completed by 1215 hr on 24 August. See Table T15 for detailed information on the Hole 1247B CWL program.

T15. CWL operations summary, p. 84.

CWL operations in Hole 1247B began with the deployment of the triple combo tool string (Temperature/Acceleration/Pressure [TAP] tool/Dual Induction Tool [DIT]/Hostile Environment Litho-Density Tool [HLDT]/Accelerator Porosity Sonde [APS]/Hostile Environment Gamma Ray Sonde [HNGS]/Inline Checkshot Tool [QSST]) (Table T15). The triple combo tool string initially reached the TD of the hole (220 mbsf) without difficulty and with no sticking problems. Excellent-quality data were acquired during the main uphole pass (see below), and the tool was run back to the bottom of the hole (BOH) for a second log pass. The second pass also reached a TD of 220 mbsf, and excellent-quality data were recorded on the second ascent. TAP tool temperature data and associated depth data were recorded without problems during both lowerings of the triple combo tool string. After completing the second pass, the triple combo tool string was again lowered to a depth of 220 mbsf to obtain several checkshots with the QSST. A one-way traveltime of 678.5 ms was recorded at the TD of Hole 1247B (220 mbsf). To calculate a checkshot interval velocity with depth, a 32-m uphole shift is necessary to take into account the positioning of the QSST at the top of the triple combo tool string. The triple combo logging run ended with the rig-down of the tool string being completed at 0715 hr on 24 August.

For the second CWL run in Hole 1247B, the FMS-sonic tool string (FMS/Dipole Sonic Imager [DSI]/Scintillation Gamma Ray Tool [SGT]) was deployed. The FMS-sonic tool string reached a maximum depth of 220 mbsf on two consecutive passes. The two FMS-sonic runs confirmed the excellent condition of the hole, as observed during the triple combo logging run. The FMS images and sonic waveforms recorded from the two lowerings of the FMS-sonic tool string were of very high quality. During the first pass of the FMS-sonic tool string, the DSI was

set at a low-frequency mode for the lower dipole, standard frequency for the upper dipole and low frequency for the monopole. During the second pass of the DSI, the monopole and the lower dipole were set at their standard frequencies, and the upper dipole was set at a low frequency. The recorded sonic waveforms from both lowerings of the DSI are of very high quality, particularly the dipole recordings, but the very low velocity of this formation made it difficult for the automatic slowness/time coherence (STC) picking program to select accurate compressional velocities. Some adjustment of the STC parameters allowed for improved V_P picks, but further reprocessing is required. The quality of the recorded shear wave data was very high, but it will also require additional processing.

A final run was made for seismic experiments which will be discussed elsewhere.

Logging Quality

All logging data from the triple combo and FMS-sonic runs in Hole 1247B are of very high quality (Figs. **F34, F35, F36, F37**). The hole conditions were excellent, with an almost straight HLDT caliper measurement from 11.8 to 12.5 in on average. Comparison of logs from successive passes shows good repeatability of the data. The two passes of the FMS calipers also showed that the hole was nearly cylindrical, consistent with the HLDT log caliper recorded on the triple combo runs.

The absolute depths, relative to seafloor, for all of the CWL logs were fixed by identifying the gamma ray signal associated with the seafloor and depth shifting the logging data appropriately. The gamma ray pick for the seafloor in Hole 1247B was 846 mbrf for all of the CWL runs.

Interpretation of Logging-While-Drilling and Wireline Logging

Data from Holes 1247A and 1247B show excellent quality LWD and CWL logs. Low ROPs and reduced pump rates during LWD operations in Hole 1247A greatly reduced the effect of borehole washouts observed at other sites drilled earlier during Leg 204. No sliding tests were conducted to evaluate downhole LWD tool motion at this site. The downhole LWD and CWL logs reveal in situ gas hydrate as high-resistivity zones and RAB image anomalies. The high-resistivity nature of the gas hydrate–bearing interval in Hole 1247A allowed quantitative estimates of gas hydrate saturations. Resistivity and density log variations below the GHSZ (~128 mbsf) appear to indicate lithologic changes and the possible presence of free gas. Borehole breakouts, which result from subsurface horizontal stress differences, are observed in the lower portion of the hole. NRM-MRP logs were also reprocessed to compute bound fluid volume and total free fluid porosities.

Logging-While-Drilling and Wireline Logging Comparison

Figure **F36** shows a comparison of downhole LWD and CWL data from Holes 1247A and 1247B, using the gamma ray, neutron porosity, density, photoelectric factor, and deep resistivity logs. The highly variable CWL log data within the upper 78 mbsf of Hole 1247B was obtained through the drill pipe. Comparison of similar log signatures on

F34. CWL data, p. 62.

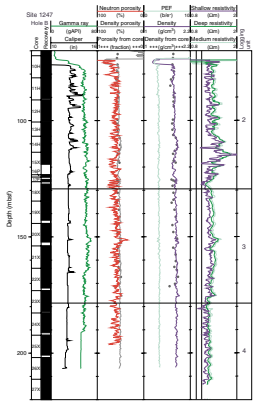

F35. CWL gamma ray logging data, p. 63

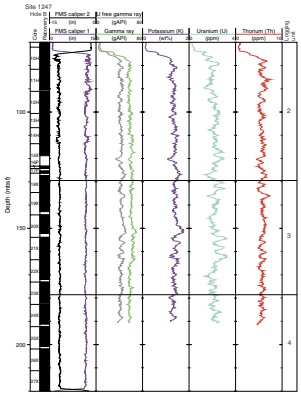

F36. LWD and CWL downhole logging data, p. 64.

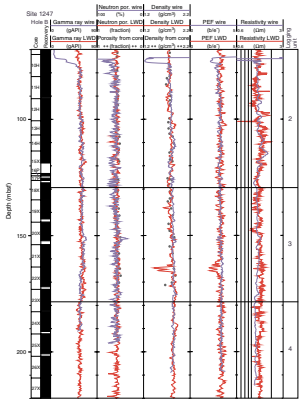

Figure F36 reveals that the CWL logging data from Hole 1247B matches the LWD logging data from Hole 1247A. The LWD and CWL data from each hole exhibit similar curve shapes and absolute log values. The CWL (Hole 1247B) and LWD (Hole 1247A) resistivity logs, however, exhibit differences in measured values with depth and a difference in the apparent vertical resolution of each device, with the RAB LWD tool yielding a log with a higher vertical resolution.

Logging Units

The logged section in Holes 1247A and 1247B is divided into four "logging units" on the basis of obvious changes in the LWD and CWL gamma ray, density, electrical resistivity (Figs. F33, F34, F35), and acoustic velocity (Fig. F37).

Logging Unit 1 (0–37 mbsf) is characterized by increasing gamma ray values, resistivity, and density with depth as measured by the LWD tools. However, this trend in the downhole logging data is probably due in part to degraded logging measurements within the enlarged portion of the near-surface borehole as shown in Figure F32. The base of logging Unit 1 does not exactly coincide with the base of lithostratigraphic Unit I (0–27 mbsf), which is composed of silty clay sediments. The transition from logging Unit 1 to 2 is defined by a sharp increase in LWD-derived density (from ~1.55 to ~1.70 g/cm³) and a relatively subtle increase in resistivity (from ~1.0 to ~1.1 Ωm).

Logging Unit 2 (37–128 mbsf) is characterized by zones of distinct high resistivities and high acoustic velocities, with measured peak resistivity values >1.8 Ωm and V_P > 1.70 km/s. The gamma ray log in this unit shows a characteristic cyclicity of values that may reflect the interbedded sand and clay turbidite sequences as described by the shipboard sedimentologists for lithostratigraphic Units II and III (27–220.62 mbsf) (see "Lithostratigraphic Units," p. 3, in "Lithostratigraphy"). The downhole logging–measured density increases with depth in logging Unit 2 (from 1.6 at the top to near 1.9 g/cm³ at the bottom). In Hole 1247B (Fig. F37), the acoustic transit-time log has been used to precisely select the depth of the boundary between logging Units 2 and 3, which is marked by an abrupt drop in V_P to <1.53 km/s. Also noted on the density log is a subtle drop in density at the contact between logging Unit 2 and 3 (of ~0.1 g/cm³), which corresponds to the estimated depth of the BSR at this site.

Logging Unit 3 (128–178 mbsf) correlates with the lower part of lithostratigraphic Unit III (60–220.65 mbsf), which is described as a diatom- and foraminifer-bearing silty clay turbidite sequence. Logging Unit 3 is generally characterized by lower and more uniform resistivities compared to Unit 2. The transition from logging Unit 3 to 4 is marked by an abrupt drop in gamma ray values (from ~65 to 55 American Petroleum Institute gamma ray units [gAPI]) and a more subtle drop in density (Fig. F33), which appears to mark the contact with the deformed sediments of the accretionary complex. A 2-m-thick anomalous interval, characterized by variable V_P (ranging from 1.51 to 1.54 km/s), variable resistivity (ranging from ~1.1 to ~1.9 Ωm), and low density (<1.45 g/cm³) is present in logging Unit 3, within the depth interval from 163 to 165 mbsf, which collectively suggests the presence of a free gas–bearing sand. This apparent free gas–bearing interval corresponds to seismic Horizon A (see "Introduction," p. 1).

F37. CWL acoustic logging data, p. 65.

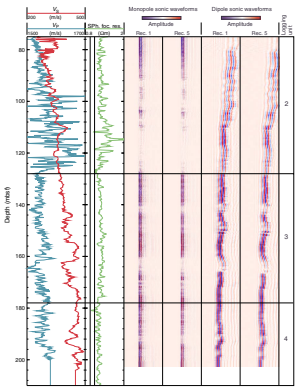

Logging Unit 4 (178–270 mbsf; TD of Hole 1247A), reflecting the upper portion of the deformed sediments of the accretionary complex, is characterized by almost constant gamma ray and density log measurements with depth that are not consistent with a normal compaction profile.

Resistivity-at-the-Bit and Formation MicroScanner Images

Both the RAB and FMS tools produce high-resolution images of the electrical resistivity of the borehole wall that can be used for detailed sedimentological and structural interpretations. The RAB and the FMS tools can also be used to make high-resolution images of gas hydrates in the borehole, thus yielding information about the nature and texture of gas hydrate in sediments. The resolution of the images from the RAB tool is considerably lower than the resolution of the images from the FMS. The RAB images have about a 5- to 10-cm vertical resolution, whereas the FMS tool can resolve features such as microfractures with widths <1 cm. However, the RAB tool provides 360° coverage of the borehole, whereas FMS images cover only ~30% of the hole.

In Figure **F38,** we have cross correlated a RAB image (Hole 1247A) and an FMS image (Hole 1247B) from the stratigraphic interval that contains Horizon A, which has been identified as a prominent regional seismic reflector (see **"Introduction,"** p. 1). As shown on the FMS and RAB images in Figure **F38,** Horizon A appears as a complex interbedded zone of high and low resistivities. More detailed examination of the FMS image shows distinct lateral variability within this interval and apparent fine-scale sedimentologic structures. The comparison of the deep- and shallow-measuring RAB images in Figure **F38** also shows evidence of geologic controls on the infiltration of conductive drilling fluids into the formation, which appears more prevalent in the shallow measuring RAB image.

F38. RAB image showing Horizon A, p. 66.

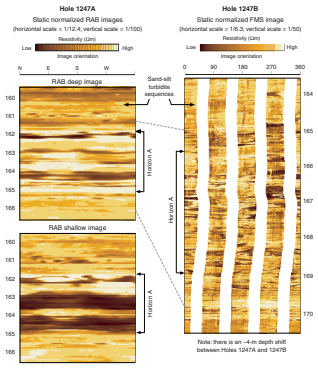

Logging Porosity

Sediment porosity can be determined from analyses of recovered cores and from numerous borehole measurements (see **"Physical Properties,"** p. 22, and **"Downhole Logging,"** p. 43, both in the "Explanatory Notes" chapter). Data from the LWD density, neutron, and NMR-MRP logs have been used to calculate sediment porosities for Hole 1247A. Core-derived physical property data, including porosities (see **"Physical Properties,"** p. 14), have been used to both calibrate and evaluate the log-derived sediment porosities.

The VND LWD log-derived measurements of density in Hole 1247A (Fig. **F33**) are relatively consistent within logging Units 2 and 3, with values ranging from ~1.6 near the top of Unit 2 (37 mbsf) to >1.8 g/cm^3 at the bottom of Unit 4 at 250 mbsf. The density log measurements are degraded in logging Unit 1 as discussed earlier in this chapter. The LWD log-derived density measurements from Hole 1247A were used to calculate sediment porosities (ϕ) using the standard density-porosity relation,

$$\phi = (\rho_m - \rho_b)/(\rho_m - \rho_w).$$

Water density (ρ_w) was assumed to be constant and equal to 1.05 g/cm^3; however, variable core-derived grain/matrix densities (ρ_m) were as-

sumed for each logging density-porosity calculation. The core-derived grain densities (ρ_m) in Hole 1247B ranged from an average value at the seafloor of 2.70 to ~2.73 g/cm³ at the BOH (see **"Physical Properties,"** p. 14). The density log-derived porosities in logging Units 2 through 4 (37–270 mbsf) of Hole 1247A range from ~46% to 62% (Fig. **F39**). However, the density log porosities in logging Unit 1 (0–37 mbsf) are more variable, ranging from 67% to 88%, which is in part controlled by poor borehole conditions.

The LWD neutron-porosity log from Hole 1247A (Fig. **F39**) yielded sediment porosities ranging from an average value at the top of the logged section of ~68% to ~55% in logging Unit 4. The "total" sediment porosity derived by the NMR-MRP tool in Hole 1247A (Fig. **F39**) ranged from ~80% near the seafloor to ~45% near the bottom of the hole.

In studies of downhole logging data it is common to combine and compare porosity data from different sources to evaluate results and assess the accuracy of a particular measurement. The comparison of core-derived and LWD log-derived porosities in Figure **F39** reveals that the density and NMR-MRP-derived porosities are generally similar to the core porosities in most of logging Units 2 and 3 (37–178 mbsf). However, the density and NMR-MRP log-derived porosities are generally higher than the core-derived porosities in logging Unit 1 and the upper portion of logging Unit 2, which can be attributed to downhole logging data that have been degraded by enlarged borehole conditions. The neutron porosities are generally higher than the core-derived porosities throughout most of the hole.

F39. LWD- and core-derived porosities, p. 67.

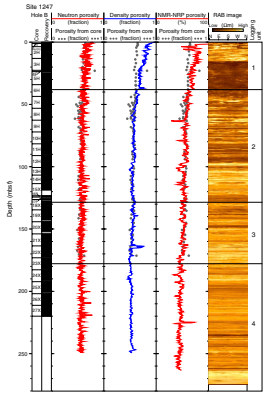

Gas Hydrate

The presence of gas hydrate at Site 1247 was documented by direct sampling, with one specimen of gas hydrate recovered in Hole 1247B at a depth of 93.01 mbsf and a significant IR anomaly perhaps related to gas hydrate observed at 113.09 mbsf. Despite this limited occurrence of gas hydrates, it was inferred, based on geochemical core analyses (see **"Interstitial Water Geochemistry,"** p. 9), IR analysis of cores (see **"Physical Properties,"** p. 14), and downhole logging data, that disseminated gas hydrate is present in logging Unit 2. As previously discussed in **"Downhole Logging,"** p. 43, in the "Explanatory Notes" chapter, the presence of gas hydrate is generally characterized by increases in logging-measured electrical resistivities and acoustic velocities. Logging Unit 2 at Site 1247 is characterized by a distinct stepwise increase in both electrical resistivities and acoustic velocities. In addition, the LWD resistivity tool revealed several thin high-resistivity zones within logging Unit 1 (0–37 mbsf), which suggests the possible presence of gas hydrate.

LWD resistivity log data have been used to quantify the amount of gas hydrate at Site 1247. For the purpose of discussion, it is assumed that the high resistivity measured in logging Unit 2 is a result of the presence of gas hydrate. Archie's Relation,

$$S_w = (aR_w/\phi^m R_t)^{1/n}$$

(see **"Downhole Logging,"** p. 43, in the "Explanatory Notes" chapter), was used with resistivity data (R_t) from the LWD RAB tool and porosity data (ϕ^m) from the LWD density tool to calculate water saturations in Hole 1247A. It should be noted that gas hydrate saturation (S_h) is the

measurement of the percentage of pore space in sediment occupied by gas hydrate, which is the mathematical complement of Archie-derived S_w, with

$$S_h = 1 - S_w.$$

For Archie's Relation, the formation water resistivity (R_w) was calculated from recovered core-water samples and the Archie a and m variables were calculated using a crossplot technique which compares the downhole logging–derived resistivities and density porosities. See Collett and Ladd (2000) for the details on how to calculate the required formation water resistivities and Archie variables. The values used for Site 1247 were a = 1, m = 2.8, and n = 1.9386.

Archie's Relation yielded water saturations (Fig. **F40**) ranging from an average minimum value as low as of ~85% to a maximum of 100% in logging Unit 2 (37–128 mbsf) of Hole 1247A, which implies the gas hydrate saturations in logging Unit 2 range from 0% to 15%. Figure **F40** also reveals that logging Unit 1 may contain a small amount of gas hydrate. However, the low water saturations shown in logging Unit 3 (Fig. **F40**) may indicate the presence of free gas–bearing sediments (as discussed previously in this chapter).

Temperature Data

The TAP tool was deployed on the triple combo tool string in Hole 1247B (Fig. **F41**). During the process of coring and drilling, cold seawater is circulated in the hole, cooling the formation surrounding the borehole. Once drilling ceases, the temperature of the fluids in the borehole gradually rebounds to the in situ equilibrium formation temperatures. Thus, the temperature data from the TAP tool cannot be easily used to assess the nature of the in situ equilibrium temperatures. However, the plot of the first pass downgoing temperature profile in Figure **F41** reveals several gradient changes that were caused by borehole temperature anomalies. The temperature anomaly at ~90 mbsf is the base of the drill pipe during the initial descent of the triple combo tool string. The break in the slope of the first pass downgoing temperature log at a depth of ~140 mbsf is near the depth of the BSR (128 mbsf) at this site.

F40. LWD-derived water saturations, p. 68.

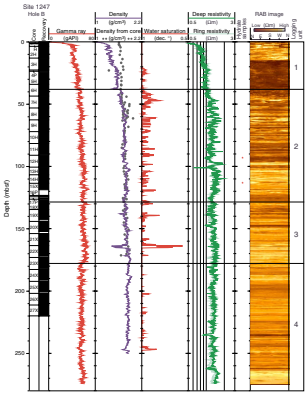

F41. Borehole temperatures, p. 69.

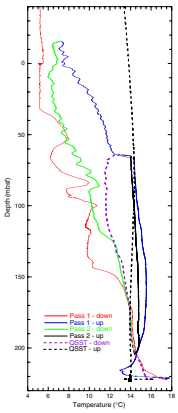

REFERENCES

Borowski, W.S., Paull, C.K., and Ussler, W., III, 1996. Marine pore-water sulfate profiles indicate in situ methane flux from underlying gas hydrate. *Geology,* 24:655–658.

Clague, D., Maher, N., and Paull, C.K., 2001. High-resolution multibeam survey of Hydrate Ridge, offshore Oregon. *In* Paul, C.K., and Dillon, W.P. (Eds.), *Natural Gas Hydrates: Occurrence, Distribution, and Detection.* Am. Geophys. Union, Geophys. Monogr. Ser., 124:297–306.

Collett, T.S., and Ladd, J., 2000. Detection of gas hydrate with downhole logs and assessment of gas hydrate concentrations (saturations) and gas volumes on the Blake Ridge with electrical resistivity log data. *In* Paull, C.K., Matsumoto, R., Wallace, P.J., and Dillon, W.P. (Eds.), *Proc. ODP, Sci. Results,* 164: College Station, TX (Ocean Drilling Program), 179–191.

Duan, Z., Møller, N., Greenberg, J., and Weare, J.H., 1992. The prediction of methane solubility in natural waters to high ionic strengths from 0° to 250°C and from 0 to 1600 bar. *Geochim. Cosmochim. Acta,* 56:1451–1460.

Edmond, J.M., Measures, C., McDuff, R.E., Chan, L.H., Collier, R., and Grant, B., 1979. Ridge crest hydrothermal activity and the balances of the major and minor elements in the ocean: the Galapagos data. *Earth Planet. Sci. Lett.,* 46:1–18.

Handa, Y.P., 1990. Effect of hydrostatic pressure and salinity on the stability of gas hydrates. *J. Phys. Chem.,* 94:2652–2657.

Seyfried, W.E., Jr., Janecky, D.R., and Mottl, M.J., 1984. Alteration of the oceanic crust: implications for geochemical cycles of lithium and boron. *Geochim. Cosmochim. Acta,* 48:557–569.

Figure F1. Bathymetric map showing locations of holes drilled at Site 1247. Bathymetry from EM300 data acquired by Monterey Bay Aquarium Research Institute (MBARI) (Clague et al., 2001).

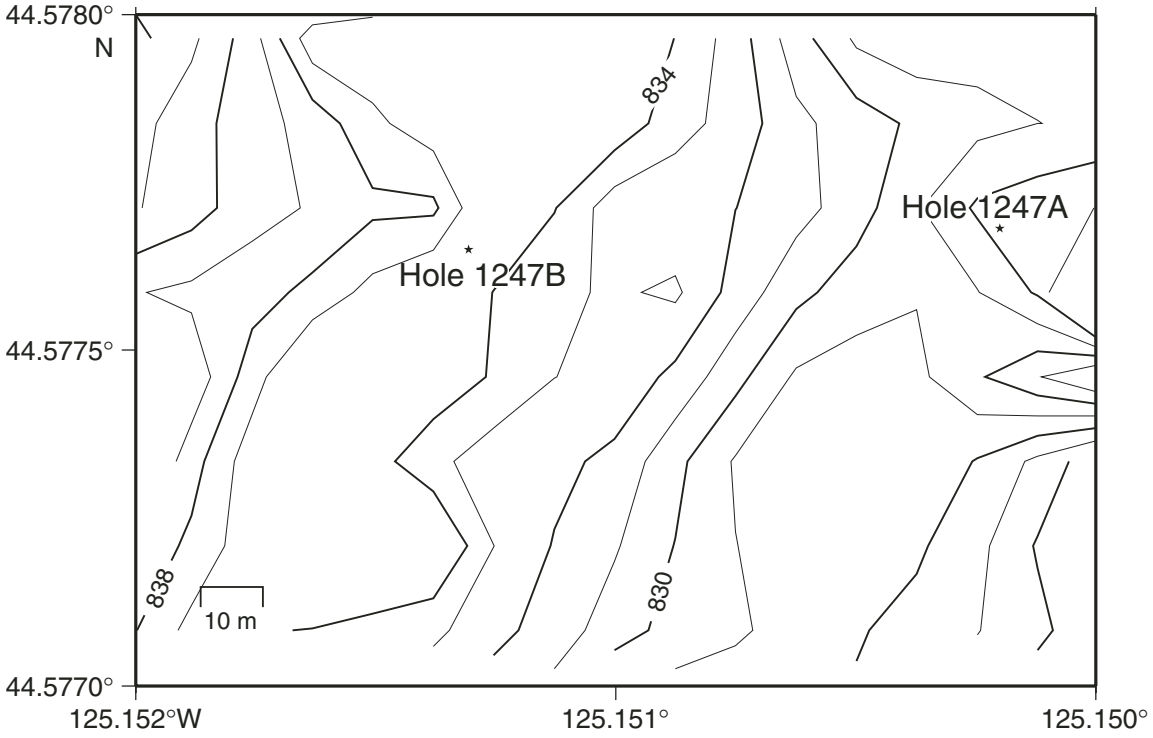

Figure F2. Detail of seismic data at Site 1247 showing the change in the seismic characteristics of Horizon A between Holes 1247A and 1247B. BSR = bottom-simulating reflector.

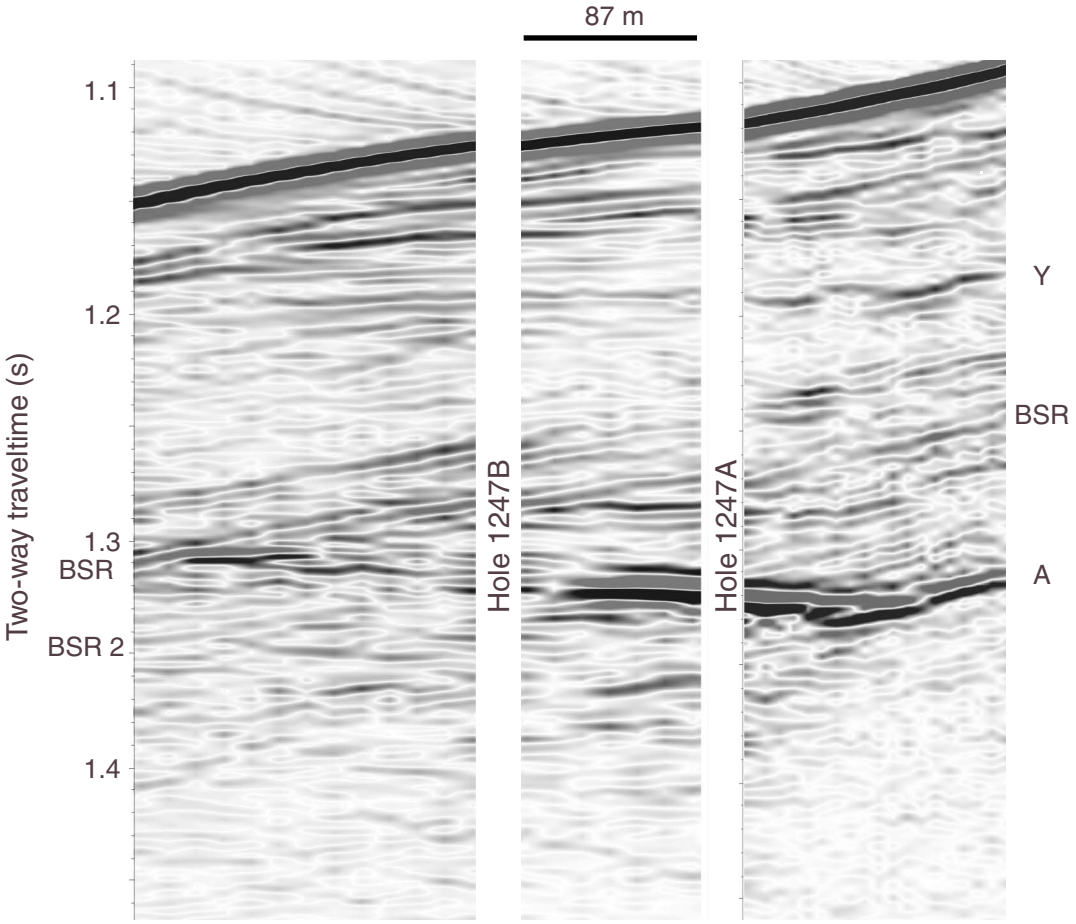

Figure F3. Lithostratigraphic summary for Site 1247. (Continued on next page.)

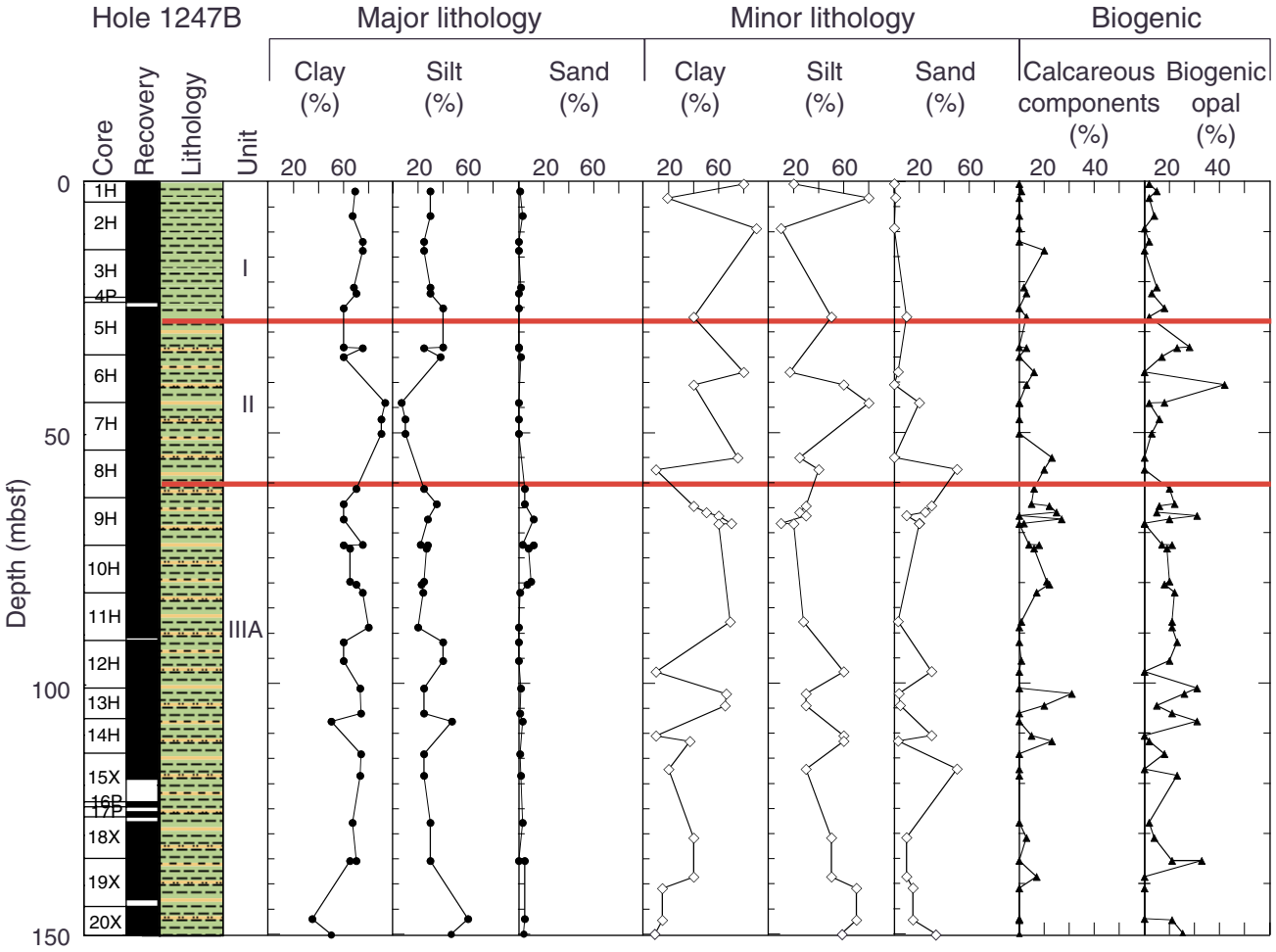

Figure F3 (continued).

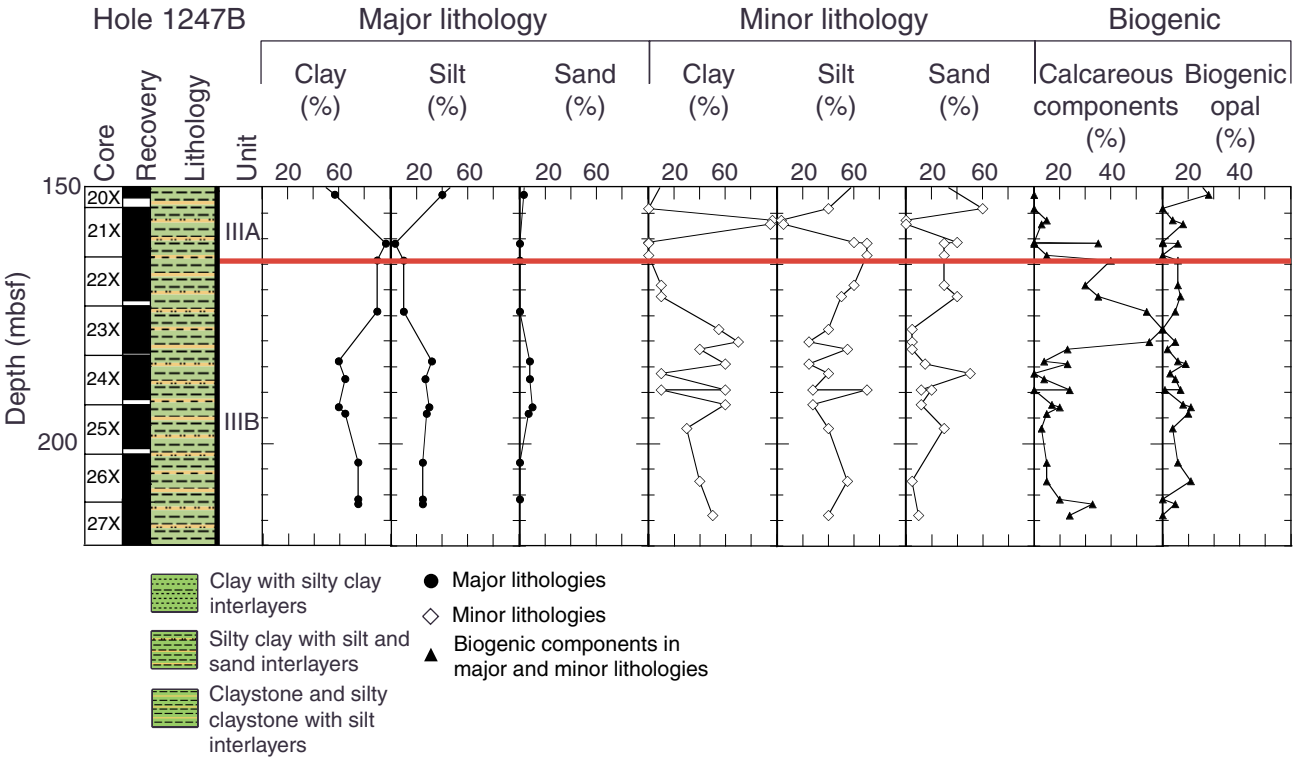

Figure F4. Seismic reflection profile from west (left) to east (right) and LWD density/resistivity logs from Site 1247. Lithostratigraphic units and subunits distinguished at Site 1247 are depicted. Notice the difference in seismic signature at Holes 1247A and 1247B. BSR = bottom-simulating reflector, RAB = resistivity at the bit.

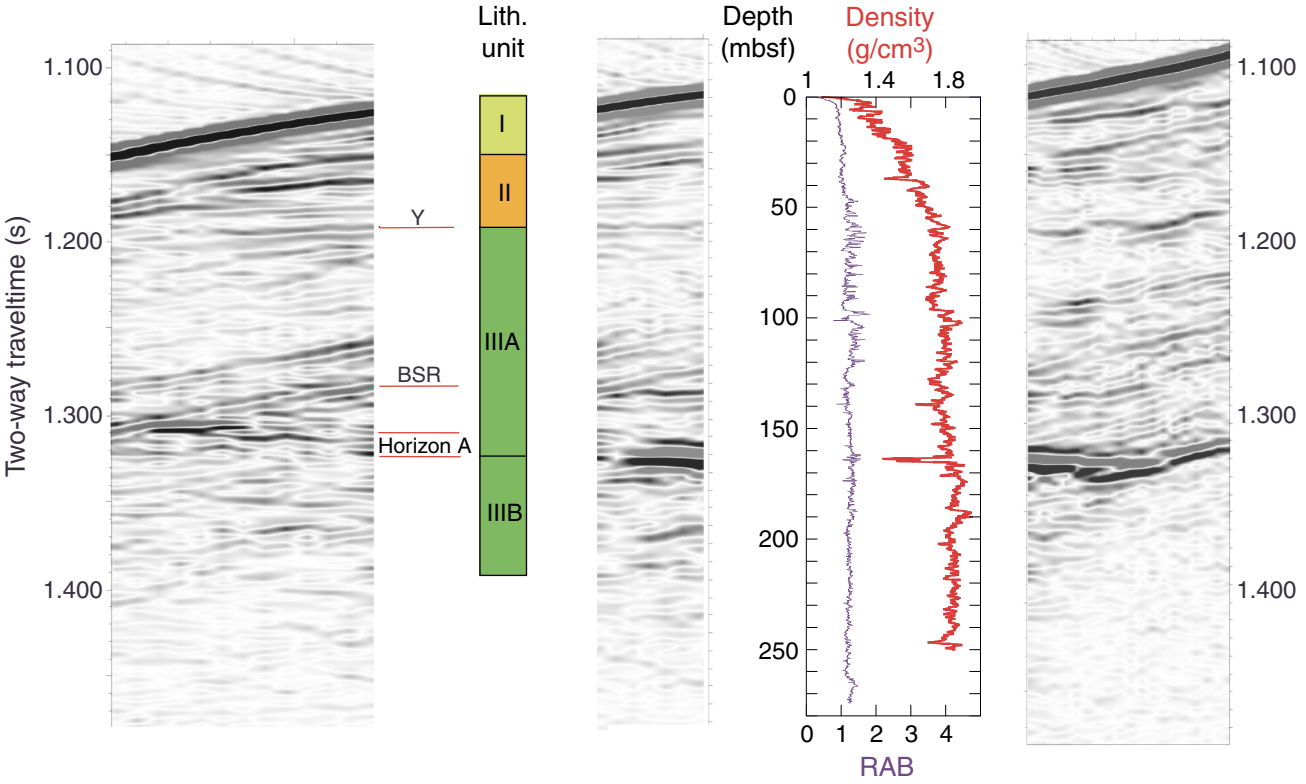

Figure F5. Close-up photograph of authigenic carbonate-cemented sediment (light patches) identified in lithostratigraphic Unit I (interval 204-1247B-2H-4, 94–135 cm).

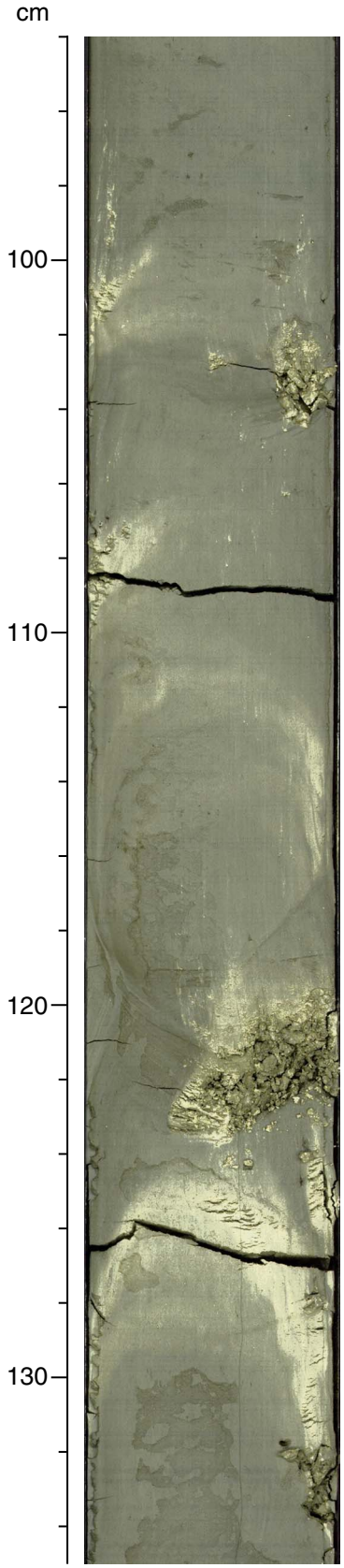

Figure F6. $CaCO_3$ content vs. depth at Site 1247. Lithostratigraphic units are indicated.

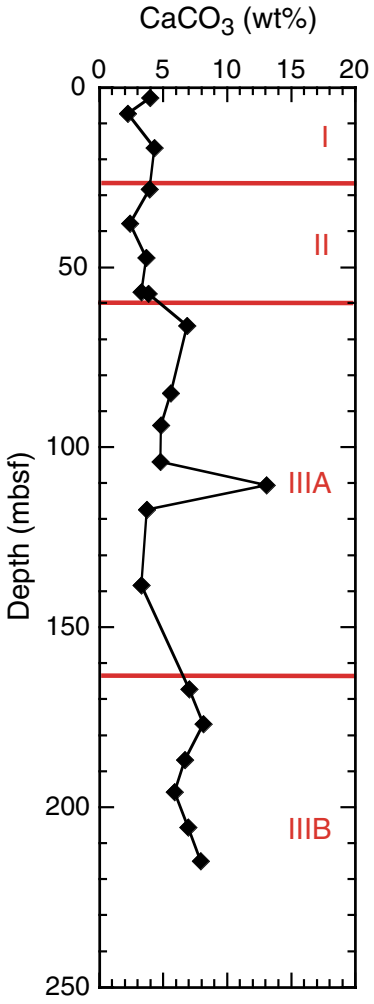

Figure F7. XRD record from carbonate samples taken in lithostratigraphic Unit I. From top to bottom, Samples 204-1247B-2H-1, 43–44 cm; 2H-4, 55–56 cm; and 2H-4, 124–125 cm, respectively.

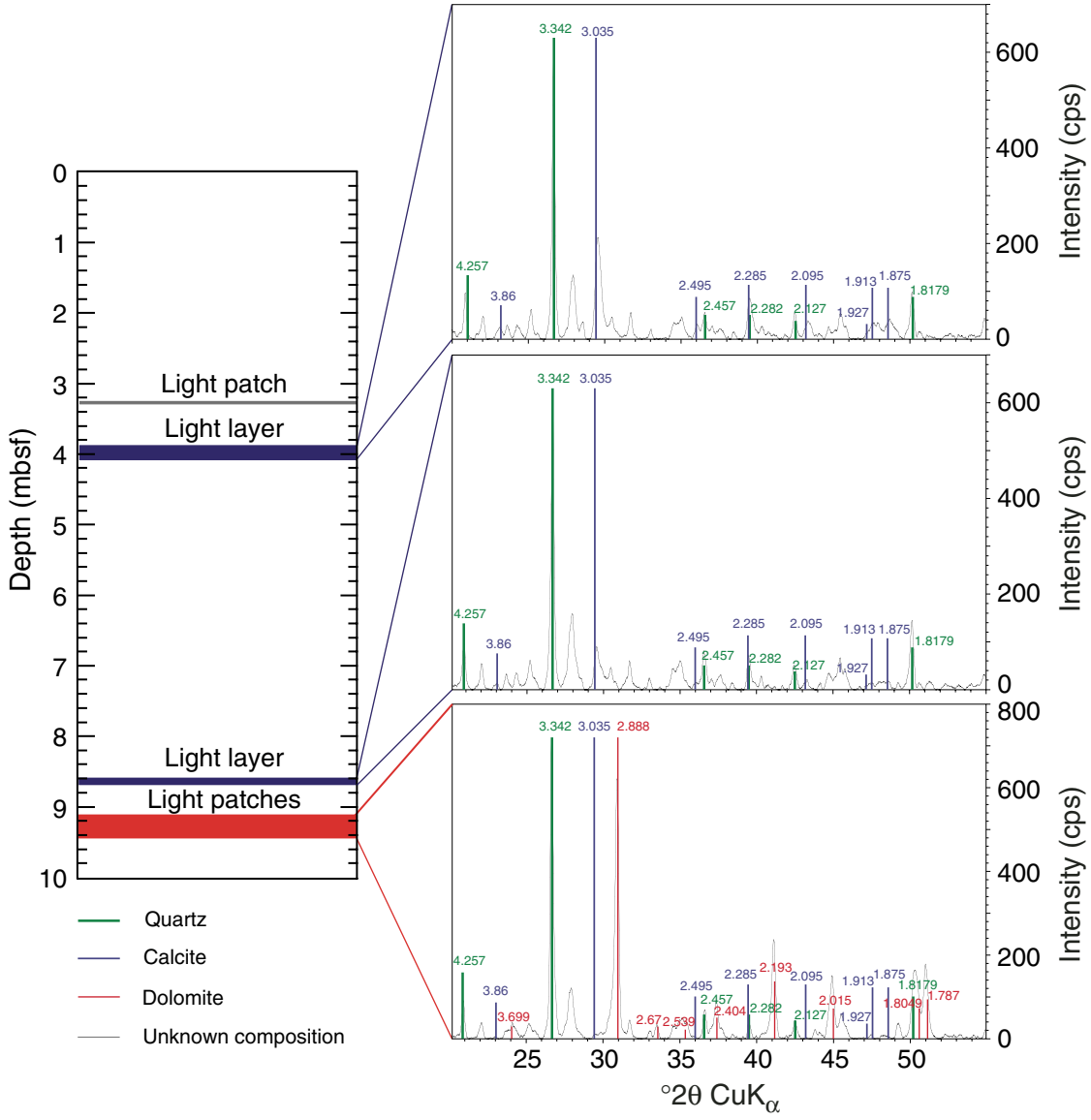

Figure F8. A. Close-up photograph of a 10-cm-long pyrrhotite vein (interval 204-1247B-5H-6, 116–135 cm). **B.** High-resolution MS plot of interval 204-1247B-5H-6, 33–33.6 mbsf. A large and narrow peak is associated with the presence of magnetic minerals (pyrrhotite) shown on the close-up photograph.

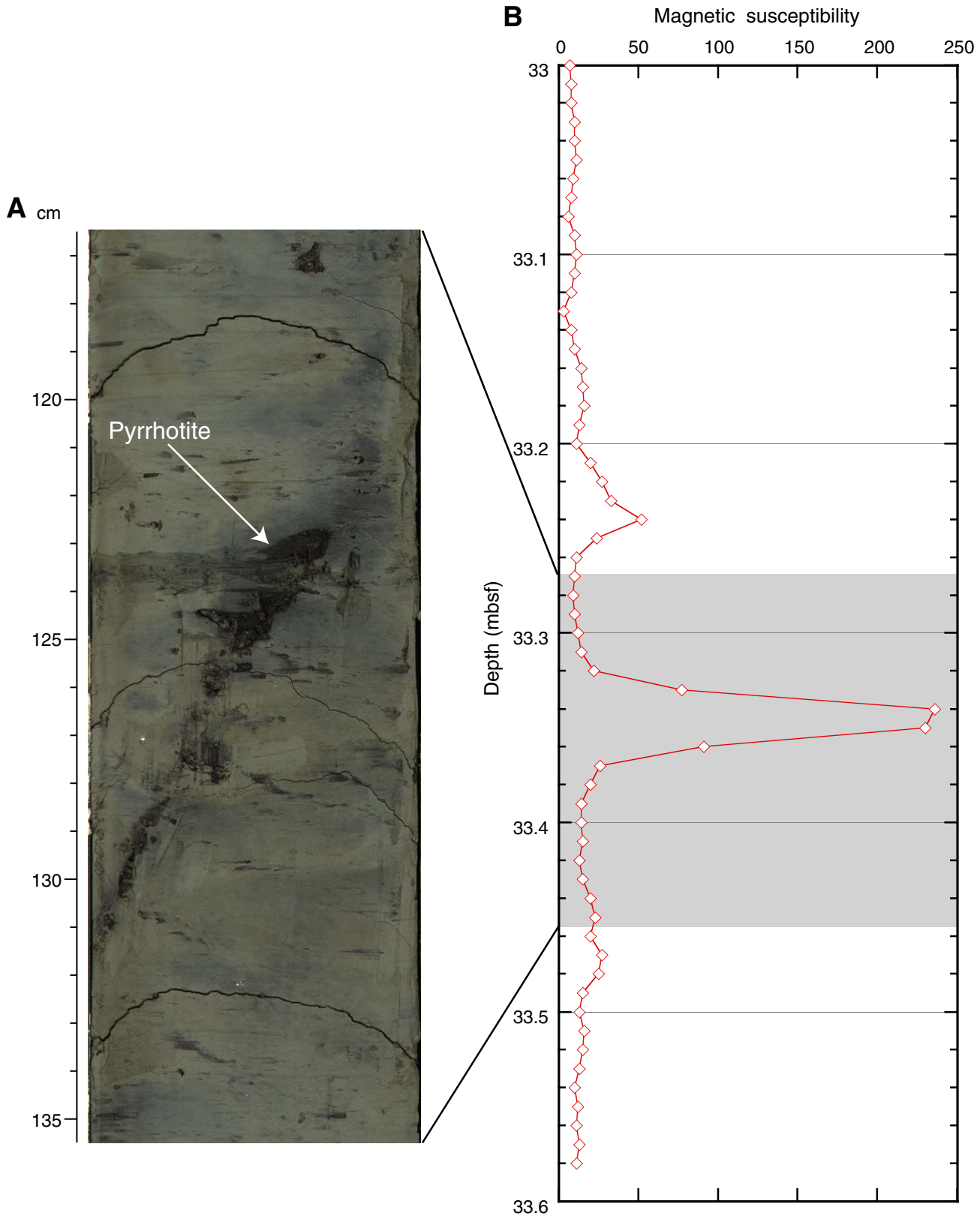

Figure F9. Close-up photograph of a debris flow deposit (interval 204-1247B-21X-4, 95–120 cm).

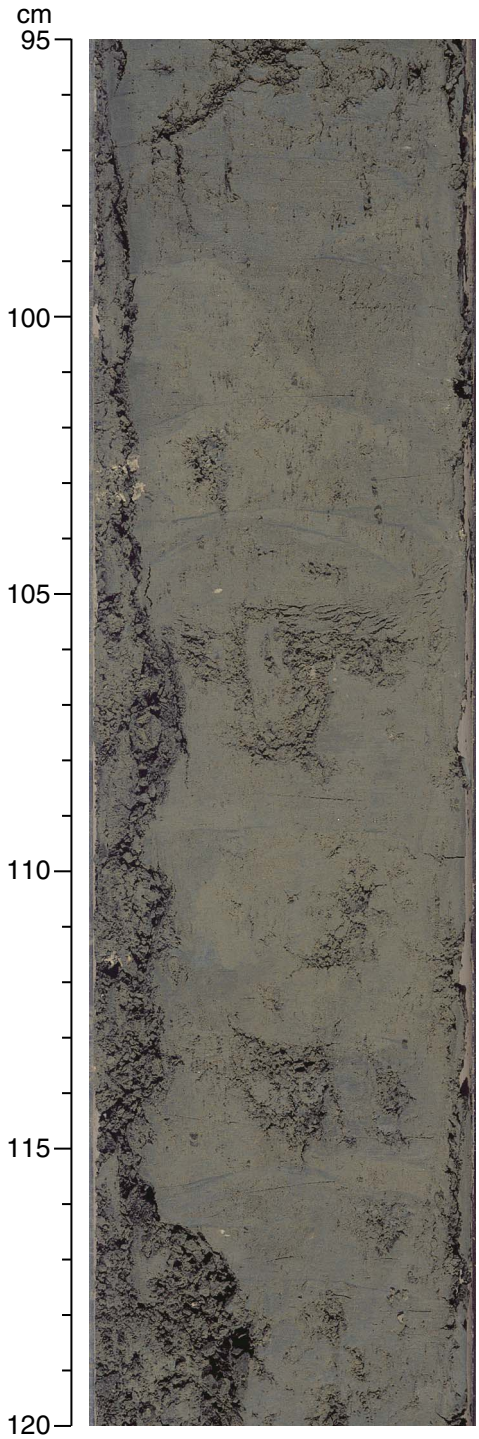

Figure F10. Close-up photograph of a sandy turbidite, with visible foraminifers (interval 204-1247B-23X-1, 104–116 cm).

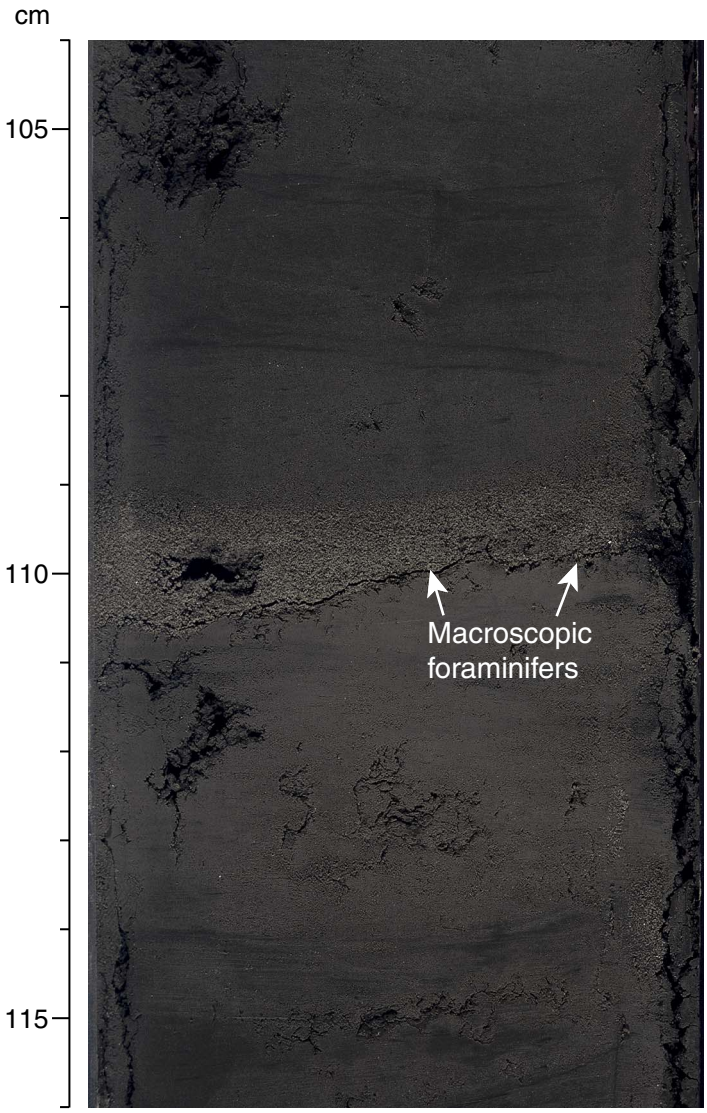

Figure F11. Age-depth plot based on diatom and calcareous nannofossil bioevents for Hole 1247B. The detailed age and depth of control points are shown in Table T3, p. 72. D = diatom event, N = nannofossil event.

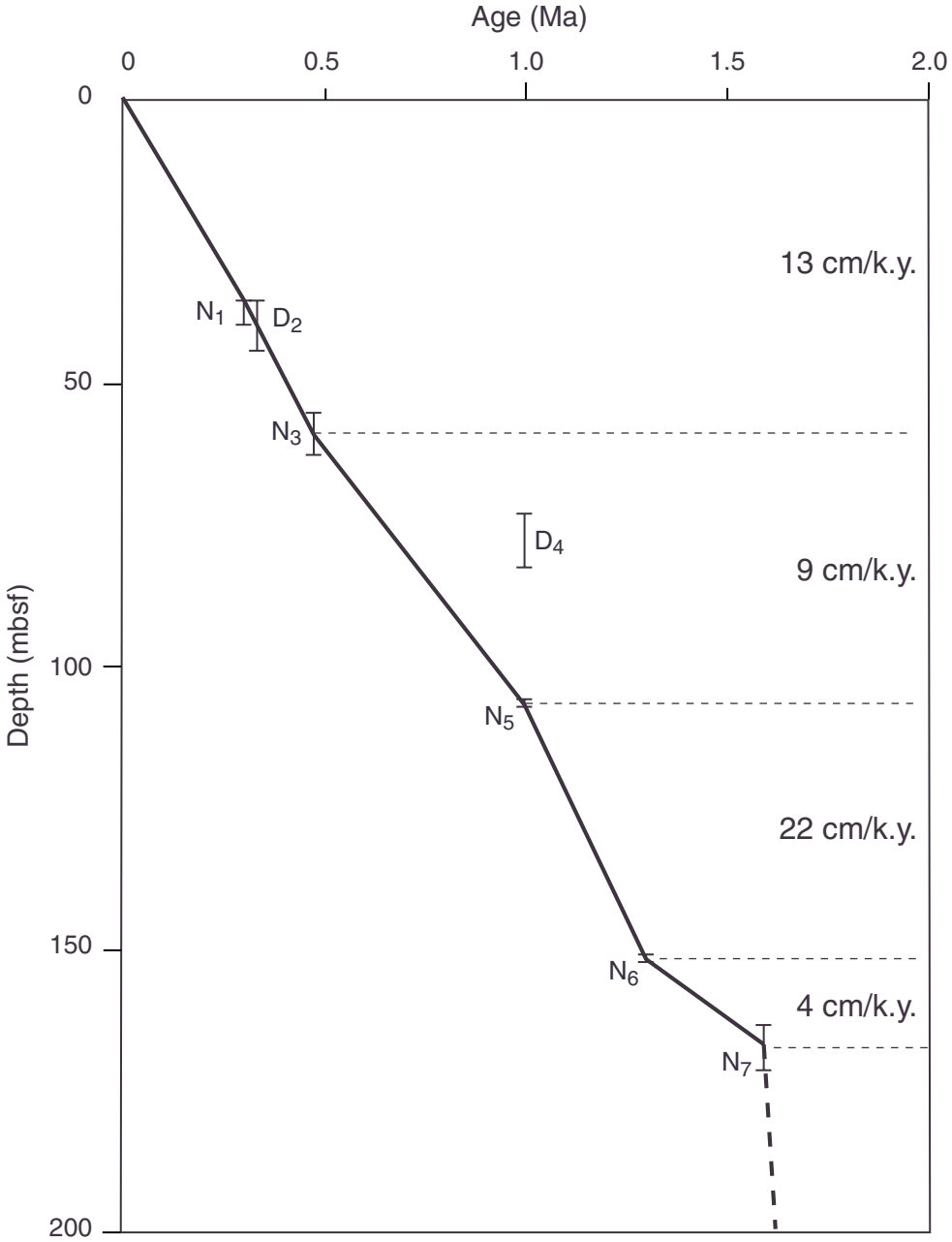

Figure F12. Concentration profiles of various dissolved species in pore waters from Hole 1247B. DOC = dissolved organic carbon. (Continued on next page.)

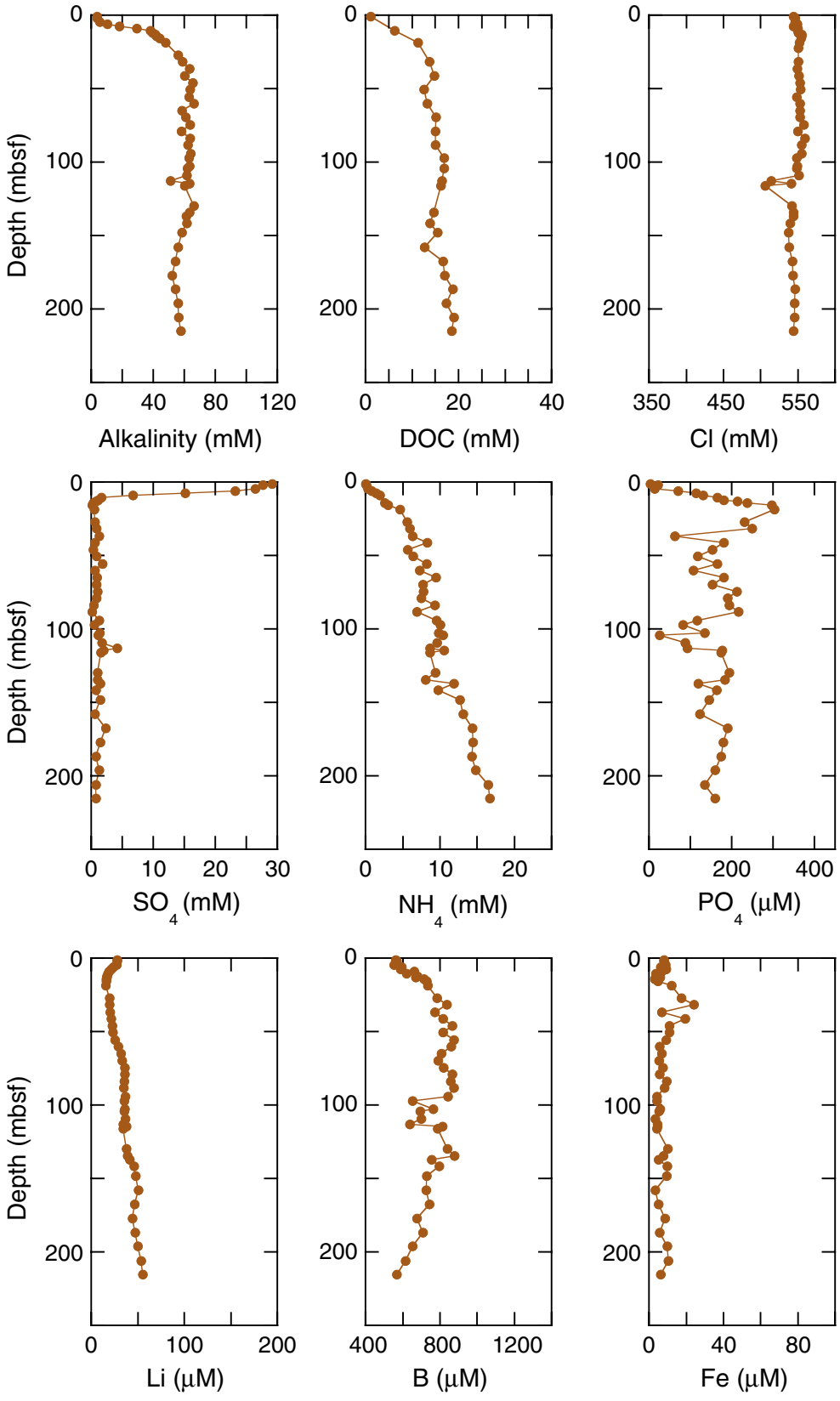

Figure F12 (continued).

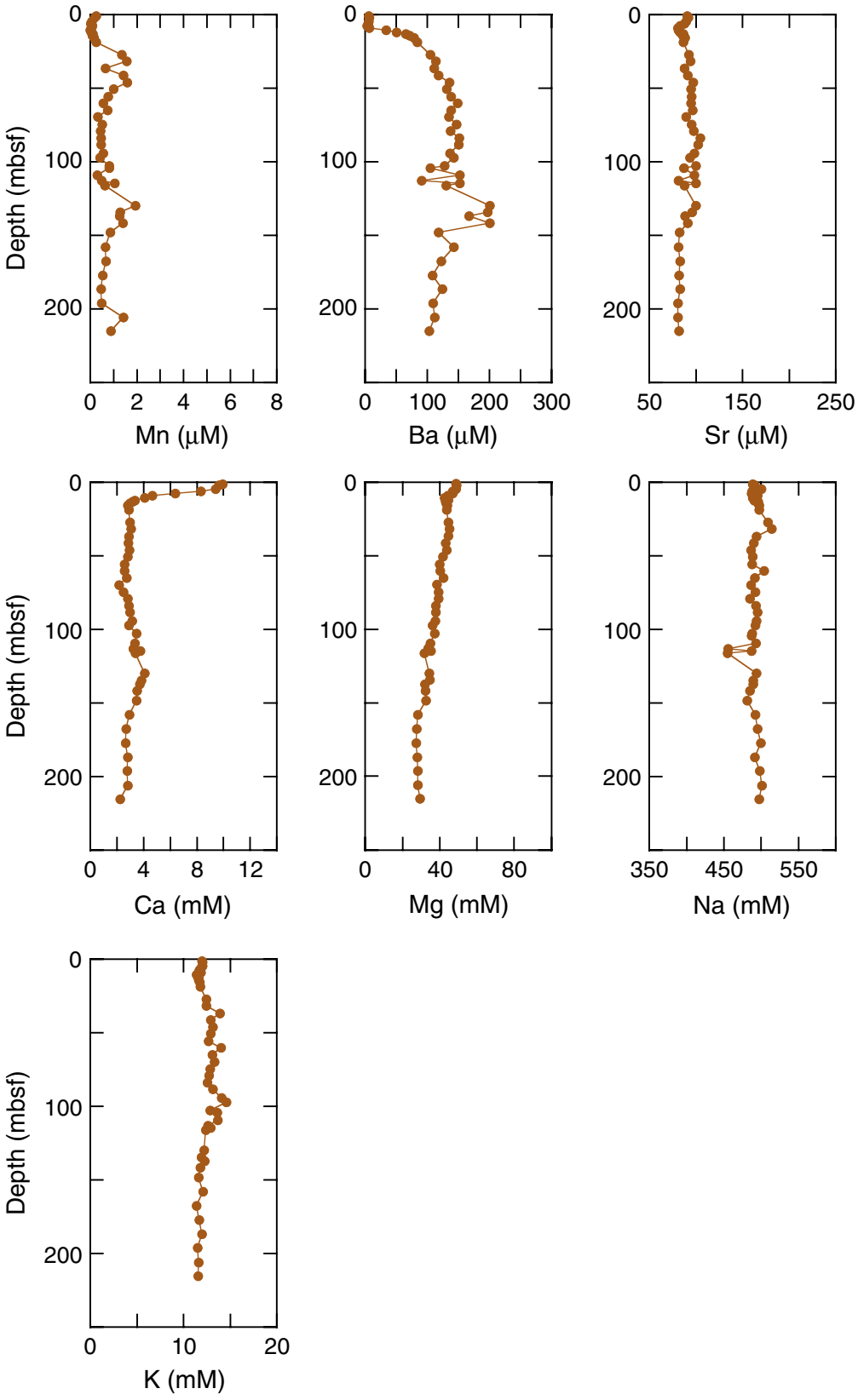

Figure F13. Chloride (Cl^-) concentration profile for Site 1247 and calculation of gas hydrate amounts as a percentage of pore space. Chloride data from Site 1245 (thin line) are shown for comparison. **A.** Chloride concentration data show anomalies toward freshening between ~56 and 116 mbsf, indicating the presence of gas hydrate between these depths. The data form gently sloping baselines with an inflection point at ~85 mbsf. These data are similar to those documented at Site 1245. **B.** Using the baselines established from the chloride data in A, the largest chloride anomaly predicts that about 10% of pore space is filled by gas hydrate at 116 mbsf. Above this depth, 0%–2% of the pore space is occupied by gas hydrate.

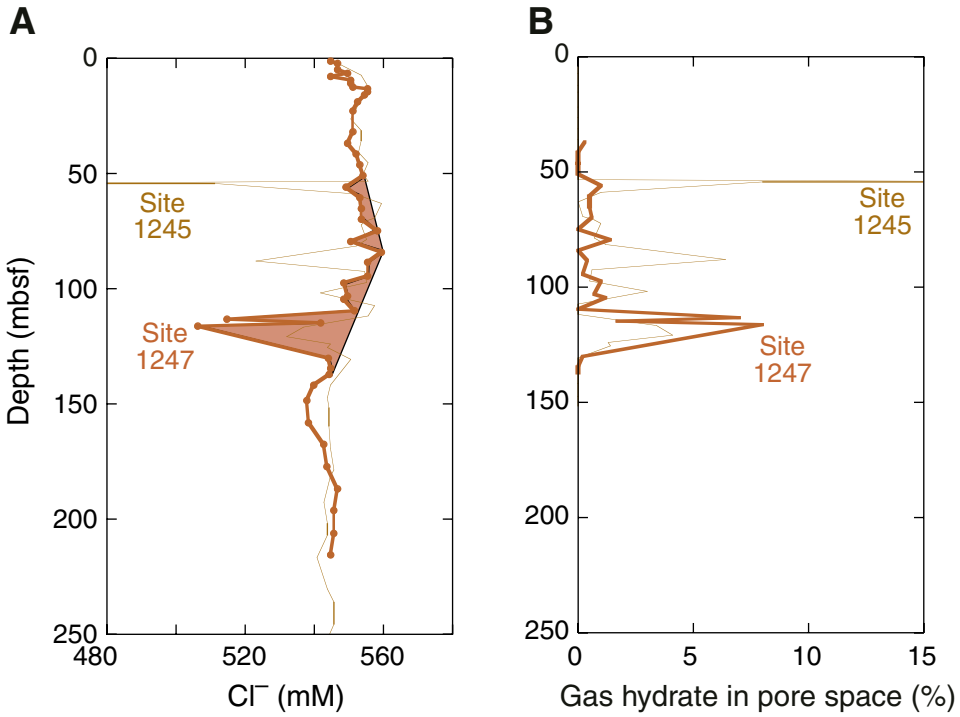

Figure F14. Sulfate (SO_4^{2-}) and methane (CH_4) concentration profiles at Site 1247. The sulfate/methane interface (SMI) is defined where a minimum in sulfate concentration and a rapid increase in methane concentration co-occur, which, at this site, is observed at ~11 mbsf. Note the curvature of the sulfate profile at both the top and bottom of the sulfate-reduction zone. The linear portion of the curve between ~6 and 10 mbsf was used to calculate upward methane flux at this site.

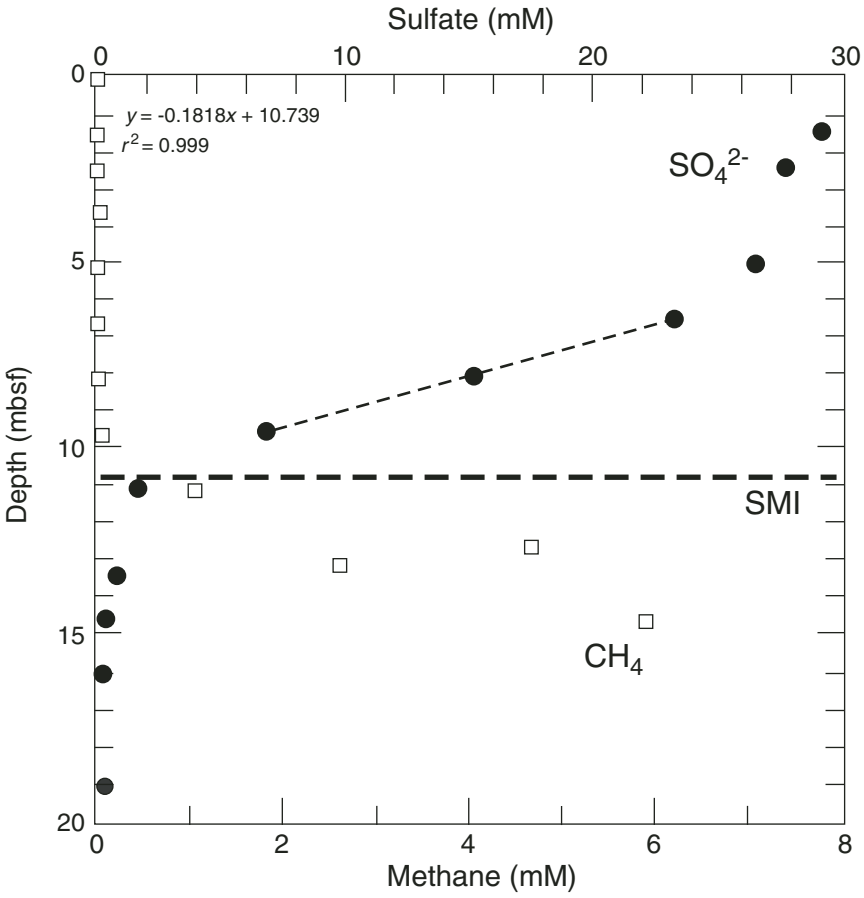

Figure F15. Dissolved lithium (Li^+) concentration profile at Site 1247 (solid circles) shown with those from Site 1245 (dashed line) for comparison. Both data sets show an increase in lithium concentration with depth. At the depth of Horizon A there is an enrichment in interstitial lithium at both Sites 1245 and 1247, perhaps indicating fluid migration from deep-seated fluids.

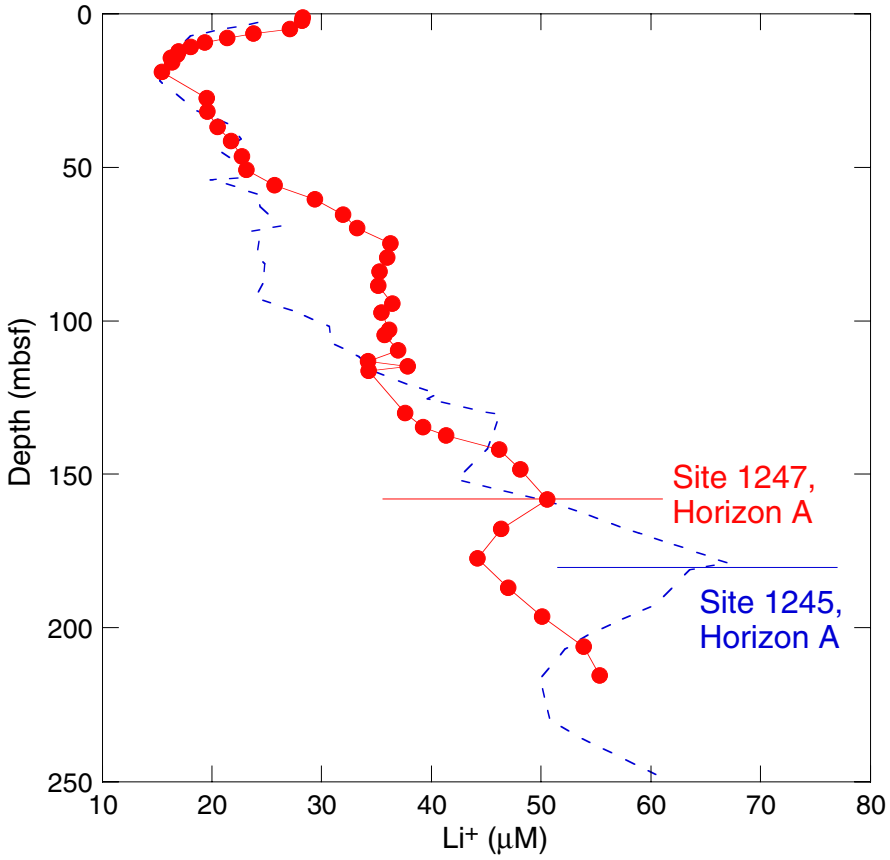

Figure F16. C_1, C_2, $C_{2=}$, and C_3 vs. depth from Hole 1247B. Measurements were made using the headspace method.

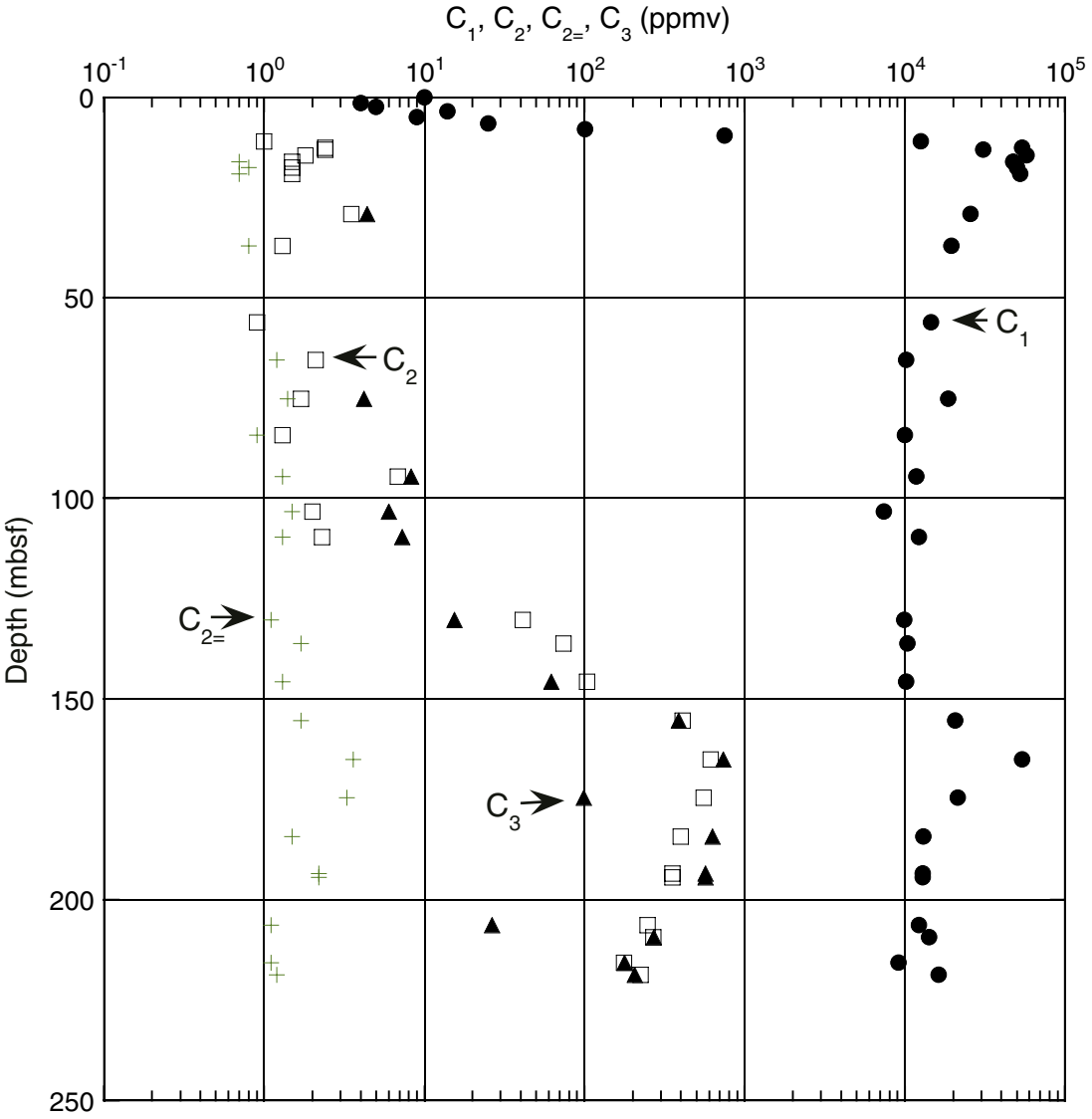

Figure F17. Dissolved residual methane (CH_4) and sulfate (SO_4^{2-}) in pore water. Methane concentration increases at the depth where sulfate concentration is depleted. SMI = sulfate/methane interface.

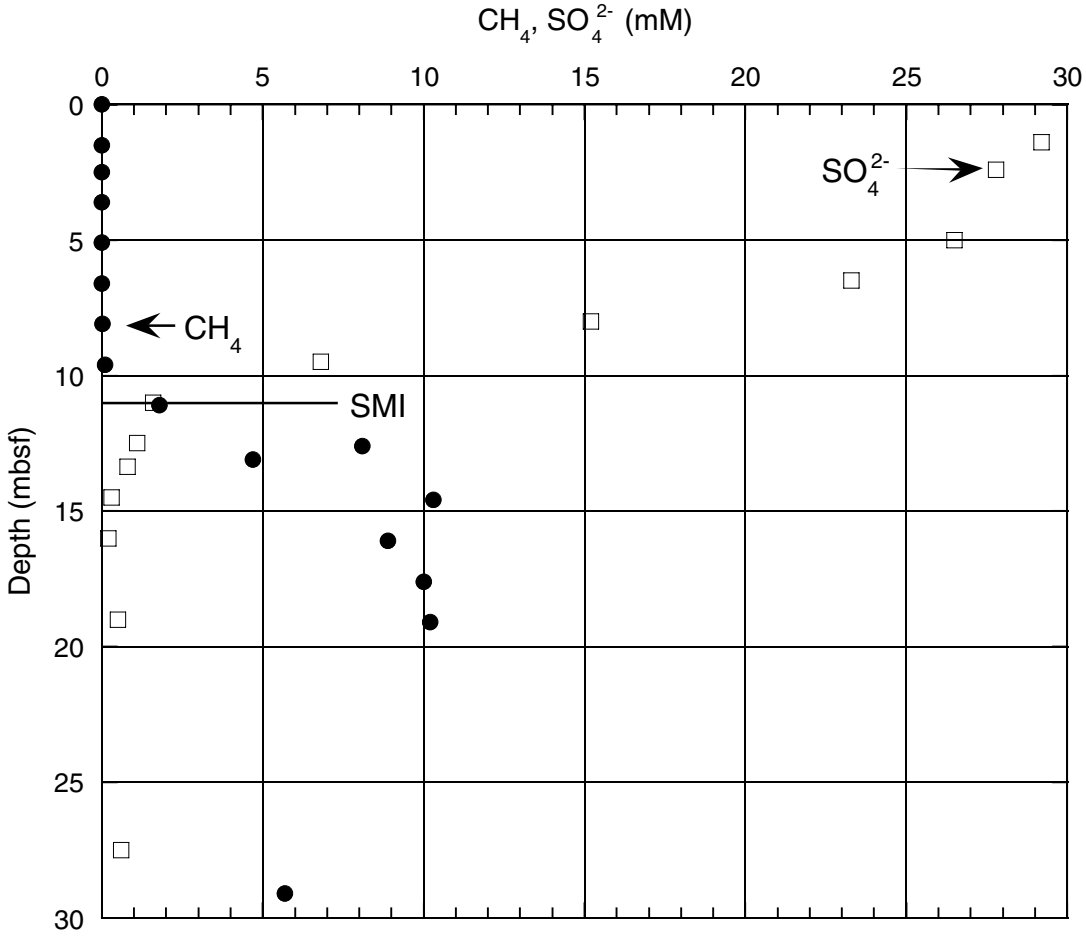

Figure F18. C_1, C_2, C_3, *I*-C_4, *n*-C_4, *i*-C_5, *n*-C_5, *i*-C_6, and *n*-C_6 vs. depth from void gas in Hole 1247B.

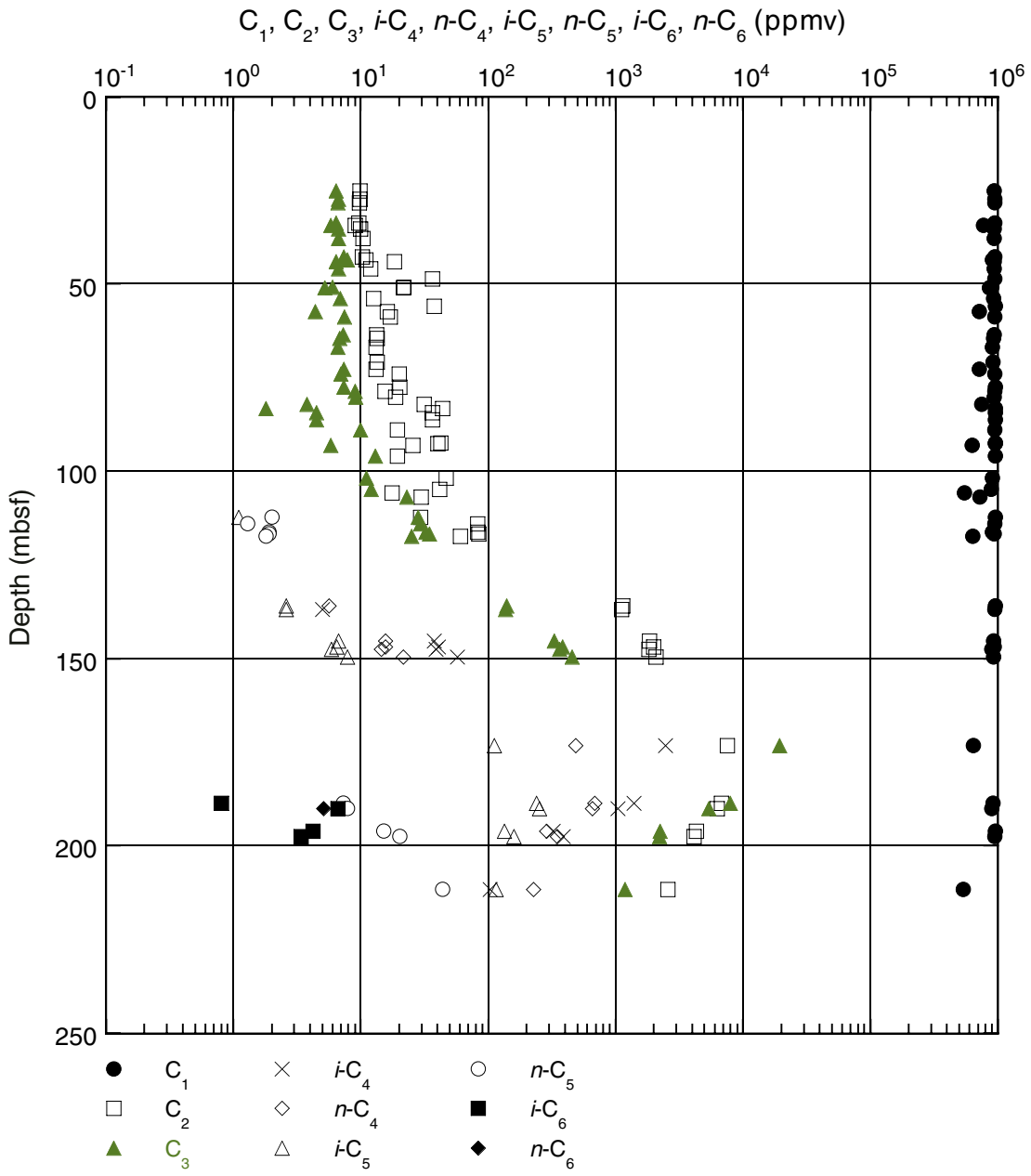

Figure F19. C_1/C_2 ratio vs. depth in Hole 1247B. BSR = bottom-simulating reflector, HS = headspace, VAC = vacutainer, GH = gas hydrate, PCS = pressure core sampler.

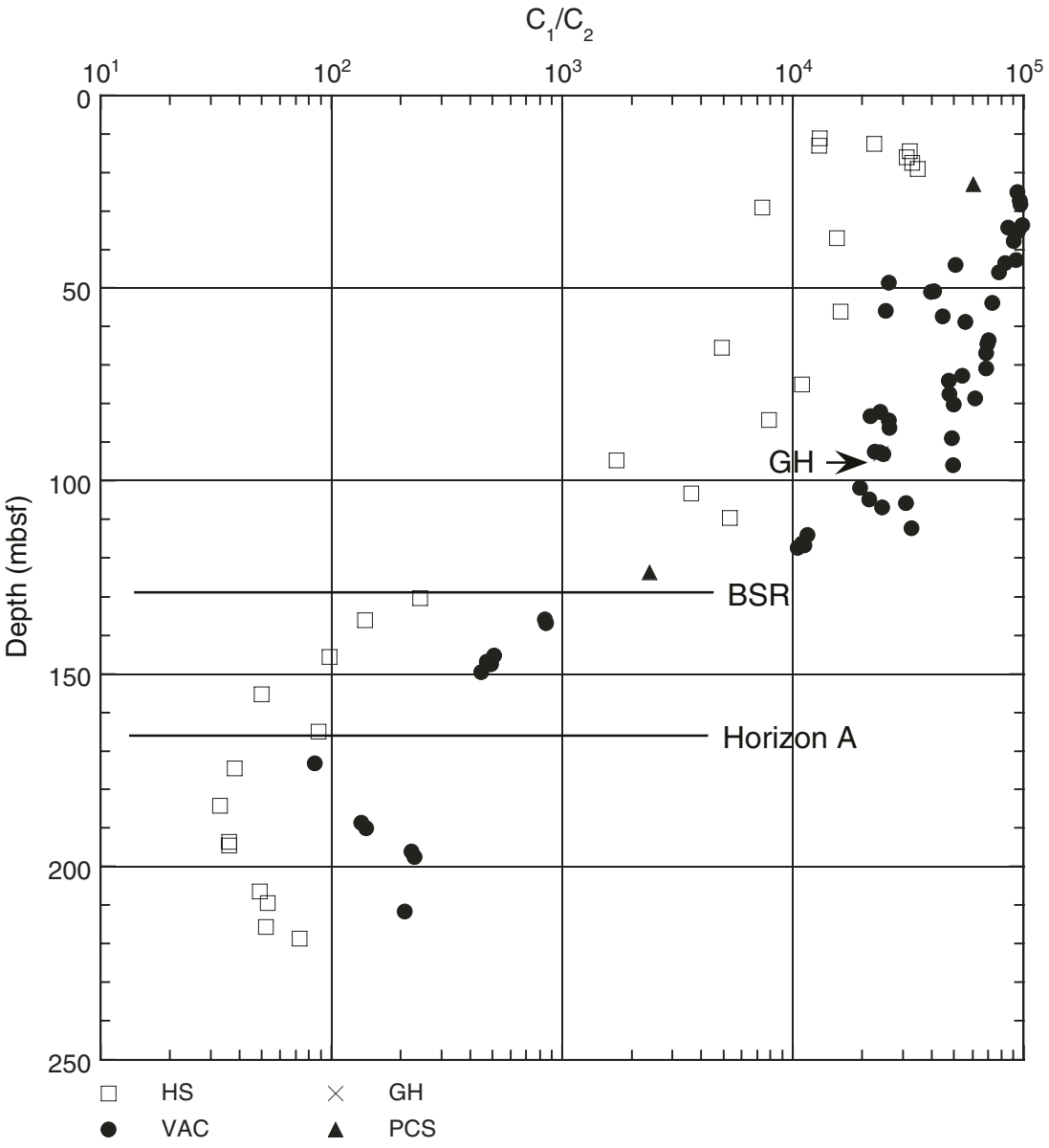

Figure F20. C_1/C_2 ratio vs. temperature in Hole 1247B. HS = headspace, VAC = vacutainer.

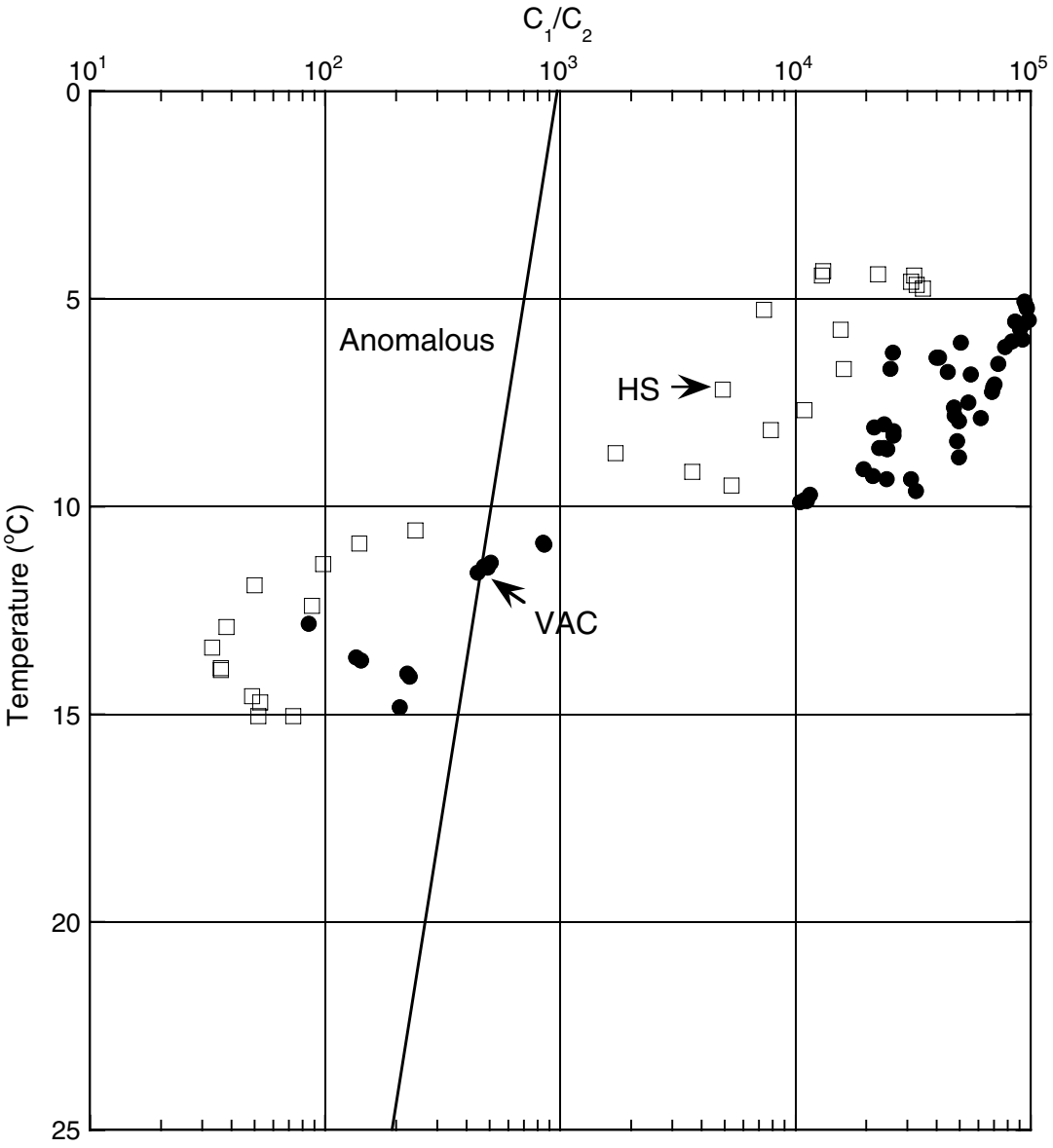

Figure F21. Downcore variation in carbonate carbon (IC), organic carbon (OC), total nitrogen (TN), total sulfur (TS), and C/N ratios in sediment from Hole 1247B. $CaCO_3$ = calcium carbonate.

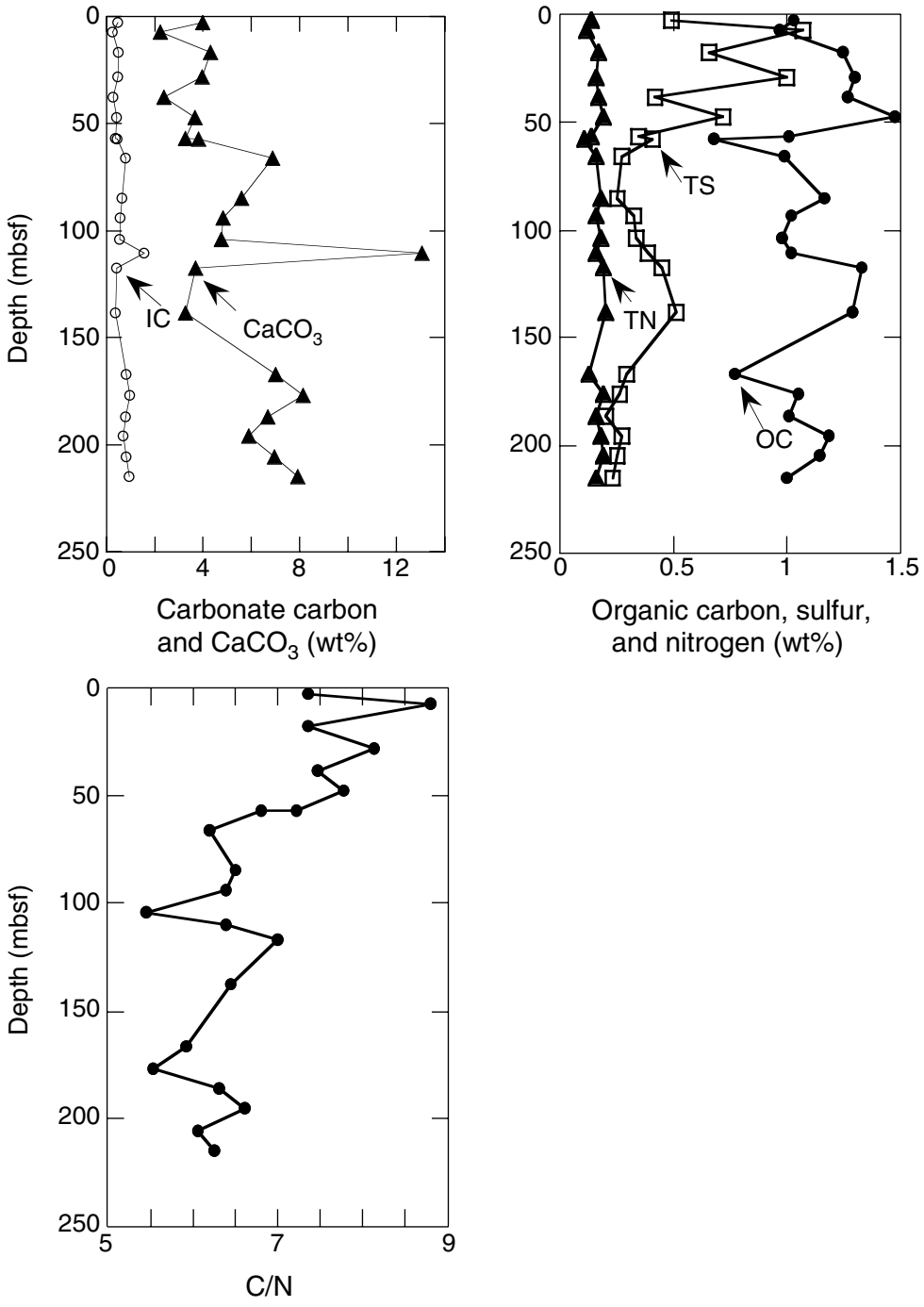

Figure F22. Downhole temperature profile derived from IR thermal imaging data in Hole 1247B. The locations of hydrate samples are indicated by arrows. BSR = bottom-simulating reflector.

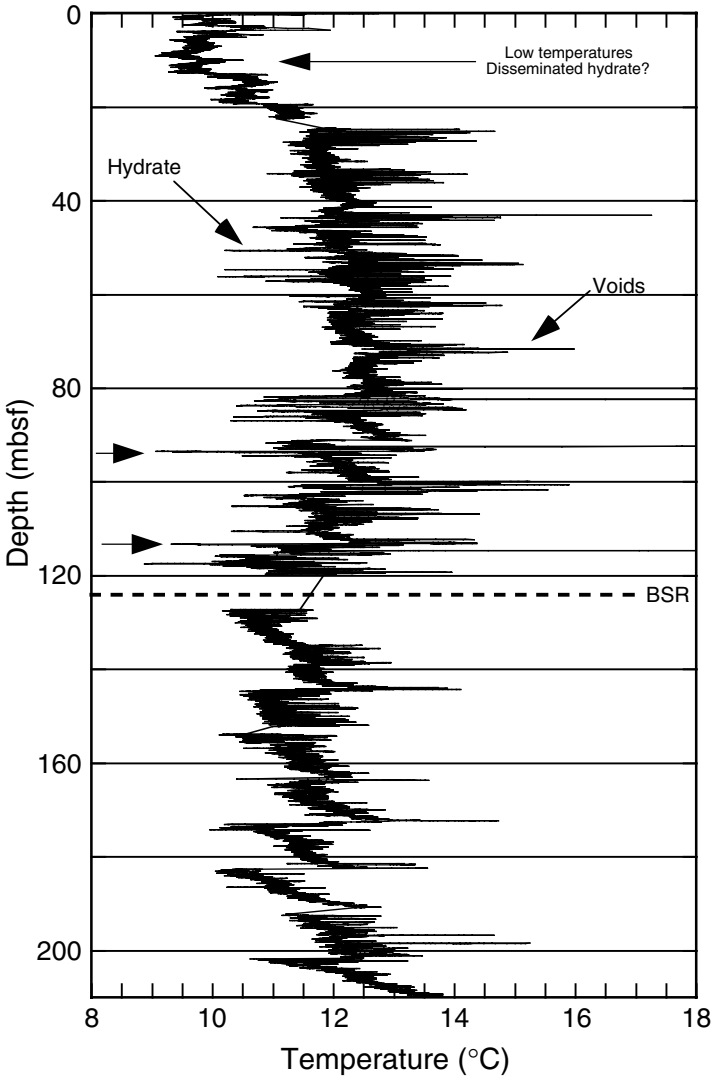

Figure F23. Comparison of temperature anomalies in the IR profile (ΔT) and S_w as calculated from LWD resistivity data at Site 1247. Resistivity data are plotted in terms of apparent S_w using Archie's Relation; the estimated hydrate concentration is 1.0 – S_w (see **"Downhole Logging,"** p. 19). BSR = bottom-simulating reflector.

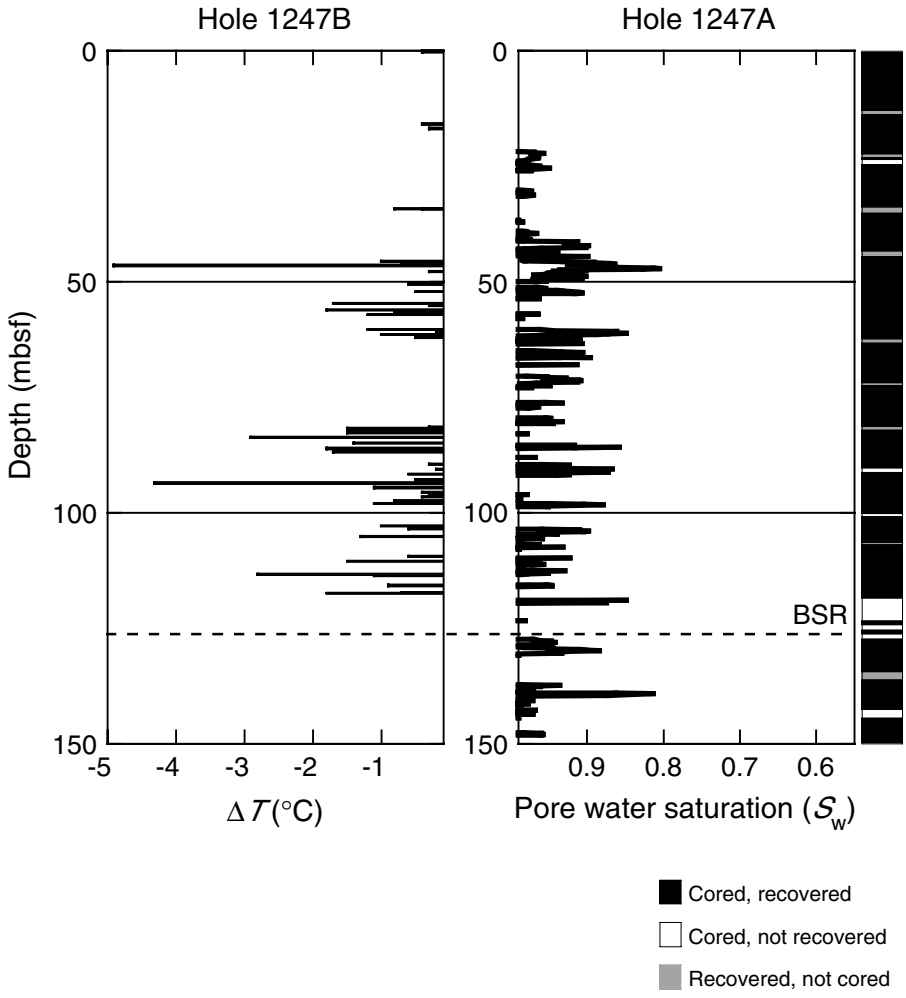

Figure F24. Overview of physical properties at Site 1247. The location of moisture and density (MAD) samples described in the text and shown in Fig. F27, p. 55, are indicated. See Figures F5, p. 55, and F6, p. 56, both in the "Leg 204 Summary" chapter. LWD = logging-while-drilling. GRA = gamma ray attenuation density, MAD = moisture and density.

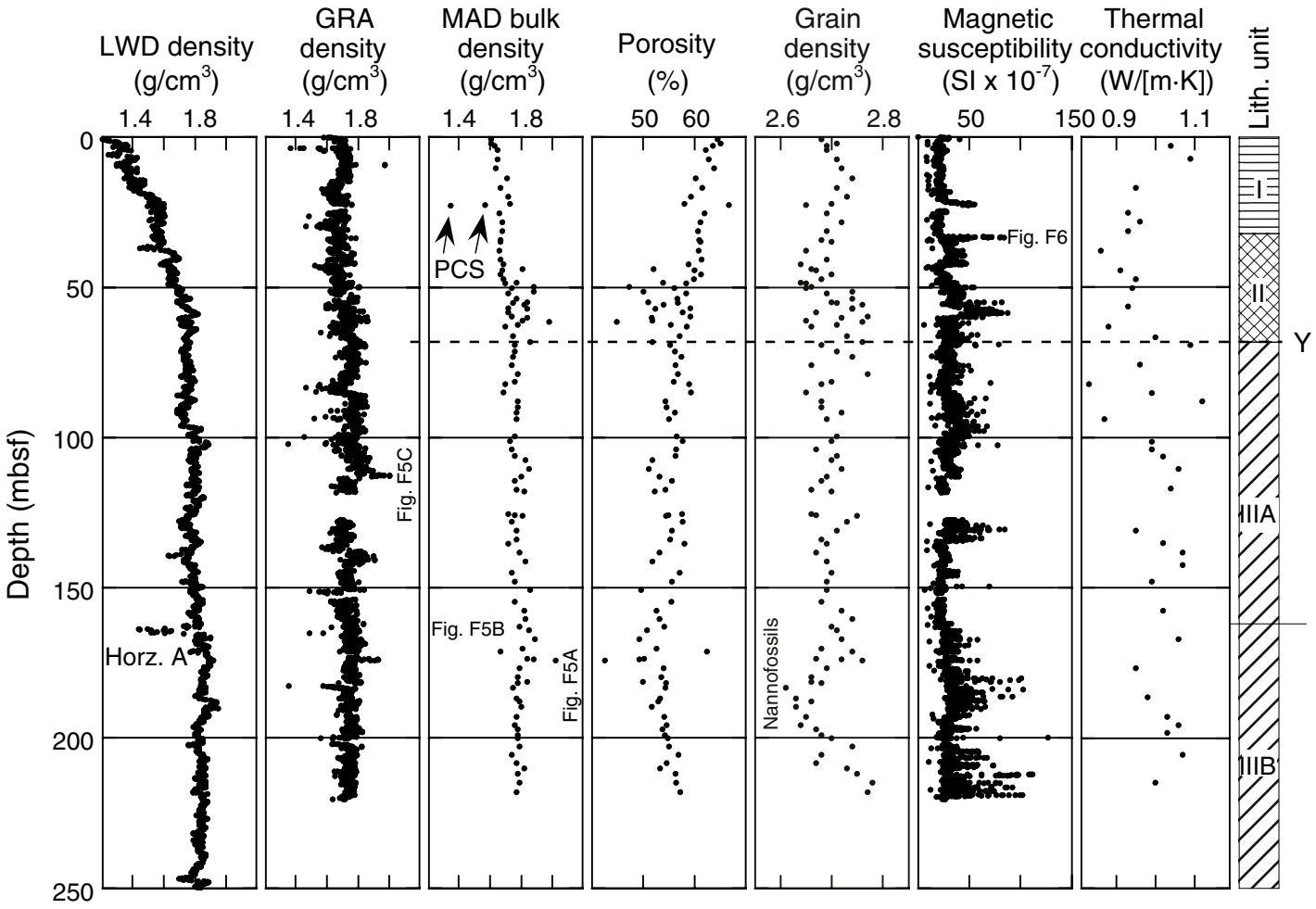

Figure F25. Comparison of physical properties and IR temperature anomalies with 3-D seismic data at Site 1247. IR temperature anomalies and MS are from Hole 1247B and logging-while-drilling (LWD) density and S_w are from Hole 1247A. Horz. = horizon.

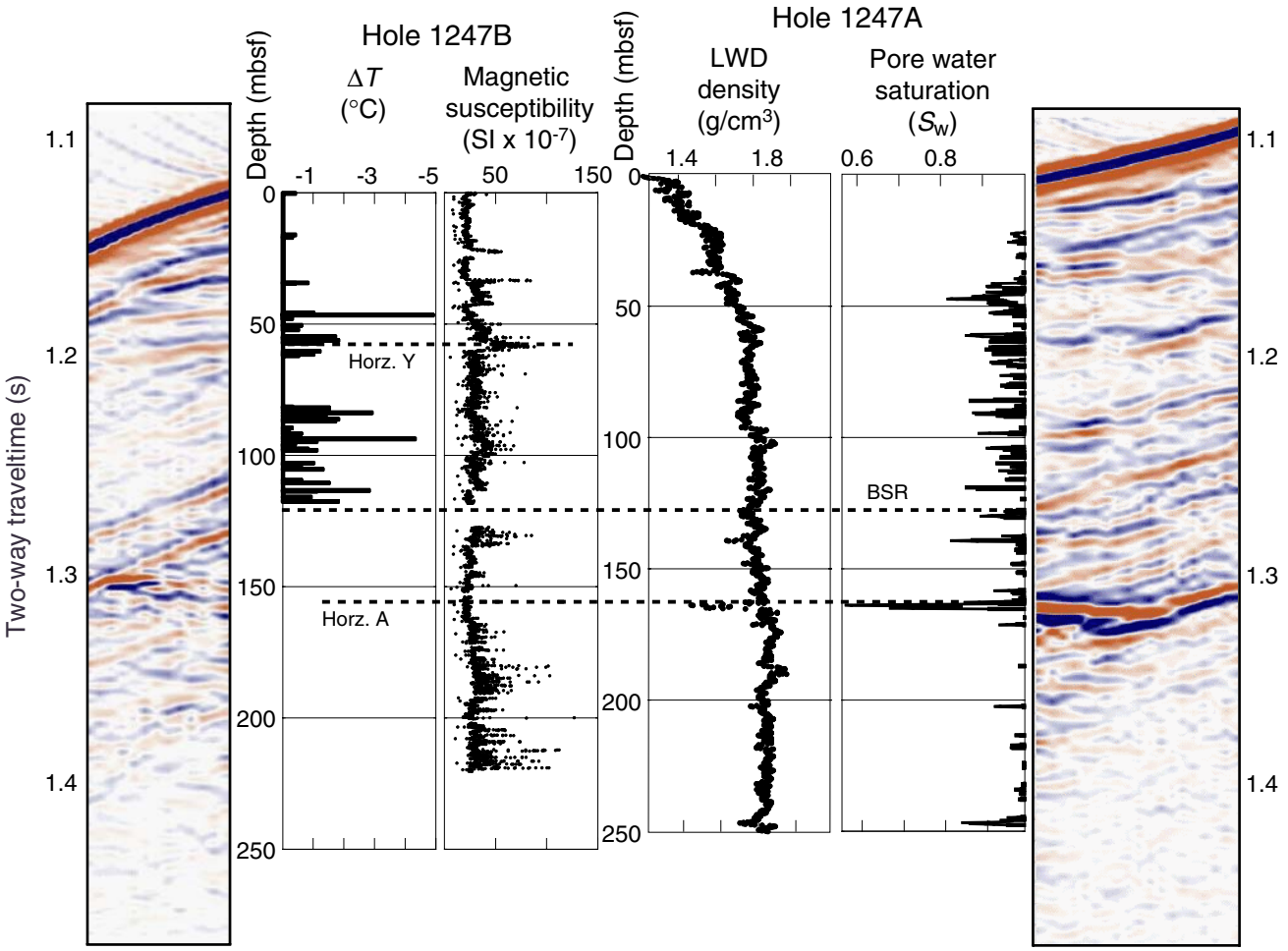

Figure F26. Examples of MAD index sample location and relation of bulk density to sedimentological structure of the sediments. **A.** Interval 204-1247B-23X-1, 105–115 cm (bulk density = 2.02 g/cm³) **B.** Interval 204-1247B-22X-6, 20–35 cm. (bulk density = 1.67 g/cm³) **C.** Interval 204-1247B-14H-5, 0–40 cm, with bioturbation-related sulfide structure (bulk density = 1.81 g/cm³).

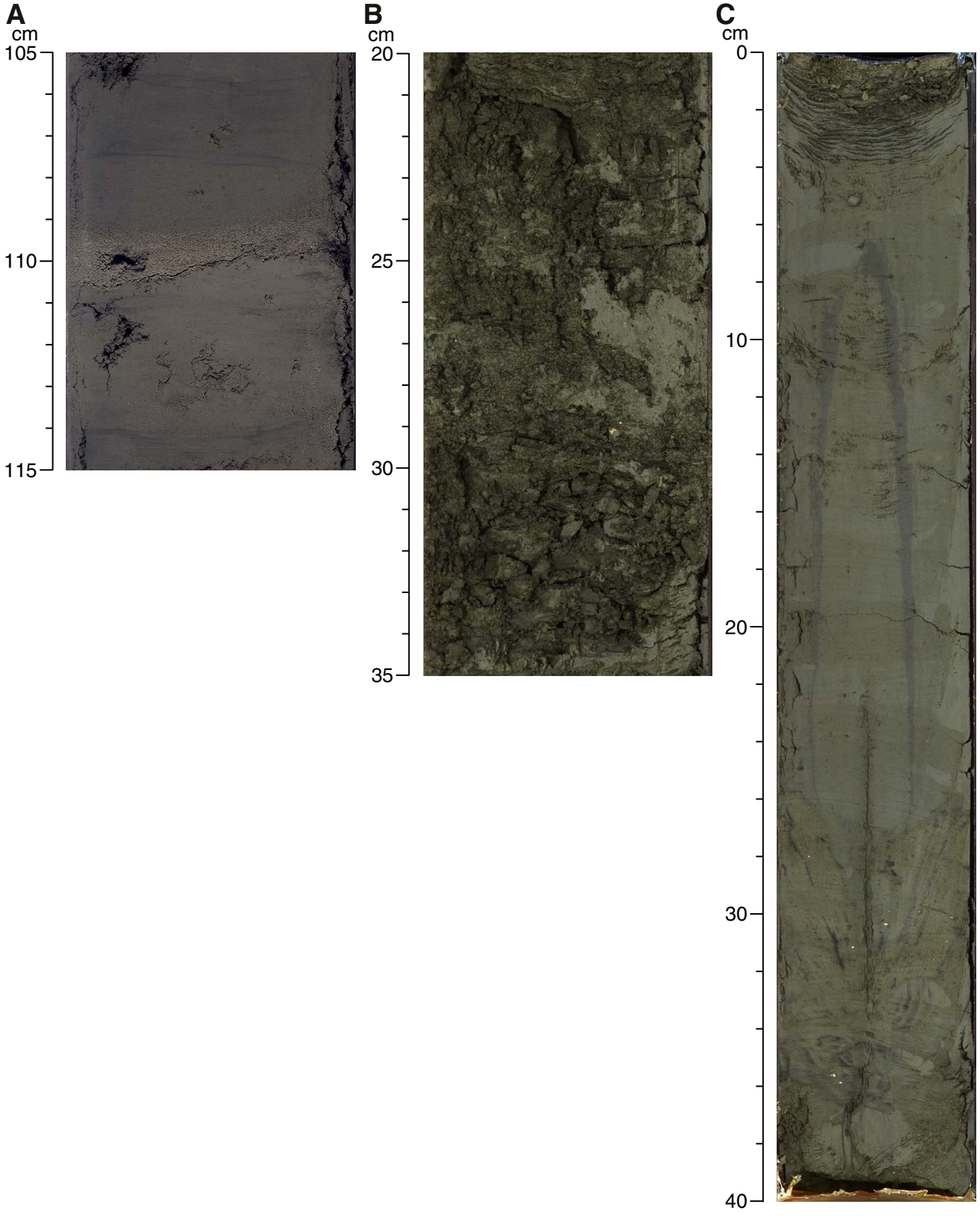

Figure F27. Close-up photograph of sulfide vein in Section 204-1247B-5H-6 and MS profile. Sulfide concretion contains pyrrhotite, as inferred from XRD analyses.

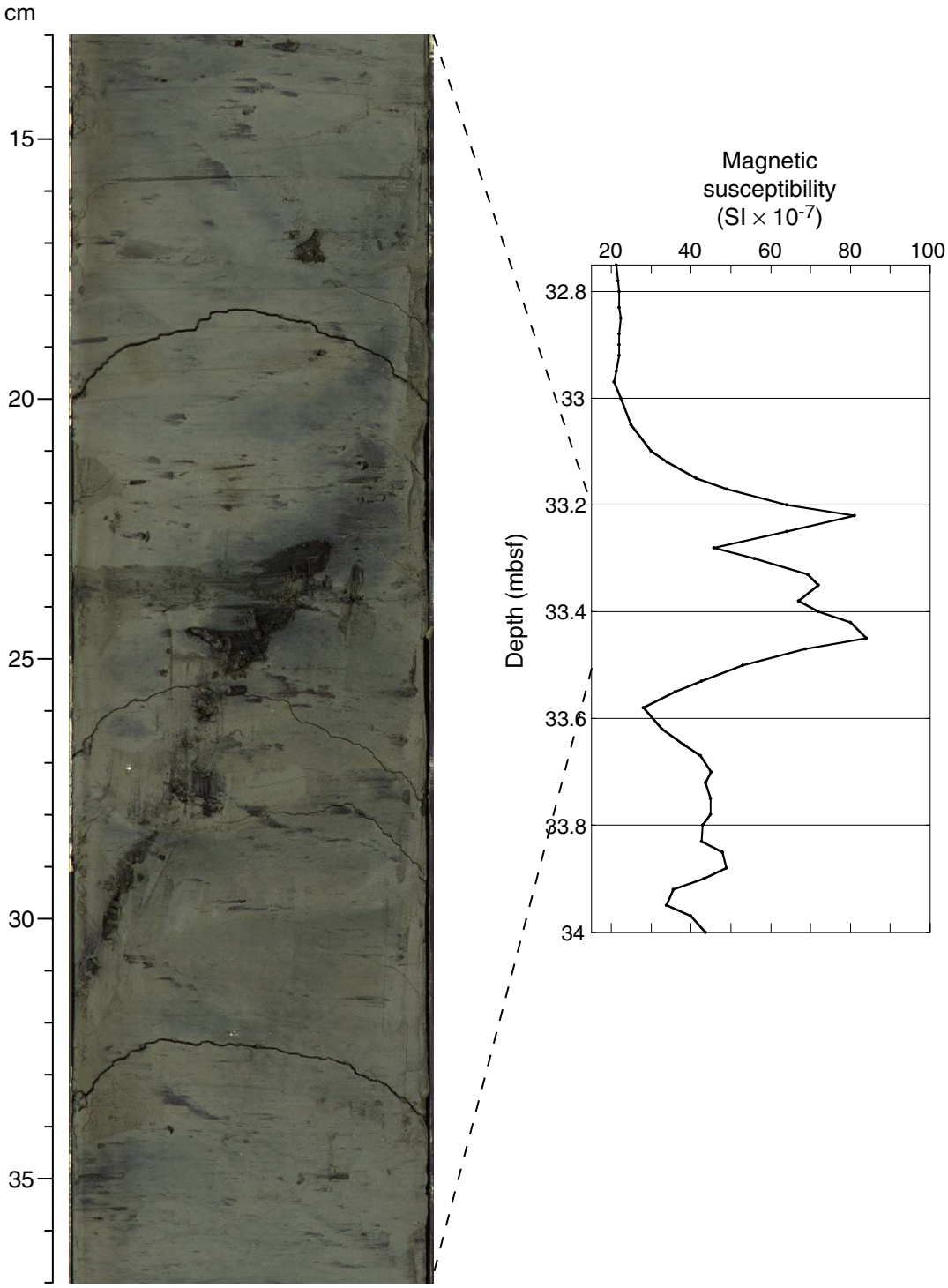

Figure F28. Raw data for estimating in situ temperatures. **A.** APCT tool data. Only the portion of data immediately before, during, and immediately after penetration of the probe into the subsurface is shown. For an example of the entire temperature history of a deployment see **"Downhole Tools and Pressure Coring,"** p. 34, in the "Explanatory Notes" chapter. The ODP core identification number associated with each run of the APCT tool is indicated in the upper left corner of the graph. The measurement depth, mudline temperature, extrapolated in situ temperature estimate, and measured thermal conductivity used for the extrapolation are also shown. **B.** DVTP temperature data. The ODP identification for the core preceding tool deployment, the deployment depth (mbsf), and the measured equilibrium temperature are indicated.

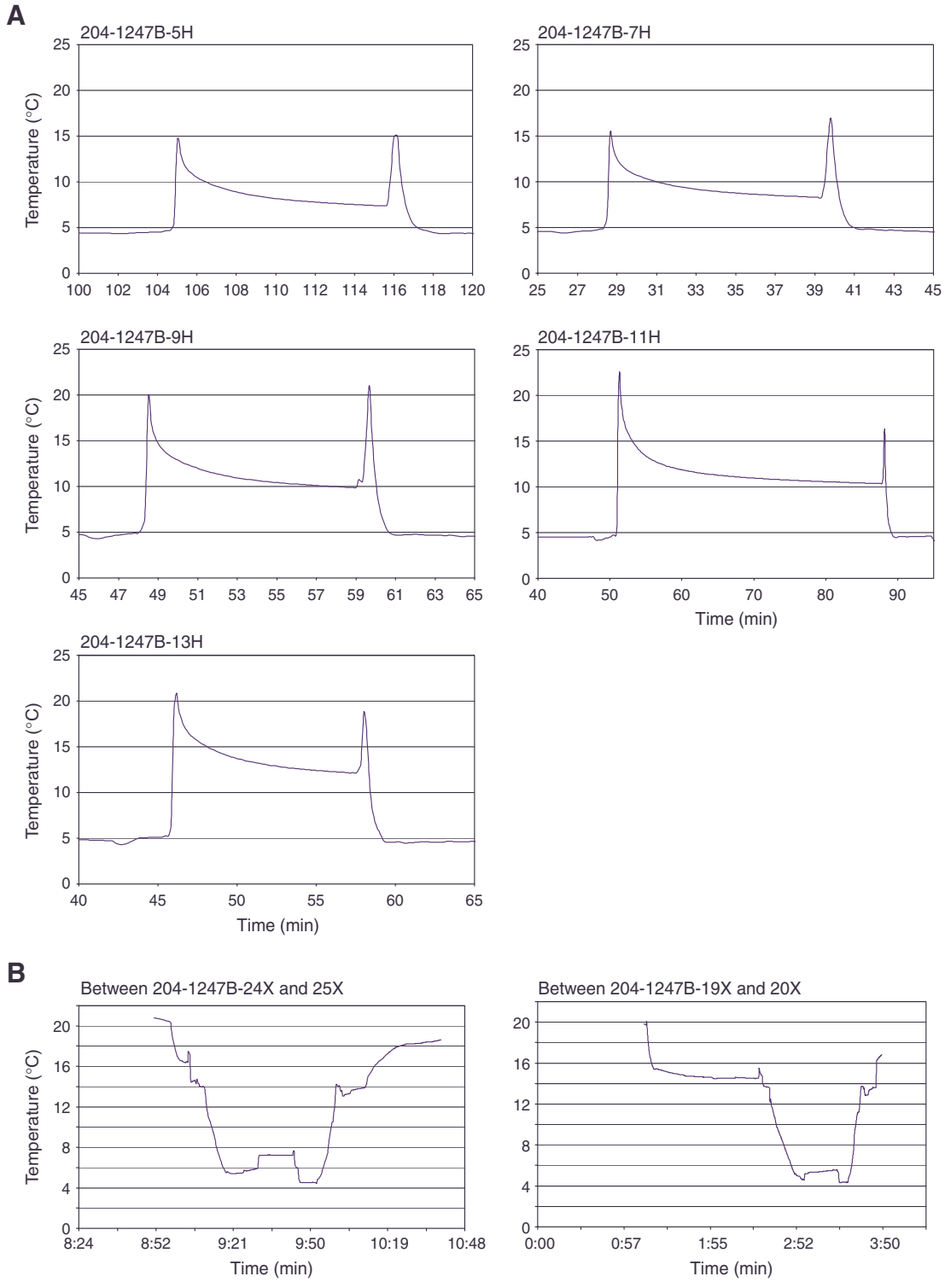

Figure F29. Subsurface temperatures plotted vs. depth beneath the seafloor at Site 1244. The equation for the best fitting linear thermal gradient for all the data, as well as best-fit gradients for several subsets of the data (see explanation in text) are also shown. A calibration correction of 0.51% is indicated, where all measurements were made using APCT 11 (see **"Downhole Tools and Pressure Coring,"** p. 17).

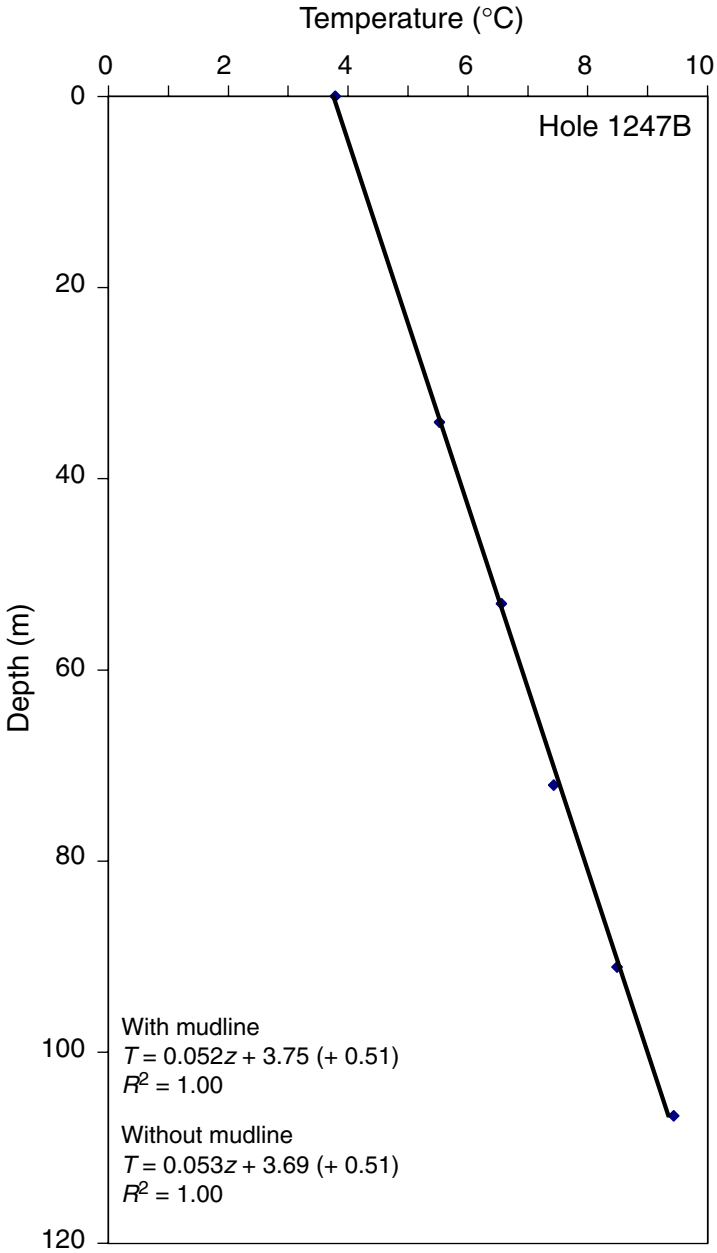

Figure F30. Volume-pressure-time plots for PCS deployed at Site 1247. **A.** Note that Core 204-1247B-4P was not placed on an ice bath since no gas hydrate was expected. **B.** Note that no evidence of gas hydrate decomposition is observed in Core 204-1247B-16P, although methane concentration exceeding solubility in situ was measured.

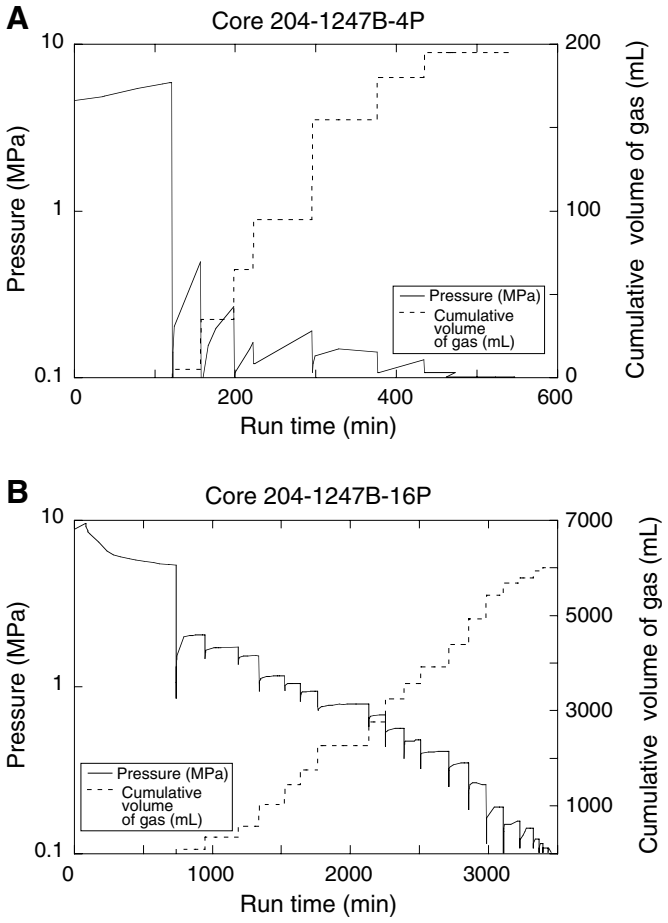

Figure F31. Methane (CH_4) concentration in sediments based on headspace (HS) and pressure core sampler (PCS) data at Site 1247. Estimated theoretical solubility of methane in pore water (extrapolated from values calculated for higher pressures; depths) (Handa, 1990; Duan et al., 1992) is shown and fields of dissolved methane (D), methane hydrate (H), and free methane (F) are depicted. The shaded areas indicate the uncertainties in the position of the boundaries.

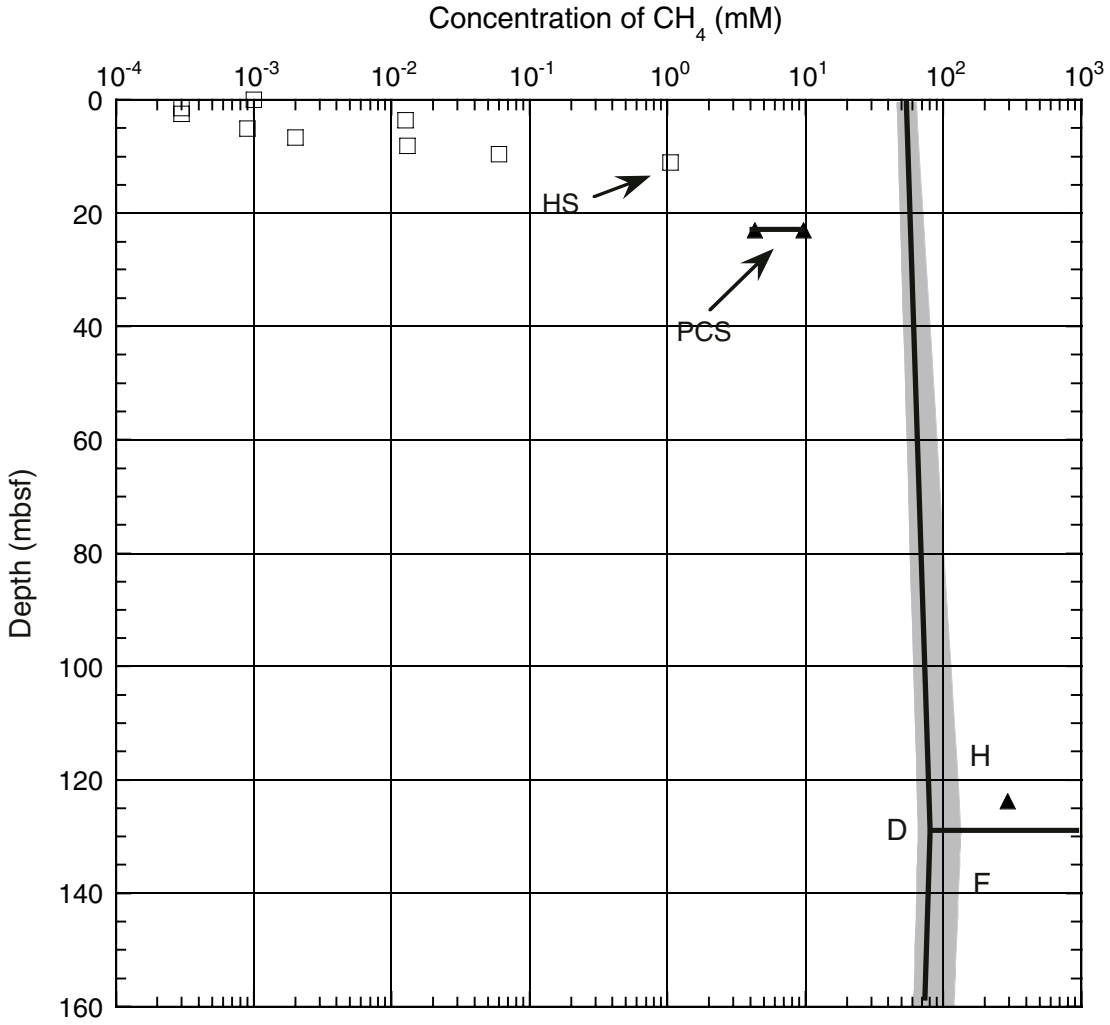

Figure F32. Quality control LWD logs from Hole 1247A. ROP = rate of penetration, TAB = time after bit, Diff. = differential.

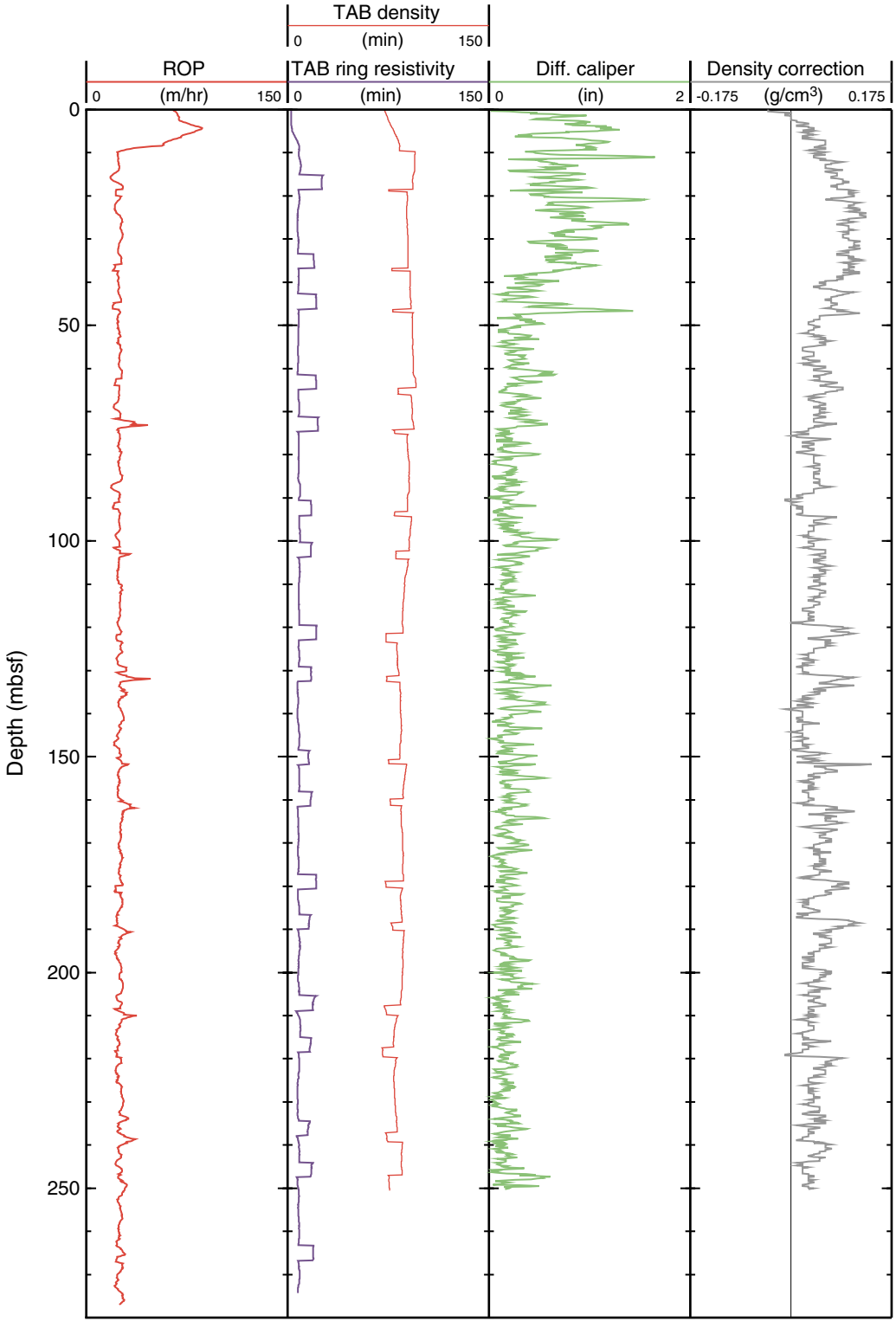

Figure F33. Summary of LWD data from Hole 1247A. gAPI = American Petroleum Institute gamma ray units, PEF = photoelectric effect factor, RAB = resistivity at the bit.

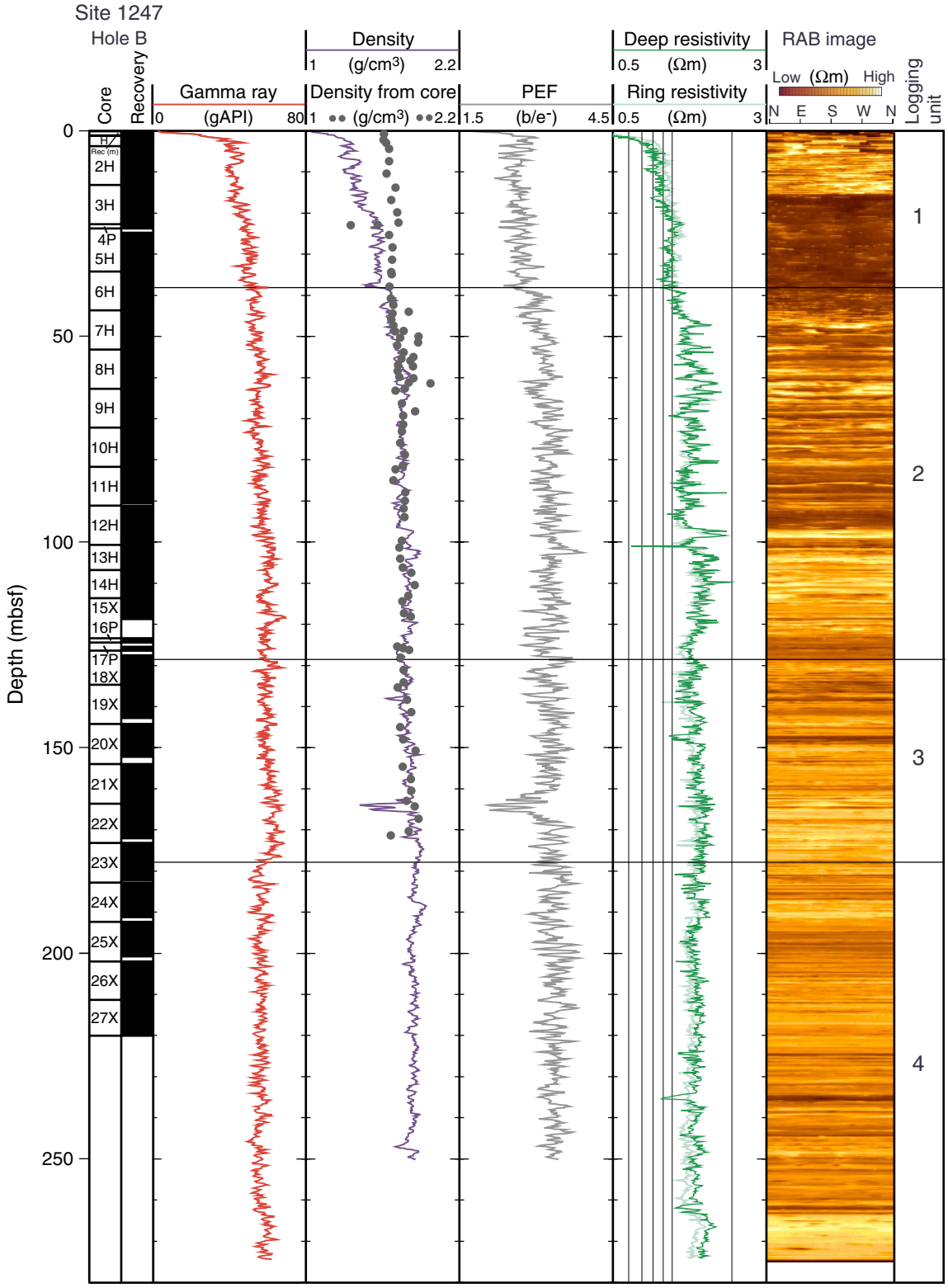

Figure F34. Summary of CWL data from Hole 1247B. gAPI = American Petroleum Institute gamma ray units, PEF = photoelectric effect factor.

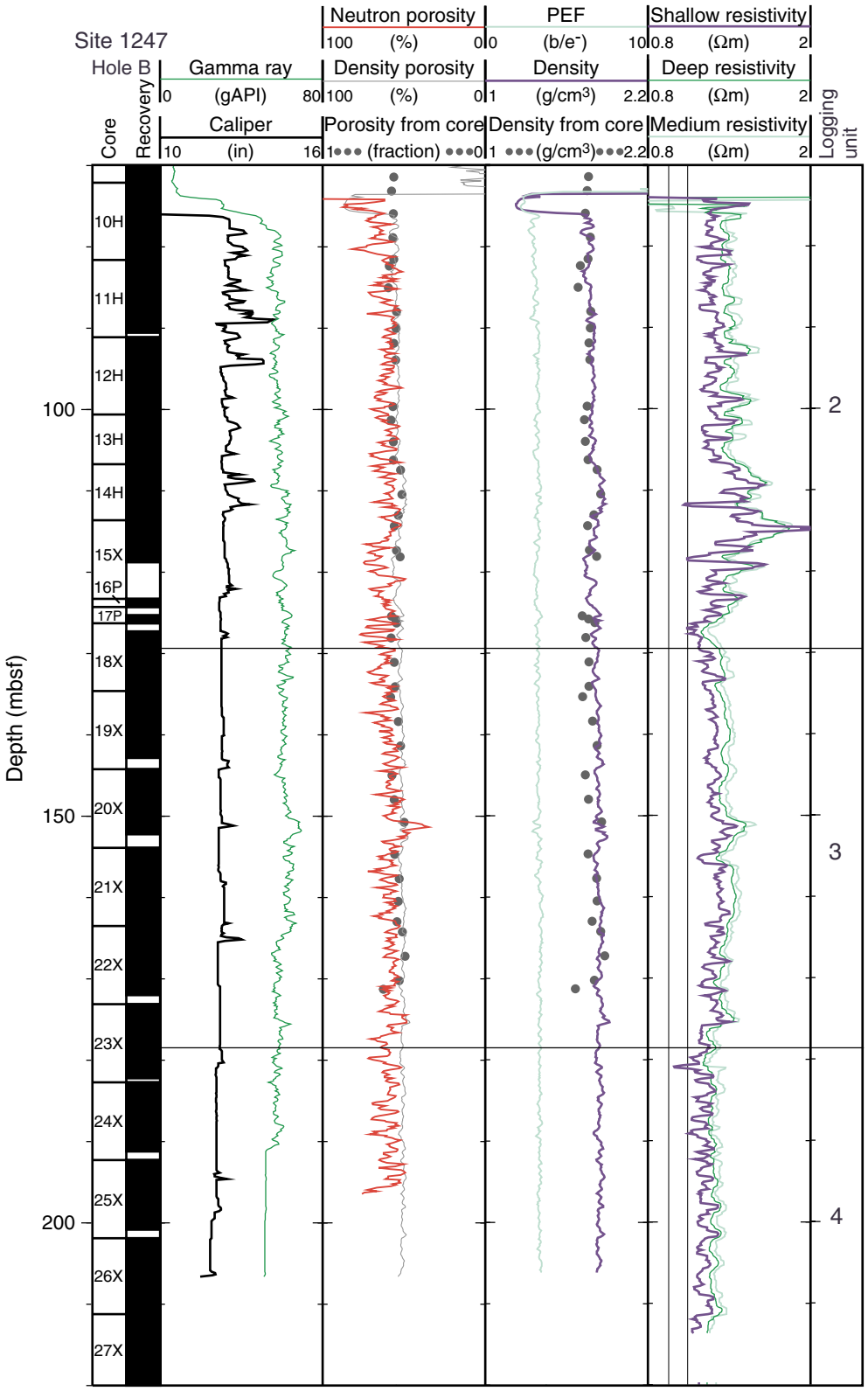

Figure F35. CWL gamma ray data from Hole 1247B. gAPI = American Petroleum Institute gamma ray units.

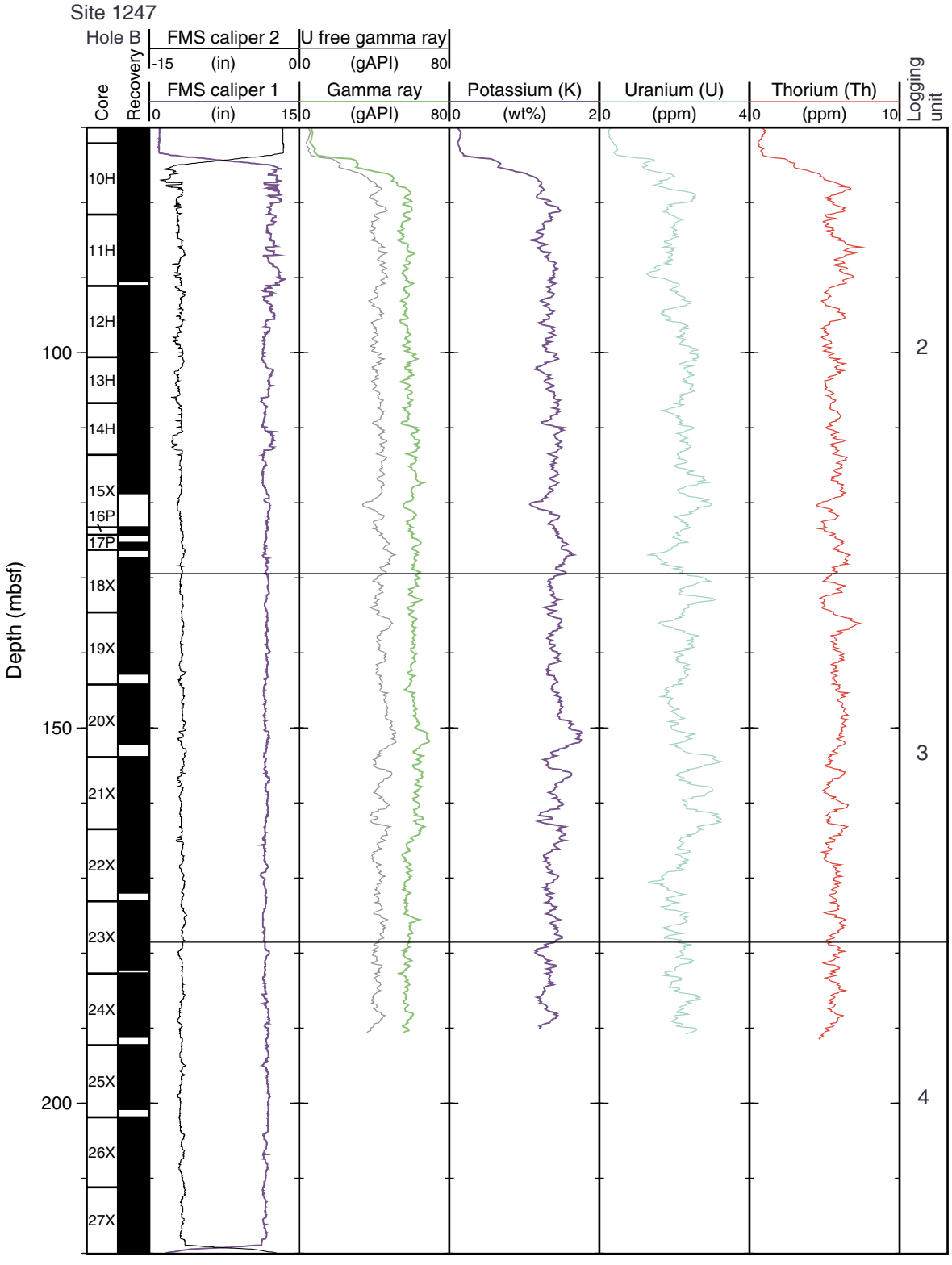

Figure F36. Comparison of LWD and CWL downhole logging data from Holes 1247A and 1247B. gAPI = American Petroleum Institute gamma ray units, por. = porosity, LWD = logging while drilling, PEF = photoelectric effect factor.

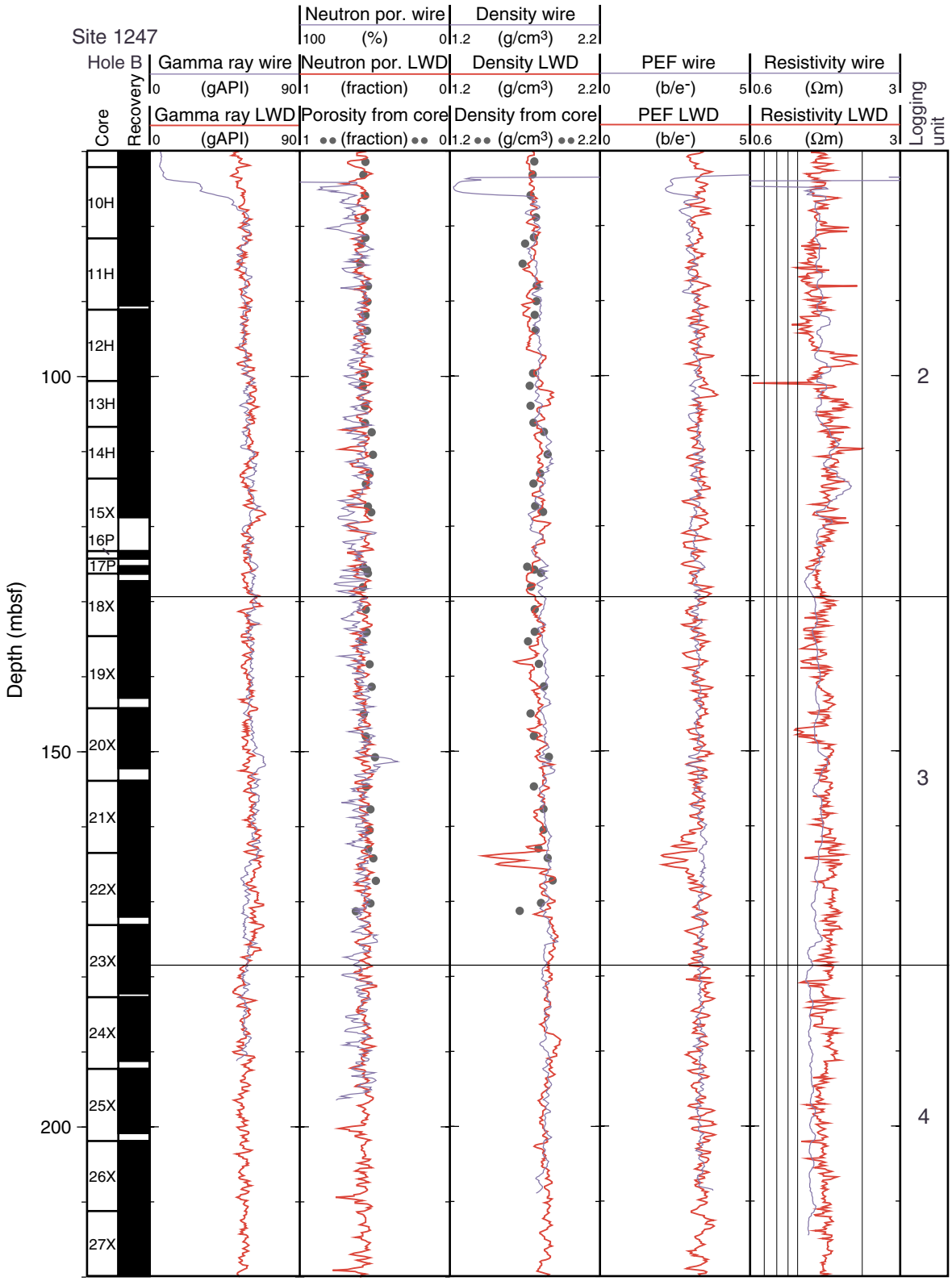

Figure F37. CWL acoustic logging data from Hole 1247B. The resistivity log is used as a reference indicator of the presence of gas hydrate. Low sonic waveform amplitudes are also possible indicators of gas hydrate. SPh. Foc. res. = spherically focused resistivity.

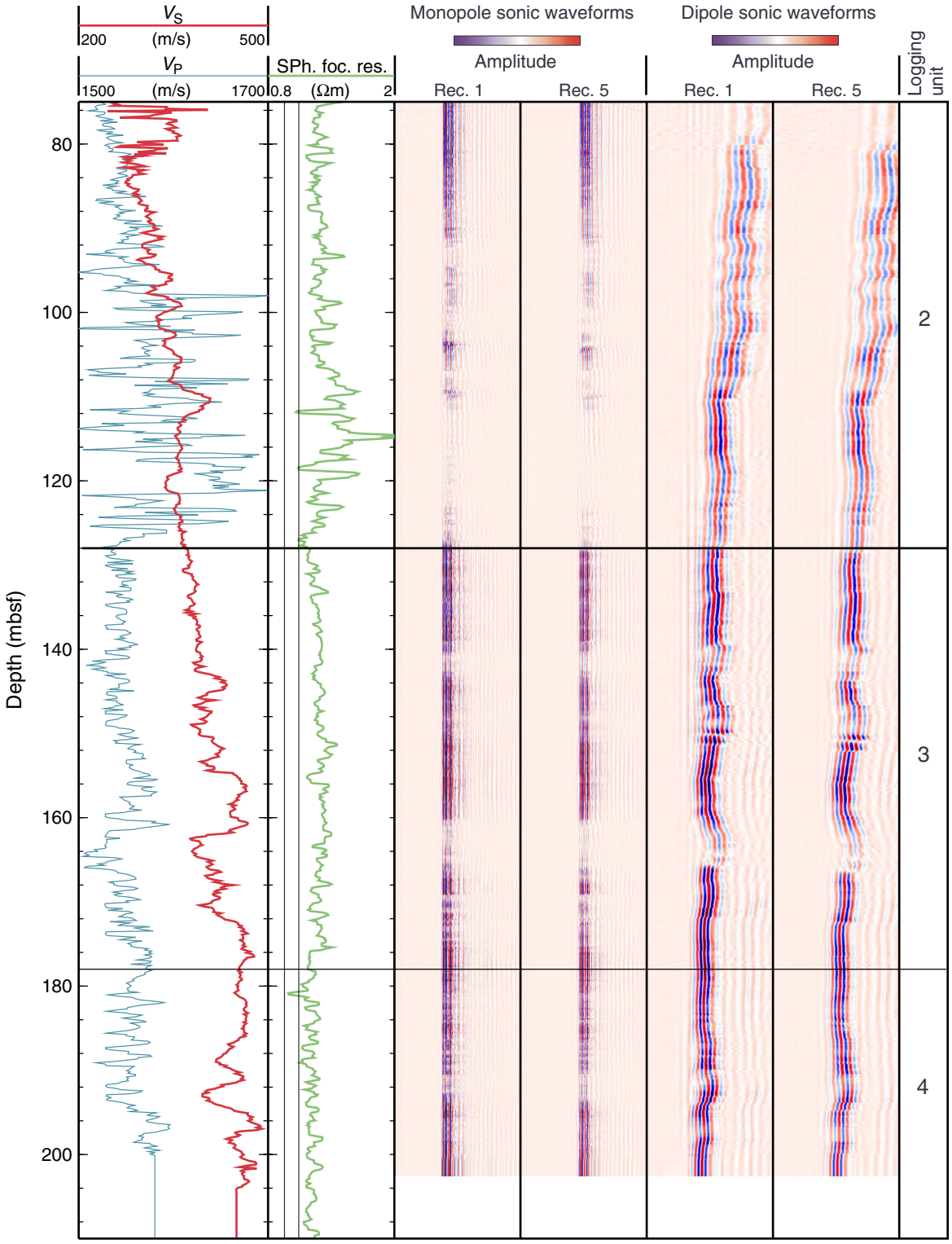

Figure F38. Resistivity-at-the-bit (RAB) and Formation Microscanner (FMS) images showing Horizon A, characterized by interbedded bright, resistive, and dark conductive layers.

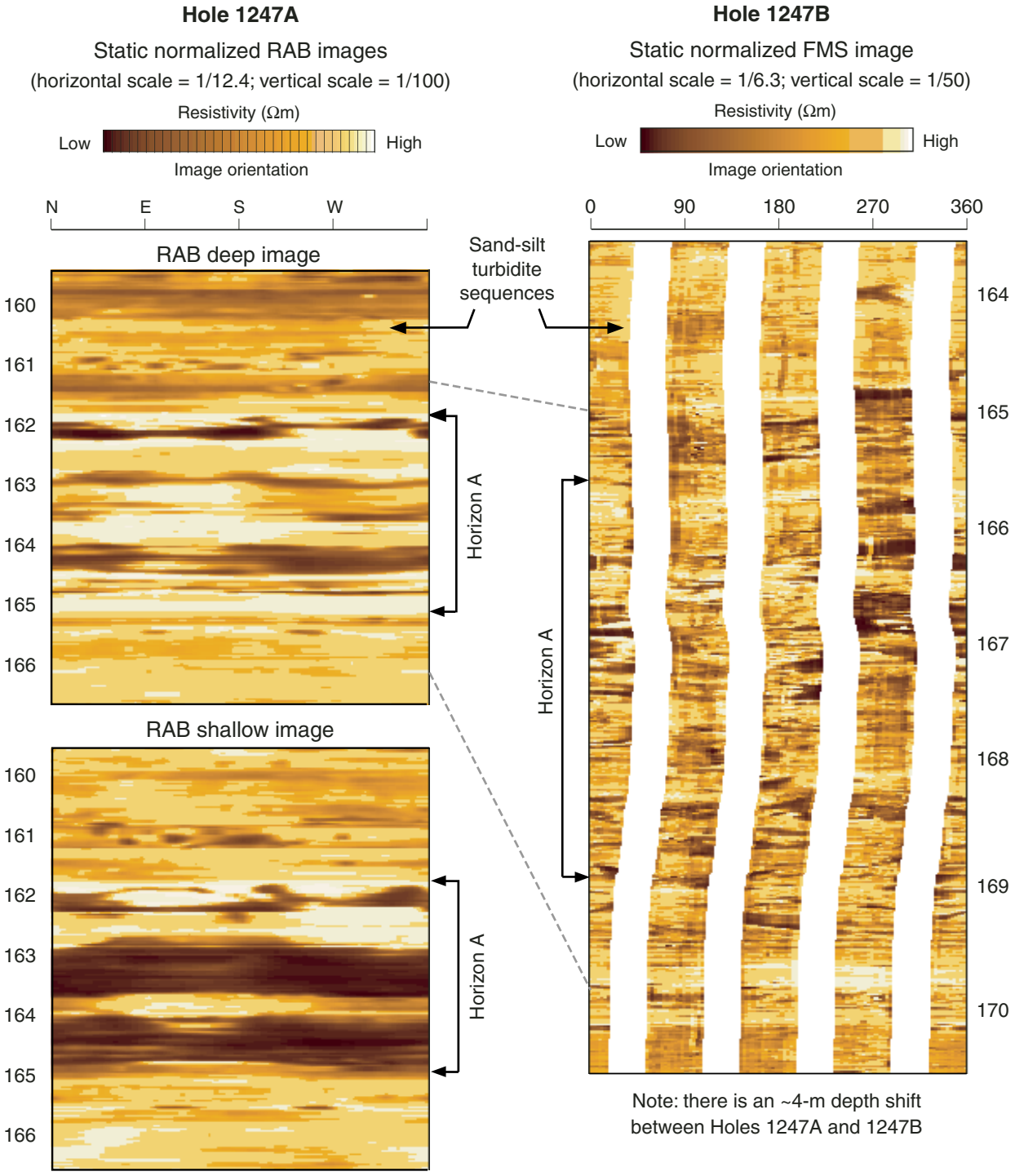

Figure F39. Comparison of LWD- (from Hole 1247A) and core-derived porosities (from Hole 1247B). NMR-MRP = Nuclear Magnetic Resonance tool, RAB = resistivity at the bit.

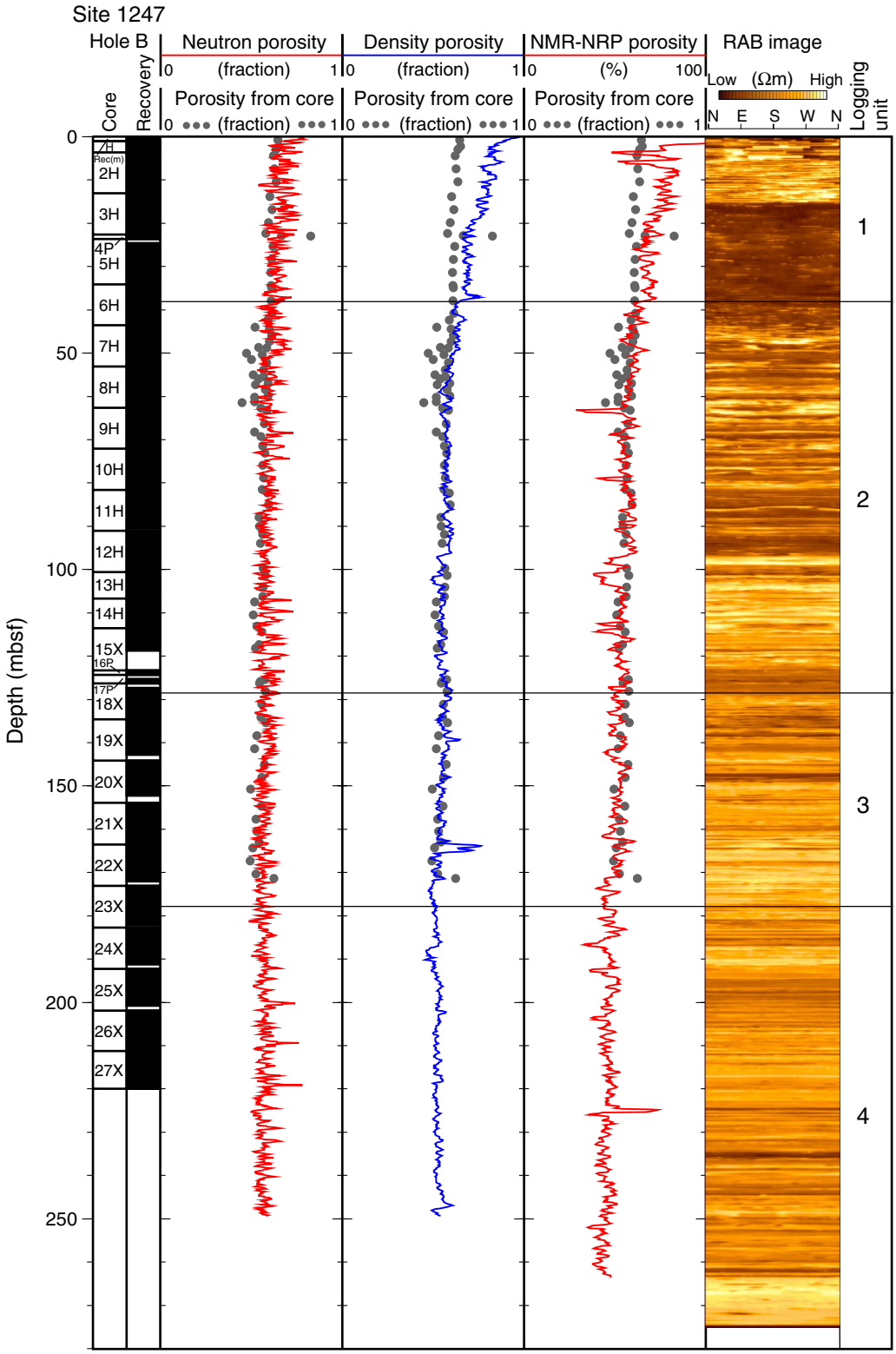

Figure F40. LWD-derived water saturations from Hole 1247A. gAPI = American Petroleum Institute gamma ray units, RAB = resistivity-at-the-bit.

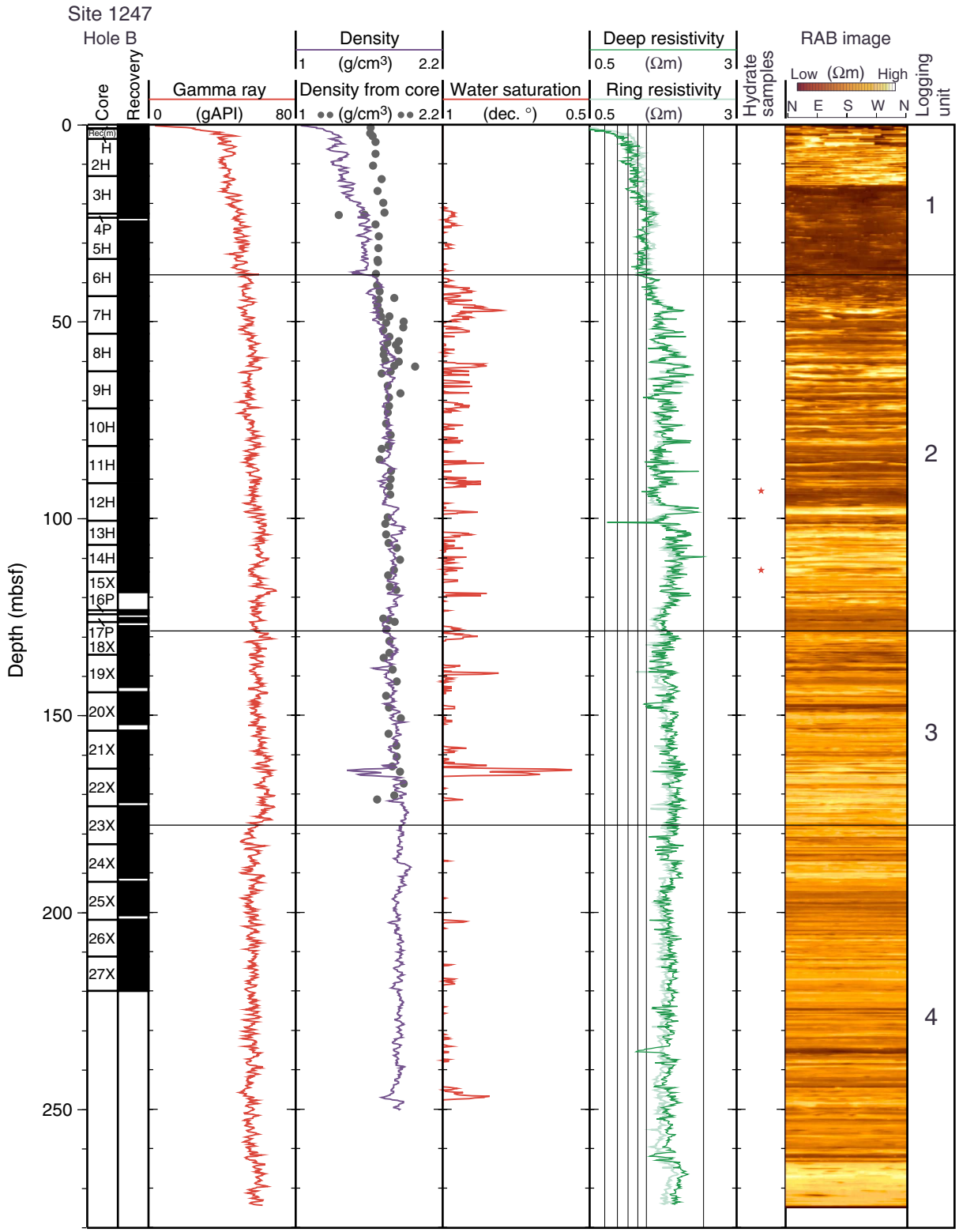

Figure F41. Borehole temperatures recorded with the TAP tool during the down and up pass of the three runs of the triple combo tool string in Hole 1247B. QSST = Inline Checkshot Tool.

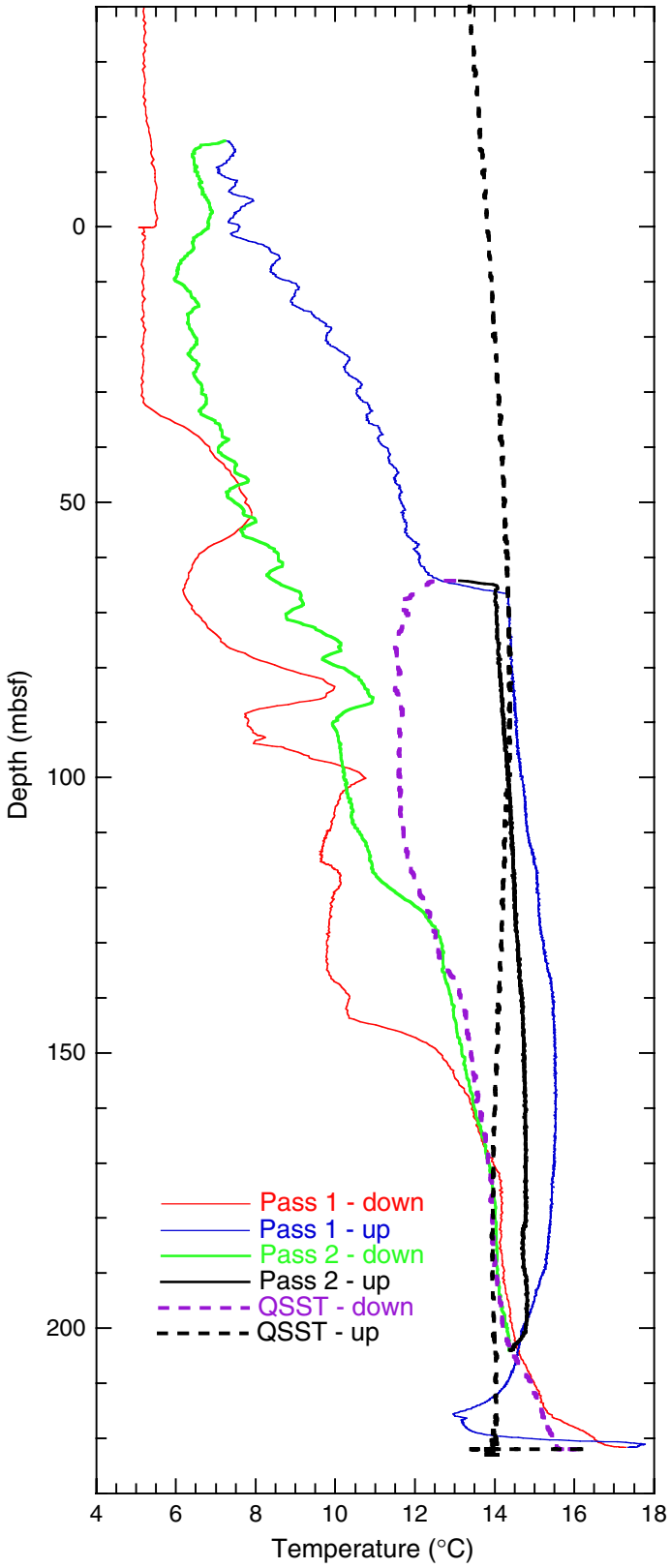

Table T1. Coring summary, Site 1247.

Hole 1247A
Latitude: 44°34.6591′N
Longitude: 125°9.0096′W
Time on site (hr): 81.75 (1800 hr, 19 Jul–1515 hr, 20 Jul 2002)
Time on hole (hr): 21.25 (1800 hr, 19 Jul–1515 hr, 20 Jul 2002)
Seafloor (drill pipe measurement from rig floor, mbrf): 845
Distance between rig floor and sea level (m): 10.9
Water depth (drill pipe measurement from sea level, m): 834.1
Total depth (drill pipe measurement from rig floor, mbrf): 1115
Total penetration (meters below seafloor, mbsf): 270
Total number of cores: 0
Total number of drilled intervals: 1
Total length of cored section (m): 0
Total core recovered (m): 0
Core recovery (%): 0

Hole 1247B
Latitude: 44°34.6589′N
Longitude: 125°9.0766′W
Time on hole (hr): 60.5 (0645 hr, 22 Aug–1915 hr, 24 Aug 2002)
Seafloor (drill pipe measurement from rig floor, mbrf): 845.9
Distance between rig floor and sea level (m): 11.1
Water depth (drill pipe measurement from sea level, m): 834.8
Total depth (drill pipe measurement from rig floor, mbrf): 1065.9
Total penetration (meters below seafloor, mbsf): 220
Total number of cores: 27
Total number of drilled intervals: 3
Total length of cored section (m): 217
Total core recovered (m): 212
Core recovery (%): 97.7

Core	Date (Aug 2002)	Local time (hr)	Depth (mbsf) Top	Depth (mbsf) Bottom	Length (m) Cored	Length (m) Recovered	Recovery (%)
204-1247A-							
			*****Drilled from 0 to 270 mbsf*****				
204-1247B-							
1H	22	1035	0.0	3.6	3.6	3.60	100.0
2H	22	1115	3.6	13.1	9.5	10.16	106.9
3H	22	1150	13.1	22.6	9.5	9.88	104.0
4P	22	1300	22.6	23.6	1.0	1.00	100.0
			*****Drilled from 23.6 to 24.6 mbsf*****				
5H	22	1350	24.6	34.1	9.5	10.47	110.2
6H	22	1420	34.1	43.6	9.5	10.32	108.6
7H	22	1505	43.6	53.1	9.5	9.53	100.3
8H	22	1550	53.1	62.6	9.5	10.03	105.6
9H	22	1645	62.6	72.1	9.5	9.71	102.2
10H	22	1715	72.1	81.6	9.5	9.85	103.7
11H	22	1845	81.6	91.1	9.5	8.94	94.1
12H	22	1915	91.1	100.6	9.5	9.40	98.9
13H	22	2015	100.6	106.7	6.1	6.17	101.1
14H	22	2055	106.7	113.6	6.9	6.93	100.4
15X	22	2240	113.6	123.3	9.7	5.18	53.4
16P	22	2325	123.3	124.3	1.0	1.00	100.0
			*****Drilled from 124.3 to 125.3 mbsf*****				
17P	23	0035	125.3	126.3	1.0	1.00	100.0
			*****Drilled from 126.3 to 127.3 mbsf*****				
18X	23	0120	127.3	134.6	7.3	8.74	119.7
19X	23	0230	134.6	144.2	9.6	8.25	85.9
20X	23	0435	144.2	153.9	9.7	8.02	82.7
21X	23	0535	153.9	163.5	9.6	9.74	101.5
22X	23	0635	163.5	173.1	9.6	8.52	88.8
23X	23	0725	173.1	182.7	9.6	9.11	94.9
24X	23	0815	182.7	192.3	9.6	8.83	92.0
25X	23	0910	192.3	201.9	9.6	8.51	88.6
26X	23	1100	201.9	211.2	9.3	9.67	104.0
27X	23	1145	211.2	220.0	8.8	9.42	107.0
				Cored totals:	217.0	211.98	97.7
				Drilled total:	3.0		
				Total:	220.0		

Table T2. Bioevents, Hole 1247B.

Age (Ma)	Bioevent	Top		Bottom		Average depth (mbsf)	Event number*	Comment
		Core, section, interval (cm)	Depth (mbsf)	Core, section, interval (cm)	Depth (mbsf)			
		204-1247B		204-1247B				
0.27	FO *Emiliania huxleyi*	5H-CC	35.02	6H-5, 36	40.46	37.74	1	Nannofossil
0.30	LO *Proboscia curvirostris*	5H-CC	35.02	6H-CC	44.47	39.70	2	Diatom
0.46	LO *Pseudoemiliania lacunosa*	8H-2, 47	55.07	8H-CC	63.08	59.08	3	Nannofossil
1.00	LO *Actinocyclus oculatus*	9H-CC	72.26	10H-CC	81.90	77.08	4	Diatom
1.00	LO small *Gephyrocapsa* spp. Acme	13H-CC	106.72	14H-1, 89	107.59	107.16	5	Nannofossil
1.20	FO small *Gephyrocapsa* spp. Acme	20X-6, 57	151.36	20X-CC	152.17	151.77	6	Nannofossil
1.59	FO *Calcydiscus macintyrei*	21X-CC	163.59	22X-CC	171.97	167.78	7	Nannofossil

Notes: * = number in Figure F11, p. 38. FO = first occurrence, LO = last occurrence.

Table T3. Interstitial water data, Hole 1247B.

Core, section, interval (cm)	Depth (mbsf)	pH	Alkalinity (mM)	Salinity (g/kg)	Cl (mM)	SO_4 (mM)	NH_4 (mM)	PO_4 (µM)	Na (mM)	K (mM)	Mg (mM)	Ca (mM)	B (µM)	Ba (µM)	Fe (µM)	Li (µM)	Mn (µM)	Sr (µM)	DOC (mM)
204-1247B-																			
1H-1, 140–150	1.40	7.27	3.75	35	545	29.2	0.1	4	489	12.0	48.9	10.0	563	6.3	8.1	28.3	0.26	90.7	1.11
1H-2, 90–100	2.40	7.23	3.60	35	547	27.8	0.1	21	492	12.0	49.1	9.7	568	6.7	8.3	28.2	0.19	91.9	—
2H-1, 140–150	5.00	7.48	5.61	35	547	26.5	0.4	15	500	12.1	48.9	9.4	553	6.3	8.9	27.1	0.07	89.7	—
2H-2, 140–150	6.50	7.39	10.49	35	550	23.3	0.9	71	488	11.9	47.1	8.3	596	5.3	6.3	23.8	0.02	87.7	—
2H-3, 140–150	8.00	7.38	18.02	34	545	15.2	1.4	115	487	11.7	46.9	6.4	588	3.0	9.4	21.4	0.09	83.5	—
2H-4, 140–150	9.50	7.59	29.34	34	551	6.8	2.0	132	495	11.9	44.4	4.7	663	7.0	7.0	19.4	0.04	80.9	—
2H-5, 140–150	11.00	7.41	38.07	34	551	1.6	—	165	489	11.4	42.8	4.1	622	34.3	3.7	18.1	0.00	81.3	6.26
2H-6, 140–150	12.50	7.37	39.60	34	551	1.1	—	181	491	11.6	44.9	3.4	679	50.8	3.9	17.0	0.03	83.5	—
2H-7, 77–78	13.37	7.61	41.32	34	556	0.8	—	214	496	11.6	43.3	3.2	673	65.4	6.1	16.9	0.12	86.9	—
3H-1, 140–150	14.50	7.51	41.96	34	556	0.3	2.6	238	496	11.6	43.5	3.0	714	71.8	3.3	16.3	0.09	86.2	—
3H-2, 140–150	16.00	7.37	44.11	34	555	0.2	3.1	298	498	11.8	44.0	2.8	731	78.7	5.0	16.4	0.16	88.4	—
3H-4, 140–150	19.00	7.41	47.98	34	553	0.5	4.7	304	498	11.8	43.8	2.9	737	84.3	12.4	15.4	0.25	87.0	11.28
4P-1, 20–30	22.80	—	—	—	551	—	—	—	—	—	—	—	—	—	—	—	—	—	—
5H-2, 140–150	27.50	7.38	56.02	34	—	0.6	5.6	231	509	12.5	44.6	3.0	787	105.0	17.5	19.6	1.35	92.8	—
5H-5, 140–150	32.00	7.27	58.78	35	551	0.9	5.9	250	515	12.4	45.4	3.0	839	113.6	24.4	19.6	1.56	94.3	13.78
6H-2, 140–150	37.00	7.38	63.39	35	550	1.3	6.3	63	494	14.0	44.7	2.9	774	111.1	7.0	20.5	0.66	87.8	—
6H-5, 140–150	41.50	7.57	60.49	35	552	0.6	8.3	181	490	12.9	43.4	2.9	819	118.1	19.7	21.8	1.43	91.2	14.88
7H-2, 140–150	46.45	7.46	65.76	35	553	0.4	5.7	153	487	13.2	43.8	2.9	868	136.2	11.0	22.7	1.58	97.5	—
7H-5, 140–150	50.95	7.37	63.94	35	554	0.9	6.5	118	489	12.9	41.9	2.8	818	131.0	11.1	23.2	1.01	95.0	12.67
8H-2, 140–150	56.00	7.32	63.08	34	549	1.8	8.2	166	488	12.7	40.0	2.6	875	138.7	9.2	25.7	0.78	95.8	—
8H-5, 140–150	60.50	7.42	66.25	35	553	0.6	7.3	108	505	14.1	40.2	2.6	862	149.4	5.9	29.4	0.56	94.7	13.34
9H-2, 140–150	65.41	7.40	58.55	35	554	0.9	9.5	181	492	13.1	42.0	2.7	810	138.9	7.0	32.0	0.75	96.4	—
9H-5, 140–150	69.91	7.51	61.01	35	554	0.8	7.7	153	487	13.3	38.5	2.2	792	134.7	5.6	33.3	0.33	89.8	15.19
10H-2, 140–150	75.00	7.57	63.69	35	558	1.0	7.8	212	493	12.9	39.5	2.5	820	147.2	7.4	36.3	0.51	95.7	—
10H-5, 140–150	79.50	7.25	58.29	34	551	0.8	7.5	191	485	12.8	39.5	2.8	867	137.4	5.9	36.0	0.43	98.1	15.03
11H-2, 140–150	84.11	7.46	63.94	35	560	0.4	9.3	195	493	12.6	38.1	2.9	858	152.0	9.5	35.3	0.45	105.1	—
11H-5, 140–150	88.61	7.28	62.49	35	556	0.2	6.9	216	495	13.2	38.1	3.0	878	150.8	8.3	35.2	0.47	102.4	15.08
12H-3, 140–150	94.51	7.35	64.14	35	556	1.3	9.5	116	494	14.1	37.7	3.1	844	137.1	4.3	36.5	0.55	98.4	—
12H-5, 140–150	97.51	7.67	63.01	35	549	0.5	10.1	83	492	14.6	36.3	2.9	653	143.2	4.2	35.5	0.42	94.0	16.89
13H-2, 140–150	103.13	7.41	63.30	35	550	1.4	9.9	135	488	12.9	37.4	3.5	766	128.1	6.0	36.2	0.82	100.4	—
13H-3, 140–150	104.63	7.57	62.26	35	549	1.1	10.4	26	487	13.6			695	105.5	5.5	35.8	0.82	87.5	16.92
14H-2, 140–150	109.60	7.46	61.63	35	552	1.7	9.6	87	493	13.7	35.1	3.4	701	152.6	3.5	37.0	0.30	98.4	—
14H-5, 62–83	113.32	7.59	51.20	32	515	4.2	8.7	93	456	12.6	33.8	3.2	641	91.4	4.7	34.2	0.48	81.7	16.45
15X-1, 135–150	114.95	7.35	63.36	34	542	2.0	10.6	178	488	12.9	35.3	3.8	814	152.6	4.6	37.9	1.04	100.4	—
15X-2, 135–150	116.45	7.55	60.41	32	506	1.6	8.7	176	455	12.4	31.8	3.4	790	130.5	4.2	34.3	0.63	87.6	16.27
17P-1, 20–30	125.50	—	—	—	—	—	—	—	—	—	—	—	—	—	—	—	—	—	—
18X-2, 135–150	130.15	7.30	66.39	35	542	1.0	9.4	195	494	12.2	34.6	4.1	842	200.9	10.2	37.6	1.94	100.5	—
18X-5, 135–150	134.65	7.33	63.39	35	545	1.0	8.1	184	490	12.0	34.7	3.8	879	197.6	8.0	39.3	1.28	96.3	14.66
19X-2, 127–147	137.37	7.36	61.20	33	544	1.5	11.9	119	490	12.3	32.1	3.7	758	167.9	5.1	41.4	1.26	88.6	—
19X-5, 130–150	141.87	7.15	61.66	35	540	0.7	9.8	164	485	11.8	32.5	3.5	798	200.9	10.0	46.2	1.39	91.6	13.92
20X-3, 130–150	148.50	7.22	58.55	34	538	1.5	12.7	146	482	11.6	32.6	3.5	731	118.1	9.7	48.1	0.85	82.5	15.55
21X-3, 130–150	158.20	7.22	56.09	34	538	0.6	13.1	123	493	12.1	28.4	2.9	726	143.2	3.5	50.6	0.65	81.6	12.77
22X-3, 130–150	167.80	7.26	54.24	34	543	2.3	14.4	191	495	11.4	27.8	2.7	746	122.7	5.2	46.4	0.67	83.5	16.72
23X-3, 130–150	177.40	7.33	52.14	34	544	1.5	14.5	179	500	11.7	27.6	2.6	676	108.4	8.8	44.2	0.53	82.0	17.06
24X-3, 130–150	187.00	7.30	54.50	34	547	0.8	14.3	176	492	12.0	28.2	2.8	709	124.4	5.8	47.0	0.46	82.9	18.85
25X-3, 130–150	196.33	7.35	55.91	34	546	1.3	14.8	161	499	11.5	28.3	2.8	655	109.4	9.9	50.1	0.49	80.8	17.41
26X-3, 130–150	206.20	7.29	56.43	35	546	0.8	16.6	135	501	11.6	28.3	2.8	616	112.5	10.5	53.9	1.43	80.9	19.01
27X-3, 130–150	215.50	7.32	57.70	35	545	0.8	16.7	160	498	11.6	29.6	2.2	568	103.5	6.3	55.4	0.88	82.0	18.62

Notes: DOC = dissolved organic carbon. — = no sample was available.

Table T4 Concentrations of methane, ethane, ethylene, and propane in headspace gas, Hole 1247B.

Core, section, interval (cm)	Depth (mbsf)	C_1 (ppmv)	C_2 (ppmv)	$C_{2=}$ (ppmv)	C_3 (ppmv)	C_1/C_2	C_1 (mM)
204-1247B-							
1H-1, 0–5	0.0	10					0.002
1H-2, 0–5	1.5	4					0.001
1H-3, 0–5	2.5	5					0.001
2H-1, 0–5	3.6	14					0.002
2H-2, 0–5	5.1	9					0.001
2H-3, 0–5	6.6	25					0.003
2H-4, 0–5	8.1	101					0.02
2H-5, 0–5	9.6	749					0.10
2H-6, 0–5	11.1	12,599	1.0			13,124	1.8
2H-7, 0–5	12.6	54,113	2.4			22,547	8.1
3H-1, 0–5	13.1	30,788	2.4			12,991	4.7
3H-2, 0–5	14.6	57,772	1.8			32,096	10.3
3H-3, 0–5	16.1	47,376	1.5	0.7		31,168	8.9
3H-4, 0–5	17.6	50,259	1.5	0.8		32,849	10.0
3H-5, 0–5	19.1	52,600	1.5	0.7		34,834	10.2
5H-4, 0–5	29.1	25,736	3.5		4.4	7,353	5.7
6H-3, 0–5	37.1	19,605	1.3	0.8		15,560	4.2
8H-3, 0–5	56.1	14,661	0.9			16,111	3.5
9H-3, 0–5	65.5	10,217	2.1	1.2		4,912	1.9
10H-3, 0–5	75.1	18,695	1.7	1.4	4.2	10,933	4.4
11H-3, 0–5	84.2	9,996	1.3	0.9		7,871	2.7
12H-4, 0–5	94.6	11,776	6.8	1.3	8.3	1,722	3.0
13H-3, 0–5	103.2	7,418	2.0	1.5	6.0	3,636	1.8
14H-3, 0–5	109.7	12,242	2.3	1.3	7.3	5,346	2.8
18X-3, 0–5	130.3	9,926	41.0	1.1	15.4	242	2.4
19X-2, 0–5	136.1	10,426	74.2	1.7		140	2.8
20X-2, 0–5	145.7	10,182	104.1	1.3	62.3	98	2.8
21X-2, 0–5	155.4	20,759	411.6	1.7	385.7	50	3.3
22X-2, 0–5	165.0	54,113	615.7	3.6	735.3	88	8.6
23X-2, 0–5	174.6	21,416	556.4	3.3	99.3	38	3.2
24X-2, 0–5	184.2	13,017	398.6	1.5	630.6	33	2.2
25X-2, 0–5	193.5	12,945	355.0	2.2	567.9	36	2.6
26X-4, 0–5	206.4	12,273	248.0	1.1	26.4	49	2.6
26X-6, 0–5	209.4	14,201	269.0		272.0	53	2.7
27X-4, 0–5	215.7	9,103	176.0	1.1	178.6	52	2.5
27X-6, 0–5	218.7	16,322	223.5	1.2	205.6	73	3.7

Note: C_1 = methane, C_2 = ethane, $C_{2=}$ = ethylene, C_3 = propane.

Table T5. Concentration of light hydrocarbon and nonhydrocarbon gases in VAC samples of core gas void, Hole 1247B.

Core, section, interval (cm)	Depth (mbsf)	C_1 (ppmv)	C_2 (ppmv)	C_3 (ppmv)	*i*-C_4 (ppmv)	*n*-C_4 (ppmv)	*i*-C_5 (ppmv)	*n*-C_5 (ppmv)	*i*-C_6 (ppmv)	*n*-C_6 (ppmv)	CO_2 (ppmv)	O_2 (ppmv)	N_2 (ppmv)	C_1/C_2
204-1247B-														
5H-1, 62	25.2	935,119	9.9	6.4							24,650	1,294	11,783	94,171
5H-2, 127	27.4	949,942	9.9	6.7							18,571	46,217	177,370	96,441
5H-3, 75	28.4	948,297	9.8	6.6							15,347	3,171	15,378	96,864
5H-7, 8	33.7	947,240	9.6	6.4							16,959	2,363	9,769	98,466
6H-1, 34	34.4	779,669	9.1	5.8							24,483	37,746	146,321	86,056
6H-1, 119	35.3	942,052	10.0	6.7							21,559	1,794	8,986	94,299
6H-3, 71	37.8	945,397	10.4	6.7							18,504	1,534	7,697	90,729
6H-6, 112	42.7	956,072	10.3	7.4							12,437	1,987	7,231	92,913
6H-7, 46	43.6	911,245	10.9	7.9							40,802	5,098	16,236	83,447
7H-1, 42	44.0	933,512	18.4	6.4							16,398	3,842	30,778	50,707
7H-2, 88	46.0	938,046	12.0	6.7							12,587	2,587	27,995	78,301
7H-4, 64	48.7	950,633	36.4								3,974	2,975	14,842	26,095
7H-5, 136	51.0	858,885	21.6	5.2							8,803	29,939	116,426	39,837
7H-6, 82	50.9	897,460	21.9	6.0							26,985	9,121	37,083	40,943
8H-1, 71	53.8	931,979	12.7	6.9										73,269
8H-2, 137	56.0	958,533	37.8								5,467	1,492	5,492	25,371
8H-3, 130	57.4	723,401	16.2	4.4							5,121	54,890	208,990	44,737
8H-4, 117	58.8	954,199	17.1	7.5							15,680	1,387	2,058	55,801
9H-1, 85	63.5	940,069	13.3	7.3							12,564	2,749	21,912	70,735
9H-2, 46	64.5	932,275	13.4	6.8							10,538	3,138	30,079	69,521
9H-3, 124	66.8	909,269	13.2	6.6										68,728
9H-6, 66	70.8	922,259	13.4								9,023	1,631	27,440	68,774
10H-1, 74	72.8	717,014	13.2	7.4							17,115	52,990	201,520	54,360
10H-2, 46	74.1	949,423	20.0	7.0							9,195	2,110	12,175	47,542
10H-4, 87	77.5	963,372	20.2	7.4										47,786
10H-5, 61	78.7	949,914	15.4	9.0										61,723
10H-6, 58	80.2	935,932	18.8	9.2										49,731
11H-1, 54	82.1	751,951	31.4	3.8							7,495	49,276	182,018	23,947
11H-2, 50	83.2	956,510	44.1	1.8							4,656	1,168	1,264	21,709
11H-3, 13	84.3	957,968	36.6	4.5							7,544	1,575	1,309	26,160
11H-4, 63	86.3	957,607	36.4	4.5							6,674	1,404	1,194	26,293
11H-6, 31	89.0	951,332	19.4	10.0							10,679	3,641	8,299	49,012
12H-1, 143	92.5	964,178	42.4								6,138	479	707	22,724
12H-2, 0	92.6	960,224	40.3								4,835	850	843	23,815
12H-2, 50	93.1	631,173	25.6	5.8							4,577	76,628	284,220	24,626
12H-4, 127	95.9	959,934	19.4	13.0							13,834	809	1,015	49,558
13H-2, 15	101.9	914,074	46.8	11.1							20,324	7,640	2,951	19,540
13H-4, 13	104.9	892,438	41.6	12.1							21,517	12,048	46,265	21,479
13H-5, 11	105.8	547,909	17.7								21,843	88,830	333,261	31,025
14H-1, 24	106.9	727,138	29.8	23.1							21,502	51,974	192,765	24,433
14H-4, 105	112.3	962,652	29.5	28.2			1.1	2.0			11,666	1,815	1,465	32,632
15X-1, 45	114.1	951,851	82.2	29.5				1.3			21,636	1,673	2,403	11,580
15X-2, 116	116.3	907,703	82.6	32.7				1.9			35,366	8,161	23,323	10,989
15X-3, 7	116.7	944,281	84.4	34.5				1.9			27,443	2,683	2,283	11,186
15X-3, 88	117.5	637,563	60.6	25.2				1.8			15,189	71,459	264,558	10,514
19X-1, 129	135.9	957,623	1,134.0	140.0		5.6	2.6				22,654	1,053	1,097	844
19X-2, 78	136.9	952,519	1,114.0	137.0	5.0		2.6				13,002	1,451	1,259	855
20X-1, 105	145.3	931,509	1,841.0	331.0	37.8	15.7	6.7				23,800	1,614	9,397	506
20X-2, 115	146.9	944,879	1,996.0	382.5	40.6	15.7	6.5				21,619	1,837	10,082	473
20X-3, 30	147.5	900,606	1,829.0	364.0	39.0	14.5	5.9				21,140	14,061	56,640	492
20X-4, 88	149.6	932,452	2,090.0	459.0	57.6	21.7	7.9				18,609	2,042	10,728	446
23X-1, 18	173.3	644,653	7,571.0	19,504.0	2,466.3	485.8	112.1				11,975	60,357	230,938	85
24X-4, 140	188.6	916,155	6,765.0	7,974.0	1,395.0	684.0	239.0	7.3	0.8		31,432	6,317	19,866	135
24X-5, 140	190.1	897,174	6,318.0	5,435.0	1,040.0	657.0	254.0	7.9	6.6	5.1	37,411	5,893	18,203	142
25X-3, 102	196.1	965,656	4,329.0	2,248.0	323.5	288.7	134.1	15.1	4.2		11,731	1,176	1,101	223
25X-4, 97	197.5	954,846	4,158.0	2,209.0	387.1	349.1	159.4	20.2	3.4		12,226	2,381	1,788	230
27X-1, 42	211.6	538,117	2,583.0	1,184.0	103.9	225.6	114.7	43.8			18,507	91,684	345,246	208

Note: C_1 = methane, C_2 = ethane, C_3 = propane, *i*-C_4 = isobutane, *n*-C_4 = normal butane, *i*-C_5 = isopentane, *n*-C_5 = normal pentane, *i*-C_6 = isohexane, *n*-C_6 = normal hexane, CO_2 = carbon dioxide, O_2 = oxygen, N_2 = nitrogen.

Table T6. Composition of gas from analyses of decomposed samples of gas hydrate, Hole 1247B.

Core, section, interval (cm)	Depth (mbsf)	C_1 (ppmv)	C_2 (ppmv)	C_3 (ppmv)	*i*-C_4 (ppmv)	*n*-C_4 (ppmv)	CO_2 (ppmv)	O_2 (ppmv)	N_2 (ppmv)	C_1/C_2
204-1247B-										
12H-2, 41–51	93.01	952,222	39.43		NA	NA	NA	NA	NA	24,150
12H-2, 41–51	93.01	957,557	38.53				3519	1667	1506	24,852

Note: C_1 = methane, C_2 = ethane, C_3 = propane, *i*-C_4 = isobutane, *n*-C_4 = normal butane, CO_2 = carbon dioxide, O_2 = oxygen, N_2 = nitrogen. NA = not analyzed. Blank cells = below detection limit.

Table T7. Composition of gas samples from PCS experiments, Hole 1247B.

Sample	Volume (mL)	C_1 (ppm)	C_2 (ppm)	C_3 (ppm)	*i*-C_4 (ppm)	*n*-C_4 (ppm)	*i*-C_5 (ppm)	*n*-C_5 (ppm)	O_2 (ppm)	N_2 (ppm)	CO_2 (ppm)	C_1/C_2
204-1247B-4P (22.6 mbsf)												
G1	195	460,317	7.6	4.9					51,941	471,251	5,255	60,728
204-1247B-16P (123.3 mbsf)												
G1	90	496,730	128.5	9.9		5.7	2.2	17.9	49,524	333,285	159	2,396
G2	245	891,178	345.0	24.6	7.3				8,230	91,030	358	
G3	240	915,366	381.6	24.9					1,408	56,990	288	
G4	450	920,808	367.8	25.5					1,511	58,910	189	
G5	420	927,056	389.4	26.3					2,653	46,396	176	
G6	315	932,118	393.4	30.0					984	42,328	165	
G7	510	926,830	378.3	27.2					1,077	4,999	170	
G8	495	910,966	341.8	27.2					1,392	65,902	187	
G9	480	927,421	364.7	28.4					1,148	47,641	220	
G10	330	916,396	351.3	30.3					3,699	56,933	267	
G11	345	923,908	358.3	28.9					2,316	50,860	303	
G12	465	935,760	372.1	30.5					972	37,564	305	
G13	550	935,567	376.1	30.8					7,457	60,227	421	
G14	490	937,119	418.2	33.6					993	35,552	745	
G15	250	933,606	448.1	33.8					2,880	40,652	1,211	
G16	120	933,260	438.9	40.6					2,228	36,009	1,423	
G17	140	936,946	454.2	39.2					2,154	33,852	1,572	
G18	90	931,460	468.3	42.7					1,895	35,805	1,370	

Notes: C_1 = methane, C_2 = ethane, C_3 = propane, *i*-C_4 = isobutane, *n*-C_4 = normal butane, *i*-C_5 = isopentane, *n*-C_5 = normal pentane, O_2 = oxygen, N_2 = nitrogen, CO_2 = carbon dioxide. C_1/C_2 ratio reported corresponds to the integrated value for the entire pressure core.

Table T8. Carbonate carbon, calcium carbonate, total carbon, organic carbon, total nitrogen, and total sulfur contents and C/N ratios, Hole 1247B.

Core, section, interval (cm)	Depth (mbsf)	Carbonate carbon (wt%)	$CaCO_3$ (wt%)	Total carbon (wt%)	Organic carbon (wt%)	Total nitrogen (wt%)	Total sulfur (wt%)	C/N
204-1247B-								
1H-3, 42–43	2.92	0.48	3.99	1.51	1.03	0.14	0.49	7.36
2H-3, 76–77	7.36	0.27	2.24	1.24	0.97	0.11	1.07	8.82
3H-3, 76–77	16.86	0.52	4.32	1.77	1.25	0.17	0.66	7.35
5H-3, 76–77	28.36	0.48	3.96	1.78	1.30	0.16	1.00	8.13
6H-3, 75–76	37.85	0.29	2.39	1.56	1.27	0.17	0.42	7.47
7H-3, 75–76	47.30	0.44	3.67	1.92	1.48	0.19	0.72	7.79
8H-3, 88–89	56.98	0.39	3.28	1.40	1.01	0.14	0.34	7.21
8H-3, 119–120	57.29	0.46	3.83	1.14	0.68	0.10	0.41	6.80
9H-3, 75–76	66.26	0.82	6.87	1.81	0.99	0.16	0.27	6.19
11H-3, 80–81	85.01	0.67	5.60	1.84	1.17	0.18	0.25	6.50
12H-3, 83–84	93.94	0.58	4.83	1.60	1.02	0.16	0.32	6.38
13H-3, 76–77	103.99	0.57	4.77	1.55	0.98	0.18	0.33	5.44
14H-3, 76–77	110.46	1.57	13.07	2.59	1.02	0.16	0.39	6.38
15X-3, 76–77	117.36	0.44	3.70	1.77	1.33	0.19	0.45	7.00
19X-3, 76–77	138.33	0.39	3.29	1.68	1.29	0.20	0.51	6.45
22X-3, 75–76	167.25	0.84	7.01	1.61	0.77	0.13	0.29	5.92
23X-3, 75–76	176.85	0.98	8.14	2.03	1.05	0.19	0.26	5.53
24X-3, 121–122	186.91	0.80	6.70	1.81	1.01	0.16	0.20	6.31
25X-3, 76–77	195.79	0.71	5.89	1.90	1.19	0.18	0.27	6.61
26X-3, 65–66	205.55	0.84	6.97	1.99	1.15	0.19	0.25	6.05
27X-3, 75–76	214.95	0.95	7.92	1.95	1.00	0.16	0.23	6.25

Note: $CaCO_3$ = calcium carbonate.

Table T9. Rock-Eval pyrolysis of samples, Hole 1247B.

Core, section, interval (cm)	Depth (mbsf)	Organic carbon (wt%)	S_1 (mg/g)	S_2 (mg/g)	Production index ($S_1/[S_1+S_2]$)	Hydrogen index (mg S_2/g C)	T_{max} (°C)
204-1247B-							
3H-3, 76–77	16.86	1.25	0.26	1.22	0.18	98	410
7H-3, 75–76	47.30	1.48	0.46	2.74	0.14	185	409
11H-3, 80–81	85.01	1.17	0.31	1.49	0.17	127	408
19X-3, 76–77	138.33	1.29	0.38	1.65	0.19	128	409
23X-3, 75–76	176.85	1.05	0.27	1.31	0.17	125	412
25X-3, 76–77	195.79	1.19	0.25	1.57	0.14	132	416
26X-3, 65–66	205.55	1.15	0.24	1.39	0.15	121	417

Note: S_1 and S_2 are as defined in **"Organic Matter Characterization",** p. 18, in "Organic Geochemistry" in the "Explanatory Notes" chapter.

Table T10. Presence of gas hydrate based on infrared images of cores in liners, Hole 1247B.

Core, section	ΔT (°C)	Gas hydrate texture*	Depth interval (mbsf)†		Anomaly designation‡	Hydrate sample		
			Top	Bottom		Top (cm)	Bottom (cm)	Depth (mbsf)
204-1247B-								
3H	–0.4	Disseminated	15.80	16.10	IR442			
3H	–0.3	Disseminated	16.80	17.10	IR443			
5H	–0.8	Disseminated	34.20	34.40	IR444			
6H	–0.4	Disseminated	34.30	34.40	IR445			
7H	–1.0	Disseminated	45.63	45.70	IR446			
7H	–0.7	Disseminated	45.80	45.90	IR447			
7H	–0.7	Disseminated	46.40	46.47	IR448			
7H	–0.3	Disseminated	47.78	47.93	IR449			
7H	–4.9	Vein; width includes fractures	46.45	46.70	IR450			
7H	–0.6	Vein; disseminated	50.30	50.70	IR451			
7H	–0.5	Disseminated	52.22	52.26	IR452			
8H	–0.4	Disseminated	53.10	53.50	IR453			
8H	–1.7	Vein	54.69	54.74	IR454			
8H	–0.3	Disseminated	55.25	55.29	IR455			
8H	–1.8	Nodular	56.16	56.25	IR456			
8H	–0.8	Disseminated; associated with fracture	56.80	56.98	IR457			
8H	–1.2	Nodular	57.20	57.23	IR458			
8H	–1.2	Disseminated; possible gas cooling	60.35	60.44	IR459			
8H	–0.2	Disseminated	61.06	61.14	IR460			
8H	–1.0	Vein	61.51	61.60	IR461			
8H	–0.5	Disseminated	61.95	62.25	IR462			
10H	–0.3	Disseminated	81.40	81.56	IR463			
11H	–1.5	Disseminated; includes gas voids	81.75	82.10	IR464			
11H	–1.5	Disseminated; some gas voids	82.55	82.90	IR465			
11H	–2.9	Disseminated	83.63	83.90	IR466			
11H	–1.4	Nodular	84.85	85.05	IR467			
11H	–1.8	Nodular	86.10	86.28	IR468			
11H	–1.7	Vein; disseminated	86.90	87.06	IR469			
11H	–0.3	Disseminated	89.51	89.60	IR470			
11H	–0.2	Disseminated	90.68	90.71	IR471			
12H	–0.6	Disseminated	91.68	91.73	IR472			
12H	–0.5	Disseminated; includes gas void	92.80	93.02	IR473			
12H-2	–4.3	Nodular	93.55	93.77	IR474	41	51	93.01
12H	–1.1	Vein	94.42	94.80	IR475			
12H	–0.4	Disseminated	95.60	95.71	IR476			
12H	–0.3	Disseminated	96.10	96.23	IR477			
12H	–0.4	Disseminated	96.62	96.71	IR478			
12H	–0.8	Nodular	97.45	97.70	IR479			
12H	–1.1	Disseminated	98.04	98.12	IR480			
13H	–1.0	Disseminated	102.87	103.01	IR481			
13H	–0.6	Disseminated	103.30	103.63	IR482			
13H	–1.3	Disseminated	105.19	105.31	IR483			
14H	–0.6	Disseminated	109.45	109.56	IR484			
14H	–1.5	Disseminated	110.49	110.63	IR485			
14H-5	–2.8	Disseminated	113.25	113.47	IR486	39	62	113.09
15X	–1.1	Disseminated; mottled; possibly cold core top	113.60	113.70	IR487			
15X	–0.9	Disseminated	115.68	116.00	IR488			
15X	–0.7	Disseminated; nodular	117.30	116.00	IR489			
15X	–0.7	Disseminated; nodular	117.30	117.40	IR489			
15X	–1.8	Nodular	117.48	117.48	IR490			

Notes: * = from anomaly characteristics and core description, if available. † = from uncut core liner. ‡ = Anomaly designations are used for reference to specific anomalies in text and figures. The difference between these depth intervals and the equivalent curated section depth intervals is typically <1 m.

Table T11. Moisture and density, Hole 1247B.

Core, section, interval (cm)	Depth (mbsf)	Density (g/cm^3)		Porosity (%)
		Bulk	Grain	
204-1247B-				
1H-1, 74–76	0.74	1.612	2.682	65
1H-2, 64–66	2.14	1.611	2.710	65
1H-3, 40–42	2.90	1.631	2.692	64
2H-1, 74–76	4.34	1.653	2.687	62
2H-3, 74–76	7.34	1.653	2.714	63
2H-5, 74–76	10.34	1.635	2.715	64
3H-1, 74–76	13.84	1.705	2.738	60
3H-3, 74–76	16.84	1.669	2.705	62
3H-5, 74–76	19.84	1.718	2.732	59
3H-7, 74–76	22.34	1.728	2.704	58
4P-1, 17–19	22.77	1.565	2.652	67
4P-1, 33–35	22.93	1.352	2.910	83
5H-1, 74–76	25.34	1.655	2.685	62
5H-3, 74–76	28.34	1.681	2.718	61
5H-5, 74–76	31.34	1.676	2.686	61
5H-7, 74–76	34.34	1.671	2.682	61
6H-1, 74–76	34.84	1.673	2.697	61
6H-3, 74–76	37.84	1.658	2.647	61
6H-5, 70–72	40.80	1.666	2.691	62
6H-6, 74–76	42.34	1.688	2.641	59
7H-1, 41–43	44.01	1.808	2.663	52
7H-1, 74–76	44.34	1.681	2.668	60
7H-2, 74–76	45.79	1.671	2.697	61
7H-3, 74–76	47.29	1.686	2.675	60
7H-4, 54–56	48.59	1.768	2.644	54
7H-4, 74–76	48.79	1.700	2.650	59
7H-5, 40–42	49.95	1.884	2.660	47
7H-5, 74–76	50.29	1.740	2.653	56
7H-6, 35–37	51.40	1.881	2.740	50
7H-6, 108–110	52.13	1.718	2.690	58
8H-1, 74–76	53.84	1.768	2.742	57
8H-2, 34–36	54.94	1.844	2.702	51
8H-2, 74–76	55.34	1.750	2.705	57
8H-2, 127–129	55.87	1.821	2.762	54
8H-3, 88–90	56.98	1.722	2.735	59
8H-3, 119–121	57.29	1.840	2.738	52
8H-4, 74–76	58.34	1.720	2.669	58
8H-5, 74–76	59.84	1.735	2.765	59
8H-5, 104–106	60.14	1.842	2.723	52
8H-6, 60–62	61.20	1.807	2.650	52
8H-6, 83–85	61.43	1.977	2.757	45
8H-7, 51–53	62.61	1.776	2.709	55
9H-1, 59–61	63.19	1.702	2.661	59
9H-3, 74–76	66.25	1.752	2.725	57
9H-4, 121–123	68.22	1.857	2.757	52
9H-5, 74–76	69.25	1.763	2.675	55
9H-7, 40–42	71.41	1.763	2.711	56
10H-1, 99–101	73.09	1.754	2.740	58
10H-3, 80–82	75.90	1.739	2.662	56
10H-5, 74–76	78.84	1.776	2.766	57
10H-7, 38–40	81.48	1.761	2.699	56
11H-1, 74–76	82.34	1.704	2.681	59
11H-3, 80–82	85.01	1.686	2.654	59
11H-5, 74–76	87.95	1.780	2.684	54
11H-7, 30–32	90.01	1.777	2.683	55
12H-1, 74–76	91.84	1.766	2.718	56
12H-3, 80–82	93.91	1.773	2.694	55
12H-7, 50–52	99.61	1.755	2.708	57
13H-1, 70–72	101.30	1.733	2.702	58
13H-3, 74–76	103.97	1.740	2.670	57
13H-5, 51–53	106.24	1.759	2.707	56
14H-1, 74–76	107.44	1.828	2.695	52
14H-3, 74–76	110.44	1.852	2.720	51
14H-5, 30–32	113.00	1.802	2.686	53
15X-1, 74–76	114.34	1.757	2.680	56
15X-3, 74–76	117.34	1.769	2.657	54
15X-4, 50–52	118.10	1.822	2.697	52
16P-1, 20–22	123.50	1.761	2.656	55
16P-1, 42–44	123.72	1.806	2.726	54
16P-1, 70–72	124.00	1.757	2.760	58
17P-1, 8–10	125.38	1.718	2.662	58
17P-1, 50–52	125.80	1.763	2.668	55
17P-1, 90–92	126.20	1.809	2.747	55
18X-1, 74–76	128.04	1.743	2.729	58
18X-3, 74–76	131.04	1.768	2.705	56
18X-5, 74–76	134.04	1.766	2.683	55
19X-1, 74–76	135.34	1.721	2.688	58
19X-3, 74–76	138.31	1.794	2.670	53
19X-5, 74–76	141.31	1.827	2.693	52
20X-1, 74–76	144.94	1.739	2.696	57
20X-3, 74–76	147.94	1.762	2.692	56
20X-5, 50–52	150.70	1.860	2.685	50
21X-1, 74–76	154.64	1.761	2.681	56
21X-3, 74–76	157.64	1.824	2.715	53
21X-5, 54–56	160.44	1.826	2.738	53
21X-7, 54–56	162.94	1.791	2.698	54
22X-1, 74–76	164.24	1.853	2.708	51
22X-3, 74–76	167.24	1.885	2.723	49
22X-5, 74–76	170.24	1.808	2.682	53
22X-6, 27–29	171.27	1.667	2.740	63
23X-1, 46–48	173.56	1.841	2.668	50
23X-1, 81–83	173.91	1.884	2.719	49
23X-1, 108–110	174.18	2.019	2.759	43
23X-3, 74–76	176.84	1.788	2.688	54
23X-5, 70–72	179.80	1.781	2.656	54
23X-6, 71–73	181.31	1.844	2.664	50
23X-6, 110–112	181.70	1.778	2.680	55
24X-1, 58–60	183.28	1.747	2.608	54
24X-3, 121–123	186.91	1.774	2.634	53
24X-4, 60–62	187.80	1.794	2.660	53
24X-5, 94–96	189.64	1.797	2.627	52
25X-1, 72–74	193.02	1.769	2.651	54
25X-3, 76–78	195.79	1.756	2.640	55
25X-4, 53–55	197.06	1.783	2.667	54
25X-6, 38–40	199.09	1.780	2.675	54
25X-7, 49–51	200.20	1.779	2.696	55
26X-1, 92–94	202.82	1.792	2.736	55
26X-3, 65–67	205.55	1.736	2.678	57
26X-5, 44–46	208.34	1.769	2.668	55
26X-6, 74–76	210.14	1.820	2.731	53
27X-1, 68–70	211.88	1.779	2.752	56
27X-3, 74–76	214.94	1.786	2.775	57
27X-5, 74–76	217.94	1.770	2.773	57

Table T12. Thermal conductivity, Hole 1247B.

Core, section, interval (cm)	Depth (mbsf)	Thermal conductivity (W/[m·K])	Individual measurements (W/[m·K])		
204-1247B-					
1H-3, 35	2.85	1.042	1.013	1.060	1.054
2H-3, 75	7.35	1.093	1.094	1.091	1.093
3H-3, 85	16.95	0.945	0.978	0.928	0.929
5H-1, 70	25.30	0.926	0.925	0.916	0.936
5H-3, 70	28.30	0.960	0.977	0.950	0.954
5H-5, 75	31.35	0.932	0.974	0.972	0.851
6H-3, 75	37.85	0.856	0.844	0.846	0.878
7H-1, 76	44.36	0.911	0.907	0.918	0.909
7H-3, 85	47.40	0.947	0.975	0.925	0.941
7H-5, 73	50.28	0.935	0.938	0.928	0.940
8H-3, 28	56.38	0.931	0.929	0.920	0.944
9H-1, 55	63.15	0.884	0.890	0.875	0.886
9H-3, 112	66.63	1.004	0.994	1.020	0.997
9H-5, 75	69.26	1.085	1.038	1.123	1.093
10H-3, 75	75.85	0.957	0.951	0.963	0.956
11H-1, 75	82.35	0.829	0.826	0.821	0.840
11H-3, 110	85.31	0.985	1.003	0.973	0.978
11H-5, 75	87.96	1.121	1.111	1.127	1.126
12H-3, 75	93.86	0.873	0.873	0.871	0.875
13H-1, 80	101.40	0.990	0.990	0.987	0.993
13H-3, 75	103.98	0.989	0.991	0.988	0.987
13H-5, 50	106.23	1.024	1.016	1.019	1.037
14H-3, 85	110.55	1.058	1.050	1.085	1.039
15X-3, 40	117.00	1.041	1.030	1.017	1.075
18X-3, 75	131.05	0.948	0.951	0.945	0.949
19X-1, 60	135.20	1.022	1.029	1.006	1.032
19X-3, 75	138.32	1.065	1.088	1.052	1.056
19X-6, 30	142.37	1.070	1.069	1.065	1.076
20X-3, 70	147.90	0.985	0.977	0.992	0.986
21X-3, 75	157.65	1.023	1.036	1.015	1.018
22X-3, 60	167.10	1.064	1.058	1.068	1.067
23X-3, 75	176.85	0.949	0.950	0.932	0.965
24X-3, 75	186.45	0.980	0.980	0.979	0.981
25X-1, 72	193.02	1.034	1.022	1.020	1.061
25X-3, 70	195.73	1.055	1.061	1.066	1.039
25X-5, 56	198.27	1.030	0.997	1.044	1.050
26X-3, 75	205.65	1.066	1.094	1.059	1.045
27X-3, 75	214.95	0.995	0.998	0.992	0.995

Table T13. Temperature measurements, Hole 1247B.

Core	Depth (mbsf)	Temperature (°C)	Thermal conductivity (W/[m·K])	Tool ID
204-1247B-				
1H	00.0	3.79	—	12
5H	34.1	5.52	0.93	11
7H	53.1	6.56	0.94	11
9H	72.1	7.43	1.09	11
11H	91.1	8.49	1.12	11
13H	106.7	9.43	1.02	11
19X–20X	144.2	5.75	—	2*
24X–25X	192.3	7.20	—	2*

Notes: Neither of the DVTP measurements were used for determining the temperature gradient at this site. ID = identification. * = not used for calculation of temperature gradients.

Table T14. Results from degassing experiments, Hole 1247B.

Core	Depth (m) Top	Depth (m) Bottom	Run time (min)	Total volume (mL)*	Volume (mL)† $O_2 + N_2$	Volume (mL)† C_1	Volume (mL)† CO_2	Volume (mL)† C_{2+}	Concentration (%)‡ $O_2 + N_2$	Concentration (%)‡ C_1	Concentration (%)‡ CO_2	Concentration (%)‡ C_{2+}	Core length (m)	Porosity (%)	C_1 (mM)**
204-1247B-															
4P	22.6	23.6	547	195	103.2	90.8	1.0	0.00	52.9	46.6	0.5	0.001	0.44–1.00	60	4.3–9.7
16P	123.3	124.3	3454	6025	339.7	5680.3	2.5	2.51	5.6	94.3	0.0	0.042	1.00	55	292.4

Notes: * = volume of gas released. † = volume of components released. ‡ = percent of components in released gas. ** = calculated concentration in situ. Core length is reported as measured after the core was degassed and split (I.e., curated length) and as cored in subsurface.

Table T15. Conventional wireline logging operations summary, Hole 1247B.

Date (Aug 2002)	Local time (hr)	Tool depth (mbsf)	Remarks
23	1145		Last core on deck
23	1145–1415		Wiper trip up to 80 mbsf; back down to 220 mbsf
23	1415–1430		Hole displaced with sepiolite mud
23	1430–1530		Set back top drive; bottom of pipe put at 90 mbsf
23	1635		Start logging rig up
23	1755		Start going down with the triple combination (TAP/DIT/HLDT/APS/HNGS/QSST) tool string
23	1845	0	Stop 5 min at mudline for temperature calibration
23	1900	220	Tool at TD; start logging-up pass at 900 ft/hr
23	1925	74	Tool back into pipe; speed up to 1500 ft/hr to log mudline
23	1935	0	End of pass 1
23	1952	204	Tool at TD; start logging-up pass 2 at 900 ft/hr
23	2022	73	Tool back in pipe; end of pass 2
23	2032	220	Tool at TD for QSST checkshot survey
23	2110	74	Tool back into pipe
23	2150		Tool back on rig floor
23	2315		Finish rig-down
23	2315		Start logging rig up
24	0020		Start going down with FMS-sonic (FMS/DSI/SGT) tool string
24	0100	220	Tool at TD; start logging-up pass at 900 ft/hr
24	0135	73	Tool back into pipe; end of pass 1
24	0145	220	Tool at TD; start logging-up pass 2 at 900 ft/hr
24	0210	73	High tension when top of tool enters pipe; end of pass 2
24	0245	73	Tool worked into pipe
24	0320		Tool back on rig floor
24	0415		Finish rig-down

Notes: TD = total depth. See Table T8, p. 102, in the "Explanatory Notes" chapter for definitions of acronyms.